COMPUTATIONAL TECHNIQUES TO ADDRESS THE SIGN PROBLEM IN NON-RELATIVISTIC QUANTUM THERMODYNAMICS

Andrew Christopher Loheac

A dissertation submitted to the faculty at the University of North Carolina at Chapel Hill in partial fulfillment of the requirements for the degree of Doctor of Philosophy in the Department of Physics and Astronomy in the College of Arts and Sciences.

Chapel Hill
2019

Approved by:

Joaquín E. Drut

Jonathan Engel

Fabian Heitsch

Reyco Henning

Amy Nicholson

© 2019
Andrew Christopher Loheac
ALL RIGHTS RESERVED

ABSTRACT

Andrew Christopher Loheac: Computational Techniques to Address the Sign Problem in Non-Relativistic Quantum Thermodynamics
(Under the direction of Joaquín E. Drut)

Understanding quantum many-body physics is crucial to physical systems throughout condensed matter, high-energy, and nuclear physics, as well as the development of new applications based upon such systems. Stochastic techniques are generally required to study strongly-interacting quantum matter, but are frequently hindered by the sign problem, a signal-to-noise issue which breaks down importance sampling methods for many physical models. This dissertation develops several novel stochastic nonperturbative and semi-analytic perturbative techniques to circumvent the sign problem in the context of non-relativistic quantum gases at finite temperature. These techniques include an extension to hybrid Monte Carlo based on an analytic continuation, complex Langevin, and an automated perturbative expansion of the partition function, all of which use auxiliary field methods. Each technique is used to compute first predictions for thermodynamic equations of state for non-relativistic Fermi gases in spin-balanced and spin-polarized systems for both attractive and repulsive interactions. These results are frequently compared against second- and third-order virial expansions in appropriate limits. The calculation of observables including the density, magnetization, pressure, compressibility, and Tan's contact are benchmarked in one spatial dimension, and extended to two and three dimensions, including a study of the unitary Fermi gas. The application of convolutional neural networks to improve the efficiency of Monte Carlo methods is also discussed.

TABLE OF CONTENTS

LIST OF FIGURES . . . . **vii**

LIST OF TABLES . . . . **xiii**

LIST OF ABBREVIATIONS . . . . **xiv**

LIST OF SYMBOLS . . . . **xv**

1 Introduction **1**

1.1 Dissertation overview 2

1.2 Why are non-relativistic systems interesting? 3

1.3 Brief survey of quantum many-body methods 4

1.4 Experimental counterparts 6

2 Foundations of Interacting Quantum Systems **7**

2.1 Equations of state for noninteracting quantum gases on the lattice 8

2.2 Auxiliary field representation of the partition function 10

2.2.1 Hubbard-Stratonovich transformation for contact interactions 12

2.3 Difficulty of direct linear algebra and mean field approaches 16

2.4 Finite-temperature determinantal Monte Carlo 19

2.4.1 Hybrid quantum Monte Carlo 21

2.4.2 Computing observables stochastically 24

3 Strongly Interacting Fermi Gases in One Dimension **27**

3.1 Equation of state results for the unpolarized system 28

3.1.1 Calculating the second-order virial coefficient on the lattice exactly 29

3.1.2 Tan's contact for the unpolarized system 32

3.1.3 Extending the unpolarized system to more flavors 33

4 Interacting Spin-Polarized Fermi Gases via Complex Chemical Potentials . . . 35
4.1 Observables, scales and computational technique . . . 36
4.2 Monte Carlo results and the analytic continuation . . . 38
4.3 Magnetization-to-density ratio and magnetic susceptibility . . . 43
4.4 Comparison with other approaches . . . 44
  4.4.1 Virial expansion . . . 44
  4.4.2 Lattice perturbation theory . . . 47

5 High-Order Lattice Perturbation Theory for Interacting Fermions . . . 51
5.1 Weak-coupling lattice perturbation theory formalism . . . 51
  5.1.1 Path integral form of the grand-canonical partition function . . . 51
  5.1.2 Expanding the fermion determinant . . . 53
  5.1.3 Recovering Wick's theorem by calculating the path integral exactly at each order . . . 55
  5.1.4 Transforming to frequency-momentum space on the lattice . . . 57
  5.1.5 Computing finite Matsubara frequency sums analytically: two tricks . . . 58
5.2 Perturbative results for the equation of state . . . 60
  5.2.1 Analytic expressions for the perturbative expansion . . . 61
  5.2.2 Pressure equation of state via perturbation theory . . . 63
  5.2.3 Pressure and density equations of state for the unpolarized one-dimensional system . . . 68
  5.2.4 Equations of state for the polarized one-dimensional system . . . 71
  5.2.5 Perturbative virial coefficients . . . 72
5.3 Second- and third-order Matsubara frequency sums . . . 74
5.4 Object-oriented design for analytic perturbative expansions . . . 76

6 Complex Langevin Dynamics . . . 82
6.1 Formulation of the complex Langevin approach for QMC . . . 83
  6.1.1 Complex Langevin pitfalls . . . 85
  6.1.2 Modified action . . . 86
6.2 Unpolarized equation of state using complex Langevin . . . 87
6.3 Spin-polarized fermions using complex Langevin . . . 89
  6.3.1 Third-order virial expansion . . . 92

6.3.2 Density equation of state 93

6.3.3 Polarization equation of state 97

6.3.4 Systematics of Langevin time discretization 100

6.4 Reducing the sign problem with convolutional neural networks 101

7 Systems in Higher Dimensions 107

7.1 Spin-polarized fermions in two spatial dimensions 107

7.2 The polarized Fermi gas at unitarity 110

APPENDIX NLO WEAK-COUPLING EXPANSION FOR POLARIZED SYSTEMS 117

REFERENCES 123

LIST OF FIGURES

2.1 Result for the pressure P normalized by the non-interacting counterpart P_0 that is obtained when attempting a mean-field analysis for the interacting Hamiltonian. The results are shown for a variety of dimensionless couplings λ, which is related to the bare coupling by $\lambda = \sqrt{\beta}g$. Comparing to the result obtained via HMC in Fig. 3.2, we can see the result is somewhat qualitatively correct within the virial region, but the result is completely wrong for large values of $\beta\mu$. *Inset:* A comparison of the mean-field result with the second-order virial expansion of the pressure (shown as a dashed black line). Mean field fails to correctly quantitatively capture the behavior of the virial region. 18

2.2 Rendering of an auxiliary field σ which is of spacetime extent $N_x \times N_\tau = 51 \times 60$ at a given point in its classical trajectory some time after thermalization has occurred. Note that the field is valid only at integer lattice points; the solid planes between such points are for visualization only. 24

3.1 Density n, in units of the density of the noninteracting system n_0, as a function of the dimensionless chemical potential $\beta\mu$ and coupling λ. From bottom to top, the coupling is $\lambda = 0.0, 1.0, 1.25, 1.5, \ldots, 2.5, 2.75, 3.0, 3.1, 3.2, \ldots, 4.0$. The dashed line joins the maxima at each λ. 29

3.2 Pressure P, in units of the pressure of the noninteracting system P_0, as a function of the dimensionless chemical potential $\beta\mu$ and coupling λ, as obtained by $\beta\mu$ integration of the density. The values of λ shown in this plot are the same as in Fig. 3.1. 30

3.3 Isothermal compressibility κ, in units of the compressibility of the noninteracting system κ_0, as a function of the dimensionless chemical potential $\beta\mu$ and coupling λ, as obtained by $\beta\mu$ differentiation of the density. The values of λ shown in this plot are the same as in Fig. 3.1, but from top to bottom instead. 30

3.4 Tan's contact C scaled by $\beta\lambda_T/(2Q_1\lambda^2) = \pi\beta^2/(2L\lambda^2)$ as a function of $\beta\mu$. The black line shows C in the absence of interactions. *Inset:* Zoom-in of the main plot on the region $-4.5 \leq \beta\mu \leq -1.0$, also showing the leading-order virial expansion. Both plots show data for $\lambda = 0.5, 1.0, 1.5, \ldots, 4.0$, which appear from bottom to top. 34

4.1 *Left:* Density as a function of the imaginary chemical potential difference βh_I at various values of $\beta\mu$. *Right:* Analytic continuation of the density as a function of βh. In both plots the density is an even function about the origin. Both plots are at a dimensionless coupling of $\lambda = 1.0$, and the physical quantities are plotted in units of the density of the noninteracting, unpolarized system. 38

4.2 *Left:* Magnetization as a function of the imaginary chemical potential difference βh_I at various values of $\beta\mu$. *Right:* Analytic continuation of the magnetization as a function of βh. In both plots the magnetization is an odd function about the origin, are at a dimensionless coupling of $\lambda = 1.0$, and the physical quantities are plotted in units of the density of the noninteracting, unpolarized system. 39

4.3 *Left:* Tan's contact as a function of the imaginary chemical potential difference βh_{I} at various values of $\beta\mu$ for a dimensionless coupling of $\lambda = 1.0$. C_0 is the contact at $\beta h = \beta\mu = 0$. *Right:* Analytic continuation of the contact as a function of βh at various values of $\beta\mu$. In both plots the contact is an even function about the origin. The curves on the right are color-wise paired by their value of $\beta\mu$, which coincides with the value on the left (by color code, or from top to bottom). Dashed-dotted lines give the results from a fit of the data to the polynomial-type ansatz (4.10), whereas solid lines result from fits of the data to our Padé-type ansatz (4.8) for the fit functions. 39

4.4 Ratio of the magnetization m to the density n as a function of the real-valued βh and $\beta\mu = -2.0, -1.0, 0, 1.0, 2.0$. The solid lines show the second-order virial expansion at $\beta\mu = -2$ (top) and -1 (bottom). Note that the virial expansion works well for $\beta\mu = -2$, but fails dramatically for $\beta\mu = -1$ and above; see Sec. 4.4.1 for details. 45

4.5 The magnetic susceptibility χ as a function of βh at representative values of $\beta\mu$, obtained by taking an analytic derivative of the magnetization with respect to βh. *Left:* Interacting case at $\lambda = 1$. *Right:* Noninteracting case in the continuum. 45

4.6 Density and magnetization at a dimensionless coupling of $\lambda = 1.0$ in units of the unpolarized, noninteracting density n_0. The solid black lines how the second-order virial expansion for each value of βh. Error bars were estimated by varying the fit parameters by an amount given by the uncertainty in the calculated fits. 48

4.7 *Left:* Tan's contact as a function of the imaginary chemical potential difference βh_{I} at various values of $\beta\mu$ for a dimensionless coupling of $\lambda = 1.0$. C_0 is the contact at $\beta h = \beta\mu = 0$. *Right:* Analytic continuation of the contact as a function of βh at various values of $\beta\mu$. In both plots the contact is an even function about the origin. The curves on the right are color-wise paired by their value of $\beta\mu$, which coincides with the value on the left (by color code, or from top to bottom). Dashed-dotted lines give the results from a fit of the data to the polynomial-type ansatz (4.10), whereas solid lines result from fits of the data to our Padé-type ansatz (4.8) for the fit functions. 49

4.8 Comparison of the Monte Carlo results after the analytic continuation, a next-to-leading-order perturbation theory calculation, and the free gas for the density and the magnetization. Results are displayed in $\beta h = 0.0, 0.5, 1.0, 1.5$ and 2.0 in the strongly interacting region $\beta\mu > -1$. 50

5.1 Feynman diagram for the next-to-leading order (NLO) contribution to the grand canonical partition function. 61

5.2 Feynman diagrams for the next-to-next-to-leading order (N2LO) contribution to the grand canonical partition function. 62

5.3 Feynman diagrams for the next-to-next-to-next-to leading order (N3LO) contribution to the grand canonical partition function. 62

5.4 Feynman diagrams for the next-to-next-to-next-to-next-to leading order (N4LO) contribution to the grand canonical partition function. 63

5.5 The perturbative expansion for the grand-canonical partition function as $\ln \mathcal{Z} = P/P_0$ written explicitly up to N3LO, where we consider the weak coupling limit $A^2 \sim \tau g$. In this respect, one may qualitatively regard the expansion as expanding in g directly on the lattice. 67

5.6 Pressure P of the attractive (top) and repulsive (bottom) unpolarized Fermi gas in units of the pressure of the noninteracting system P_0, as shown for the dimensionless interaction strengths $\lambda = 0.5$, 1.0, 1.5, 2.0, and $\lambda = -0.5$, -1.0, -1.5, -2.0 for the attractive and repulsive cases, respectively. The NLO (dashed line), N2LO (dash-dotted line), and N3LO (solid line) results from perturbation theory are displayed for each coupling. The corresponding data points for each attractive coupling are computed using HMC (see Ref. [1]). 69

5.7 Density n of the attractive (top) and repulsive (bottom) unpolarized Fermi gas in units of the density of the noninteracting system n_0, as shown for the dimensionless interaction strengths $\lambda = 0.5$, 1.0, 1.5, 2.0 (attractive), and $\lambda = -0.5$, -1.0, -1.5, -2.0 (repulsive). The NLO (dashed line), N2LO (dash-dotted line), and N3LO (solid line) results of perturbation theory are displayed for each coupling and are compared with HMC results (see Ref. [1]) in the attractive case. For both plots, the black diamonds show CL results (RL for the attractive case), regulated with $\xi = 0.1$ as described in the main text. The statistical uncertainty of the CL results is estimated to be on the order of the size of the symbols, or less, as supported by the smoothness of those results. 70

5.8 Density n of the attractive (top) and repulsive (bottom) unpolarized Fermi gas in units of the density of the noninteracting system n_0, as shown for the dimensionless interaction strengths $\lambda = 2.5$, 3.0, 3.5, 4.0 (attractive), and $\lambda = -2.5$, -3.0, -3.5, -4.0 (repulsive). The NLO (dashed line), N2LO (dash-dotted line), and N3LO (solid line) results of perturbation theory are displayed for each coupling and are compared with HMC results (see Ref. [1]) in the attractive case. It is evident that perturbation theory fails miserably at these higher couplings, and competing oscillations set in for the repulsive case. For both plots, the black diamonds show CL results (RL for the attractive case), regulated with $\xi = 0.1$ as described in the main text. The statistical uncertainty of the CL results is estimated to be on the order of the size of the symbols, or less, as supported by the smoothness of those results. 71

5.9 Fifth-order perturbative virial expansion for the pressure P/P_0 for two attractive and repulsive couplings. The expansions are shown for which the virial coefficients are computed at NLO (dashed line), N2LO, (dotted line), and N3LO (dash-dotted line). The fully solid line shows the full perturbative calculation of the pressure at N3LO, as shown in Fig. 5.6. Results from HMC data (see Ref. [1]) are displayed as corresponding data points for the attractive couplings. 73

5.10 Plot of the second, third, fourth, fifth, and sixth-order virial coefficients as computed via Fourier projection under third-order lattice perturbation theory, shown as a function of the dimensionless coupling λ. The plot displays the virial coefficients from the non-interacting limit of $\lambda = 0$ to the strongly-coupled regime. 75

5.11 Reduced class diagram for the C++ implementation of computing the analytic expressions for perturbative contributions to the grand-canonical partition function. All objects used in the calculation are derived from the `SymbolicTerm` class, and can be broken into two categories. The left hand side of the diagram contains expression objects which are containers for pointers to one or more `SymbolicTerm` instances (which itself may resolve to an expression object), and the right hand side of the diagram shows terminal objects which are representations of mathematical objects that appear in the perturbation theory formalism. For brevity, this diagram only displays particular methods and fields discussed further in the text below. In addition, each class typically provides relevant operator overloads to define particular behaviors, as well as overriding implementations of `SymbolicTerm::copy()` and `SymbolicTerm::to_string()`. 78

6.1 The normalized density n/n_0, where n_0 is the noninteracting result, for $\lambda = -1.0$ and $\beta\mu = 1.6$, as a function of the Langevin time t for several values for the regulating parameter ξ [see Eq. (6.13)]. The result was computed on a spatial lattice of $N_x = 80$ and a temporal lattice of $N_\tau = 160$. For a choice of $\xi = 0$, where the regulating term is removed, CL tends toward an incorrect value for the density. When $\xi \simeq 0.1$, the additional term provides a restoring force and the stochastic process converges to a different value consistent with perturbation theory. On the other hand, for cases where $\xi < 0$, the solution diverges, as expected. Each plotted line corresponds to a fixed count of 10^5 iterations of performing one integration step of the adaptive step δt; as such, the length of the line gives an indication as to the computational demand to reach time t for a given ξ. 87

6.2 Plot of the complex quantity e^{-S} in terms of its magnitude ρ and phase θ such that $e^{-S} = \rho e^{i\theta}$, for a CL calculation at $\lambda = -1.0$ and $\beta\mu = 1.6$. Data points are plotted as $\ln(\rho)\cos(\theta)$ and $\ln(\rho)\sin(\theta)$ as parametric functions of the Langevin time t. Plots are displayed for four values of the parameter ξ. Note that for $\xi = 0$, the solution does not converge, but does converge for $\xi = 0.005$ and 0.1. For the case where $\xi = -0.1$, the result for the density n/n_0 rapidly diverges, as expected [note change in scale for y axis and see Fig. 6.1]. Data points show the locations where samples were taken along the CL trajectory; the shaded areas result from straight lines joining the data points. 88

6.3 Histograms of values taken of $2\ln(|\det M|)$ over the course of a CL simulation at $\xi = 0.1$ for a few representative values of the coupling λ (shown primarily on the repulsive side and for the strongest coupling) and the chemical potential $\beta\mu$ (shown in the virial and strongly interacting regions). The distributions across parameter values appear approximately log-normal and well behaved, and indicate that the drift force is generally free of singularities. Although the magnitude of the action can vary across parameter space, the variance across field configurations is centered about a well-defined mean. 90

6.4 Density equation of state $n = n_\uparrow + n_\downarrow$ normalized by the non-interacting, unpolarized counterpart n_0, for attractive (top) and repulsive (bottom) interactions of strength $\lambda = \pm 1$. *Insets:* Zoom in on region $\beta\mu > 0$ (top) and $\beta\mu > 1$ (bottom). In all cases, the CL results are shown with colored symbols, iHMC results (from Ref. [2]) appear with black diamonds, perturbative results at third order are shown with solid lines, and virial expansion results appear as dashed lines. 94

6.5 Density equation of state $n = n_\uparrow + n_\downarrow$ normalized by the non-interacting, unpolarized counterpart n_0 for attractive (top) and repulsive (bottom) interactions of strength $\lambda = \pm 2$. *Insets:* Zoom in on region $\beta\mu > 0$ (top) and $\beta\mu > 1$ (bottom). The CL results are shown with colored symbols, perturbative results at third order are shown with solid lines, and virial expansion results appear as dashed lines. 95

6.6 Density equation of state $n = n_\uparrow + n_\downarrow$ normalized by the non-interacting, unpolarized counterpart n_0 for attractive (top) and repulsive (bottom) interactions of strength $\lambda = \pm 4$. The CL results are shown with colored symbols, perturbative results are shown with solid red lines, and HMC for the attractive, unpolarized case is shown in black diamonds [1]. 96

6.7 Spin polarization $m = n_\uparrow - n_\downarrow$ normalized by the non-interacting, unpolarized counterpart n_0 for attractive (top) and repulsive (bottom) interactions of strength $\lambda = \pm 1$. The CL results are shown with colored symbols, iHMC results (from Ref. [2]) appear with black diamonds, perturbative results at third order are shown with solid lines, and virial expansion results appear as dashed lines. 97

6.8 Spin polarization $m = n_\uparrow - n_\downarrow$ normalized by the non-interacting, unpolarized counterpart n_0 for attractive (top) and repulsive (bottom) interactions of strength $\lambda = \pm 2$. The CL results are shown with colored symbols, perturbative results at third order are shown with solid lines, and virial expansion results appear as dashed lines. 98

6.9 Spin polarization $m = n_\uparrow - n_\downarrow$ normalized by the non-interacting, unpolarized counterpart n_0 for attractive (top) and repulsive (bottom) interactions of strength $\lambda = \pm 4$. The CL results are shown with colored symbols, perturbative results at third order are shown with solid lines, and virial expansion results appear as dashed lines. 99

6.10 *Left:* Relative difference between the density $n_\uparrow + n_\downarrow$ computed via CL (n_{CL}) and the third-order perturbative result n_{PT} for three positive values of $\beta\mu$, as a function of the CL timestep t_{CL}. The dashed horizontal line shows where $n_{\mathrm{CL}} = n_{\mathrm{PT}}$. *Right:* Relative difference between n_{CL} and the third-order virial expansion n_{virial} for three values of $\beta\mu$ of small fugacity, as a function of t_{CL}. The dashed horizontal line shows where $n_{\mathrm{CL}} = n_{\mathrm{virial}}$. In both plots, the coupling was set to $\lambda = \pm 1$, where solid and open symbols refer to repulsive and attractive couplings, respectively. Error bars represent the statistical error of the CL calculation, and indicate agreement with PT and the virial expansion as $t_{\mathrm{CL}} \to 0$. 100

6.11 Architecture of the convolutional neural network. The complex, normalized form of the fermion matrix is inserted as the input of the convolutional network. Additional information is passed in at an intermediate step through the sequential network, and two output neurons categorize the accuracy of the considered auxiliary field configuration (see main text). 102

6.12 Predictions and performance of the trained convolutional neural network shown in Fig. 6.11. The plots on the left hand side corresponds to the case of attractive interactions where $\lambda = 1$, and the right corresponds to repulsive interactions where $\lambda = -1$. *Top:* Density n normalized by the non-interacting counterpart n_0. Values of the density made by the CNN prediction (black squares), CL simulations (green circles), and N3LO reference values (purple triangles) are shown. The red shaded curve indicates the standard deviation of all samples provided by CL, and the blue shaded curve shows the standard deviation of the subset of samples selected by the CNN whose error is estimated to be $\leq 10\%$. *Center:* Percentage of the samples across the training and validation data sets which were correctly classified by the CNN for each value of $\beta\mu$. *Bottom:* Fraction of the density samples whose error is $\leq 10\%$ for each value of $\beta\mu$. In all plots, the grey shaded region indicates the values of $\beta\mu$ whose samples were used to train the CNN. 105

7.1 Density equation of state n normalized by the non-interacting counterpart n_0 for the spin-balanced attractively interacting Fermi gas in two spatial dimensions as a function of the dimensionless chemical potential $\beta\mu$. Curves are displayed for five interaction strengths from $\beta\epsilon_B = 0.1$ to 3.0. Colored symbols correspond to CL calculations at $N_x = 16$, and black diamonds correspond to HMC calculations [3] at $N_x = 19$, where both are at $\beta = 10$. PT at N3LO (pink dotted lines) are shown at each value of the chemical potential asymmetry, which correspond to that of the CL data points from bottom to top. 109

7.2 Density equation of state n normalized by the non-interacting counterpart n_0 for the spin-polarized attractively interacting Fermi gas in two spatial dimensions as a function of the dimensionless chemical potential $\beta\mu$. Curves are displayed for five polarizations from $\beta h = 0.0$ to 2.0. Colored symbols correspond to CL calculations at $\beta\epsilon_B = 0.1$ (top) and $\beta\epsilon_B = 0.5$ (bottom) for $N_x = 16$ and $\beta = 10$. PT at N2LO (red solid lines) is shown for the polarized case, and at N3LO (pink dotted line) for the spin-balanced case. Note that the values of βh for each of the PT curves correspond to that of the CL data points from bottom to top. 111

7.3 *Top:* Density of the unpolarized UFG obtained with CL (blue squares), in units of the noninteracting, unpolarized density n_0 as a function of the dimensionless mean chemical potential $\beta\mu$. Also shown is the third-order virial expansion (dashed line), experimental results of Refs. [4, 5] (red circles), bold diagrammatic Monte Carlo (BDMC) calculations [5] (dark diamonds), and determinantal hybrid Monte Carlo (DHMC) calculations [6] (light diamonds). *Bottom:* Compressibility κ as derived from the density EOS, in units of its noninteracting counterpart κ_0 as a function of the dimensionless pressure P/P_0 (blue squares). A comparison is made to experimental values [4] (red circles) and the third-order virial expansion (dashed line). Statistical uncertainties for the CL results are on the order of the symbol sizes. The shaded areas indicate the superfluid phase. 114

7.4 Density $n = n_1 + n_2$ of the spin-polarized Fermi gas at unitarity in three spatial dimensions, normalized by the density of the non-interacting, unpolarized system n_0. Results using CL are shown in colored points for chemical potential asymmetries $\beta h = 0.0$, 0.4, 0.8, 1.2, 1.6, and 2.0 at a spatial lattice volume of $N_x^3 = 7^3$. The second-order virial expansion is shown in solid black lines. Additionally, experimental results for the unpolarized system at unitarity are shown in solid red circles (see Ref. [4]). 115

7.5 *Left:* Density of the UFG in units of the noninteracting density, from top to bottom: $\beta h = 0$ (circles), 0.4 (octagons), 0.8 (hexagons), 1.2 (pentagons), 1.6 (squares), 2.0 (triangles), compared to the third-order virial expansion (dashed lines). Note the colors encode fixed values of $\beta\mu$ shown in all panels. *Center:* Magnetization in units of the interacting density for the balanced system as a function of βh for several values of $\beta\mu$. For $\beta\mu \leq -1.0$, the third-order virial expansion is shown with dashed lines. *Right:* Dimensionless magnetic susceptibility $\bar{\chi}_M$ as a function of βh (symbols) compared to the corresponding susceptibility of the free Fermi gas $\bar{\chi}_M^0$ (dotted lines) at equal chemical potential and asymmetry (color and shake coding match other panels). *Inset:* Ratio $\bar{\chi}_M/\bar{\chi}_M^0$ as a function of $\beta\mu$ at $\beta h = 0.4$. 116

LIST OF TABLES

4.1 Fit parameters for the density as they appear in Eq. (4.8) at a constant dimensionless coupling of $\lambda = 1.0$ for various values of $\beta\mu$, as well as the χ^2 per degree of freedom for each fit. Note that γ is not a fit parameter (see main text). 42

4.2 Fit parameters for the magnetization as they appear in Eq. (4.5) at a constant dimensionless coupling of $\lambda = 1.0$ for various values of $\beta\mu$, as well as the χ^2 per degree of freedom for each fit. 43

4.3 Fit parameters for the contact as they appear in Eq. (4.8) at a constant dimensionless coupling of $\lambda = 1.0$ for various values of $\beta\mu$, as well as the χ^2 per degree of freedom for each fit. Note that γ is not a fit parameter (see main text). 44

5.1 Detail of next-to-leading order (NLO), next-to-next-to-leading order (N2LO), and next-to-next-to-next-to-leading order (N3LO) contributions (respectively, order A^2, A^4, and A^6) to the grand-canonical partition function $\mathcal{Z}$. The indicated diagram figure refers to the corresponding fully-connected Feynman diagram or product of such diagrams for each contribution. The volume $V = N_x N_\tau$ that appears in all expressions refers to the spacetime volume of the lattice. The greatest number of loops that appear for each fully-connected diagram is also provided. It is implicit in the notation that a momentum-conserving Kronecker delta has been utilized to eliminate momentum sums: one in the case of S_4 and $S_4^{(1)}$, but two in the case of S_6. 64

5.2 Part I detail of next-to-next-to-next-to-next-to (N4LO) contribution (order A^8) to the grand-canonical partition function $\mathcal{Z}$. The remainder of the N4LO contributions are provided in Table 5.3. All diagrams that appear in this table are disconnected diagrams, and will cancel after the logarithm of the partition function is taken. The indicated diagram figure refers to the corresponding fully-connected Feynman diagram or product of such diagrams for each contribution. The volume $V = N_x N_\tau$ that appears in all expressions refers to the spacetime volume of the lattice. The greatest number of loops that appear for each fully-connected diagram is also provided. It is implicit in the notation that a momentum-conserving Kronecker delta has been utilized to eliminate momentum sums. 65

5.3 Part II detail of the next-to-next-to-next-to-next-to (N4LO) contribution (order A^8) to the grand-canonical partition function $\mathcal{Z}$. The first part of the N4LO contributions are provided in Table 5.2. All diagrams that appear in this table are new fully-connected diagrams that appear at this order. The indicated diagram figure refers to the corresponding fully-connected Feynman diagram or product of such diagrams for each contribution. The volume $V = N_x N_\tau$ that appears in all expressions refers to the spacetime volume of the lattice. The greatest number of loops that appear for each fully-connected diagram is also provided. It is implicit in the notation that a momentum-conserving Kronecker delta has been utilized to eliminate momentum sums. 66

5.4 Results for the second, third, fourth, and fifth-order virial coefficients of the pressure P [see Eq. (5.50)] at NLO, N2LO, and N3LO for two repulsive and attractive couplings. All coefficients are computed for a spatial lattice size of $N_x = 100$, $\beta = 8.0$, and a temporal lattice spacing of $\tau = 0.05$. The fifth-order virial expansion is displayed in Fig. 5.9. 74

LIST OF ABBREVIATIONS

1D	one spatial dimension
2D	two spatial dimensions
3D	three spatial dimensions
CL	complex Langevin
EOS	equation of state
FFT	fast Fourier transform
HMC	hybrid Monte Carlo
HS	Hubbard-Stratonovich
NLO	next-to-leading order
N2LO	next-to-next-to-leading order
N3LO	next-to-next-to-next-to-leading order
PT	perturbation theory
QMC	quantum Monte Carlo
RL	real Langevin

LIST OF SYMBOLS

β	inverse temperature
μ	chemical potential
h	chemical potential asymmetry
g	bare coupling
b_n	n-th order virial coefficient
z	fugacity
λ	dimensionless coupling
λ_T	thermal de Broglie wavelength
$\hat{N}$	particle number operator
$\hat{H}$	Hamiltonian operator
$\hat{T}$	kinetic energy operator
$\hat{V}$	potential energy operator
M	fermion matrix
N_x	spatial lattice volume
N_τ	temporal lattice volume
C	Tan's contact
P	pressure
n	density
S	action
σ	Hubbard-Stratonovich auxiliary field
π	auxiliary momentum field
Q	canonical partition function
$\mathcal{Z}$	grand-canonical partition function
ξ	Langevin modified action parameter

CHAPTER 1: Introduction

The many-body system, both in the context of classical and quantum physics, has been a long-standing problem in a variety of fields. The classic n-body problem is a gravitational system of orbiting massive bodies according to a pairwise $1/r$ central potential, which requires the use of numerical tools to exactly solve the equations of motion beyond the two-body problem [7]. An understanding of the many-body problem in the context of quantum mechanics is crucial to a vast number of physically relevant systems, particularly throughout nuclear and condensed matter physics. Gluons form colorless bound states to produce hadrons, protons and neutrons interact to form nuclei, and electrons live on lattices of ions to provide unique materials, such as graphene. Tackling these challenges proves to be especially fruitful: the study of the quantum-many body problem illuminates the properties of how the universe's building blocks interact to create the dynamical phenomena around us.

Given this challenge of finding solutions to the quantum many-body problem, the development of numerical methods is a crucial pillar to supporting this track of research. Quantum Monte Carlo (QMC) techniques are used across nuclear [8], condensed matter [9], and high-energy physics [10] to nonperturbatively probe the collective behavior of interacting many-body systems in the quantum limit. Extracting quantitative information about the thermodynamics of these systems is notoriously difficult, or even practically impossible, in particular regimes of interest. For example, systems with a finite chemical potential in the context of quantum chromodynamics (QCD), imbalanced systems of ultracold fermions, and particular kinds of physical interactions pose a significant challenge to QMC methods. The most general roadblock preventing the study of these rich systems is the appearance of the sign and signal-to-noise problems which cause stochastic methods to break down and provide incorrect, inaccurate, or diverging results. At its core, the *sign problem* (arguably directly related to the signal-to-noise problem) results from a non-positive probability measure used in the importance sampling of the highly-dimensional integrand that is to be evaluated stochastically. Over the past several decades, significant work has been put into developing theoretical and algorithmic techniques to eliminate, or at least mitigate, the sign problem in a variety of contexts across many areas of physics; however, it has been strongly suggested that the sign problem is NP-hard, and therefore a general solution does not exist [11], and to search for one would prove fruitless. Therefore, more efficient and robust techniques to study many-body systems with limited computational resources are of general interest. The development of new techniques to overcome the sign problem in the context of non-relativistic quantum many-body systems will be the topic of this dissertation.

Section 1.1: Dissertation overview

In the present dissertation, we will focus on the development and testing of novel nonperturbative (stochastic) and semi-analytic perturbative techniques to calculate thermodynamic observables for non-relativistic systems normally plagued by a sign problem. In particular, we choose to study a system of fermions under both attractive and repulsive contact interactions at finite temperature; the variant of the system in one spatial dimension is generally known as the Gaudin-Yang model [12, 13]. The one-dimensional system is studied extensively here in light of benchmarking new techniques, but studies are extended to higher dimensions in the final chapter. The methods we have implemented include extensions to the more conventional hybrid Monte Carlo technique (which is a stochastic method based on the Metropolis-Hastings algorithm), the complex Langevin method (which permits the study of systems where the fermion matrix is complex, but drops the Metropolis algorithm for stochastic noise), and a novel perturbative method performed on the lattice. All of these techniques were used to study thermodynamic quantities of strongly-interacting fermions, including computing the density and pressure equations of state, virial coefficients, the isothermal compressibility, and Tan's contact. These observables are frequently compared to the virial expansion, which becomes valid in the semiclassical regime. To the best of our knowledge, the results that we have published, including those for repulsively-interacting and spin-polarized systems, are not previously known, even though these can be considered classic many-body condensed matter systems.

The work conducted over the course of the doctoral program for this dissertation has resulted in the following peer-reviewed publications, which form the basis of most of the upcoming chapters.[1] A footnote on the first page of each such chapter indicates the publications it is based upon. Quite often, the text in the dissertation provides additional discussion or details that were not available in the original manuscript.

1. M. D. Hoffman, P. D. Javernick, A. C. Loheac, W. J. Porter, E. R. Anderson, and J. E. Drut, *Universality in one-dimensional fermions at finite temperature: Density, pressure, compressibility, and contact*, Physical Review A **92**, 013631 (2015)

---

[1] As an author of the listed manuscripts, permission is granted by the American Physical Society to include these articles in whole or in part within this dissertation. Note that where appropriate, © American Physical Society in the year of publication.

2. Andrew C. Loheac, Jens Braun, Joaquín E. Drut, and Dietrich Roscher, *Thermal equation of state of polarized fermions in one dimension via complex chemical potentials*, Physical Review A **92**, 063609 (2015)
3. M. D. Hoffman, A. C. Loheac, W. J. Porter, and J. E. Drut, *Thermodynamics of one-dimensional SU(4) and SU(6) fermions with attractive interactions*, Physical Review A **95**, 033602 (2017)
4. Andrew C. Loheac and Joaquín E. Drut, *Third-order perturbative lattice and complex Langevin analyses of the finite-temperature equation of state of non-relativistic fermions in one dimension*, Physical Review D **95**, 094502 (2017)
5. Andrew C. Loheac, Jens Braun and Joaquín E. Drut, *Polarized fermions in one dimension: density and polarization from complex Langevin calculations, perturbation theory, and the virial expansion*, Physical Review D **98**, 054507 (2018)
6. Lukas Rammelmüller, Andrew C. Loheac, Joaquín E. Drut, and Jens Braun, *Finite-Temperature Equation of State of Polarized Fermions at Unitarity*, Physical Review Letters **121**, 173001 (2018)

The following article was published during the program, but falls outside the scope of this dissertation:

1. L. Rammelmüller, W. J. Porter, A. C. Loheac, and J. E. Drut, *Few-fermion systems in one dimension: Ground- and excited-state energies and contacts*, Physical Review A **92**, 013631 (2015)

Section 1.2: Why are non-relativistic systems interesting?

Modern QMC techniques are famous for their widespread use in lattice quantum chromodynamics (QCD), where the relativistic field theory of quarks and gluons are placed on a lattice such that they can be studied on a computer. The application of QMC to the non-relativistic counterpart in condensed matter physics is equally important, as non-relativistic systems of fermions and bosons are prevalent in many physical phenomena. A few of the foremost examples include ultracold atomic clouds, which may be controlled via Feshbach resonances and can exhibit interesting phase transitions and superfluid states.

As previously mentioned, the physical systems we will be examining in this dissertation will be of non-relativistic particles with a quadratic dispersion relation. However, most of the fundamental algorithms and techniques we apply were born in the context of relativistic lattice field theory (e.g., hybrid Monte Carlo), and still bear important connections with the methods we develop further in our research. Although the stochastic evaluation of path integrals is common to both relativistic and nonrelativistic theories, an important distinction between the two formalisms is the construction of differing fermion actions and the computational demand required to work with them. In this context, the study of nonrelativistic systems offers a more tractable challenge to benchmark new numerical algorithms as they are further developed, which can later be transferred to more difficult situations. In the relativistic case, one must be most concerned with maintaining local gauge invariance and consequences of breaking continuous rotational symmetry when discretizing the theory onto a lattice, which leads to introduction of plaquettes and the resulting Wilson gauge action [14]. This naturally leads to the construction of a gauge action, which by itself is a rich yet interesting theory to study. For further reading on QMC techniques for relativistic theories, we point the reader to texts [15, 16] on the subject.

Section 1.3: Brief survey of quantum many-body methods

In addition to the methods to address the sign problem presented in the following chapters, there are of course a whole host of techniques that others have used across the disciplines mentioned above. However, most of these methods are only applicable to particular models or dimensionality, are restricted to a particular regime of parameter space, or are not *ab initio* techniques, or methods with start from a well-defined Hamiltonian and systematically proceed without limiting assumptions. Additionally, many more tractable analytical solutions exist for systems at zero temperature (studies of the ground state) compared to systems at finite temperature. Systems in one spatial dimension are generally more soluble by analytic means compared to higher dimensions, if such a technique can be found. We will, however, provide a very brief survey of some of these additional methods for a handful of situations in the present chapter; it should be noted that overview is far from exhaustive.

The classic problem studied in quantum chemistry and condensed matter are properties of quantum systems close to “zero-temperature”, or cases where the ground-state of the system dominate the dynamics of the system. Although this type of analysis can provide many key properties, such as electronic structure and spectroscopy information, and may be sufficient in a wide array of situations, finite temperature can have a drastic effect on the behavior of particular systems.

The Bethe ansatz, first proposed by Hans Bethe in 1931 ([17], see also [18–20] for an introduction to the method) is capable of providing an analytic solution to the one-dimensional system at zero temperature. The method was applied to a system of spin-1/2 fermions in the Heisenberg model, and predicted critical properties of ferromagnetism. An extension of this method to systems at finite temperature, known as the thermodynamic Bethe Ansatz (TBA) [21] was introduced, but the method results in an infinite tower of coupled partial differential equations that must at some point be truncated, is difficult to work with, and is restricted to one spatial dimension. Nevertheless, it has been applied to a number of models of interest, including a number that are on the lattice [22–24]. Since the Bethe ansatz and its thermodynamic counterpart can, in principle, study a whole host of one-dimensional models, many might consider the 1D interacting system to be solved; however, many such studies remain unexplored which must overcome limitations of this analytic method, particularly for systems at finite temperature. Some of these previously unknown results in one spatial dimension are presented in this dissertation.

Beyond analytic techniques, numerical methods have also been developed to extract properties of systems at zero temperature, such as the ground-state energy of a strongly interacting system. Perhaps the most widely known is the Hartree-Fock method [25], which is applicable to a wide range of many-electron atomic and molecular systems, and is a popular starting point in many quantum chemistry and solid state [26] problems. A number of Monte Carlo methods exist to study systems in the ground state, including diffusion Monte Carlo (DMC), Green's function Monte Carlo (GFMC) [27] and variational Monte Carlo (VMC) [28], and auxiliary field Monte Carlo (AFMC). These techniques have been used to compute various interesting physical quantities, such as ground-state and low-lying excited state energies of nuclei [29–34], estimates on isospin-mixing matrix elements [34], and the first calculation of the matrix elements for neutrinoless double beta decay for light nuclei [35]; many of these calculations have extraordinary agreement with experiments [8].

These Monte Carlo and other *ab initio* methods are capable of studying properties of light nuclei, but begin to break down as the number of nucleons becomes too large. Density functional theory (DFT) [36–38], although not *ab initio*, has proved successful in attacking even the largest nuclei, and has recently been applied to Fermi gases [39]. Mean-field theory is frequently leaned upon when *ab initio* calculations become unwieldy, but often have difficulty capturing important statistical features of interacting systems. A host of other techniques have been developed to address the infamous sign problem, but each generally have their own advantages and limitations. For instance, Lefschetz thimbles [40–44] involves an evolution of manifolds into the complex plane, over which a new representation of the path integral can be evaluated. The method of fermion bags [45–48] seeks to rewrite the partition function as a sum over determinants over a smaller subspace, which can allow the algorithm to study vastly larger lattice sizes. Bosonization seeks to recast a fermionic theory into one written in terms of bosons. As can be seen, there exists a small zoo of techniques to address studies of interacting many-body quantum system. No single method has risen as superior to all others, as each appears to have their own niche of strengths. New techniques and improvements on old ones constantly appear on the market, with perhaps the most modern additions involving applications of machine learning.

Section 1.4: Experimental counterparts

The condensed matter systems we have chosen to study in this dissertation are by in large accessible systems that may be studied experimentally using ultracold atomic gases in laboratories today with an extraordinary degree of precision. Although theoretical developments in some respects remain a few steps ahead of current experimental techniques, there are some works with which we are able to compare to directly, including measurements of the equation of state for unpolarized fermions at unitarity [4] and in two spatial dimensions [49]. However, the experimental study of ultracold atomic gases and their superfluid states spans back to experiments of helium-4 [50, 51] and up to the first production of a Bose-Einstein condensate with rubidium-87 [52]. More recently, ultracold fermionic condensates have been realized in the laboratory [53–57]. Although outside the context of this dissertation, experimental capabilities have gone as far as determining the entanglement entropy in quantum gases [58], which was theoretically explored [59–62] by our research group using similar stochastic techniques for interacting many-body systems.

CHAPTER 2: Foundations of Interacting Quantum Systems

The overarching goal of the work in this dissertation is to study the thermodynamic properties of interacting many-body quantum systems using several different computational approaches. In particular, we often choose to compute equations of state, which although were not previously known for a number of physical systems studied here, help to quickly benchmark and understand the behavior of new methods. These properties at finite temperature are computed from a partition function in the grand-canonical ensemble of the system, which always serves as a starting point for our analysis. The bulk of the analytic work is in rewriting the partition function in a tractable form from which physics can be extracted with reasonable resources. In this chapter, we will overview such a recasting of the partition function in terms of auxiliary fields, and look at well-established Monte Carlo techniques for computing observables stochastically. We will also discuss the so-called *sign problem*, which causes Monte Carlo methods to break down for many systems of interest, and therefore motivates the development of the techniques in this work.

The analytic starting point for computing thermodynamic properties by all the techniques presented in this work is the *grand-canonical partition function* for each particular system of interest. This partition function establishes an ensemble of states for a system that is in thermodynamic equilibrium with heat and particle reservoirs. The typical state variables of this ensemble are the temperature T (which will typically appear in our formulations as the inverse temperature $\beta = 1/k_B T$, where we take the Boltzmann constant $k_B = 1$), the spatial volume V, and the chemical potential μ. For a quantum mechanical system governed by a Hamiltonian $\hat{H}$, the grand-canonical partition function is given by a trace over the Boltzmann weights,

$$\mathcal{Z}(\mu, V, T) = \mathrm{Tr}\left[e^{-\beta(\hat{H} - \sum_i \mu_i \hat{N}_i)}\right] \tag{2.1}$$

where the sum in the exponent is over any number of particle species with corresponding chemical potentials. Throughout the following chapters, we will consider spin-1/2 fermions in situations where the chemical potentials for spin-up and spin-down flavors are equal (the spin-balanced case), and where $\mu_\uparrow \neq \mu_\downarrow$ (the polarized case). We will also look at both cases across dimensions, focusing first on developing techniques in one dimension, and then expanding to two and three dimensions.

Section 2.1: Equations of state for noninteracting quantum gases on the lattice

Before moving to computing equations of state for interacting many-body systems, we should first overview a derivation for the pressure and density equations of state for the noninteracting equivalents. These expressions will frequently enter into our analyses later on, as we typically present thermodynamic quantities for interacting systems in units of the noninteracting counterparts.

For the moment, let us consider the simple system of non-relativistic, unpolarized fermions[1] on the lattice; shortly we will extend the result to polarized fermions. The Hamiltonian for a free system is simply given as the kinetic energy,

$$\hat{H} = \frac{\hat{\mathbf{p}}^2}{2m}, \quad \hat{H}|k\rangle = \epsilon_k|k\rangle, \tag{2.2}$$

where the momentum operator $\hat{\mathbf{p}}$ may be extended to any number of dimensions, and the eigenvalues of the Hamiltonian are labeled as ϵ_k. Evaluating the partition function in the grand-canonical ensemble for ideal fermions is straightforward in the occupation number basis $n_k = \{n_0, n_1, n_2, \ldots n_\infty\}$ for each corresponding single-particle energy level ϵ_k. If we now consider spin-1/2 fermions which come in two flavors of types $s =\uparrow, \downarrow$ (such that $\mu = \mu_\uparrow = \mu_\downarrow$ and $N = N_\uparrow + N_\downarrow$), then for spin s,

$$\mathcal{Z}_s = \sum_{N=0}^{\infty} \sum_{\{n_k\}} \exp\left[-\beta\left(\sum_k n_k\epsilon_k - \mu N\right)\right], \tag{2.3}$$

where the second sum is over the set $\{n_k\}$ that satisfies the total particle number N, and the sum appearing in the exponent is the total energy of all particles in the system (where we have n_k particles of energy ϵ_k). By defining the fugacity $z \equiv e^{\beta\mu}$,

$$\mathcal{Z}_s = \sum_{N=0}^{\infty} \sum_{\{n_k\}} \prod_k \left(z^{n_k} e^{-\beta n_k \epsilon_k}\right) \tag{2.4}$$

for which we may rearrange the various sums in the above to give that

$$\mathcal{Z}_s = \prod_k \left[\sum_{n_k} z^{n_k} e^{-\beta n_k \epsilon_k}\right]. \tag{2.5}$$

---

[1] For a more exhaustive description of ideal quantum gases and the present derivation outside the context of a lattice, see Chapter 6 of Ref. [63].

For fermions in a given state $|k\rangle$ with energy ϵ_k, the occupation number of that state may only be either $n_k = 0$ or $n_k = 1$; as such, the partition sum reduces to (the above may be computed for bosons by completing the geometric sum):

$$\mathcal{Z}_s = \prod_k \left[1 + z e^{-\beta\epsilon_k}\right]. \tag{2.6}$$

If we consider that the system is placed on a one-dimensional spatial lattice of extent N_x, then the product is taken over the discrete set $k = -N_x/2, -N_x/2+1, \ldots, N_x/2-1, N_x/2-1$ where $\epsilon_k = (2\pi k/N_x)^2/2m$. The total partition function for both spins is of course the product over such spins, $\mathcal{Z} = \mathcal{Z}_\uparrow \mathcal{Z}_\downarrow$. In order to compute thermodynamic observables, we are generally interested in $\ln \mathcal{Z}$ which is given by

$$\ln \mathcal{Z} = 2 \sum_{k=-N_x/2}^{N_x/2-1} \ln \left[1 + z \exp\left(\frac{-\beta}{2m}\left[\frac{2\pi k}{N_x}\right]^2\right)\right]. \tag{2.7}$$

The factor of two in front of the sum arises from the fact that the energy and chemical potential contributions to the for the second spin degree of freedom may be inserted additively in the exponential weight. Additionally, note that in future references to this expression, we will generally always set the fermion mass $m = 1$. The noninteracting pressure P_0 is directly related to $\ln \mathcal{Z}$,

$$P_0 = \frac{2}{\beta N_x^d} \sum_{k=-N_x/2}^{N_x/2-1} \ln \left[1 + z \exp\left(\frac{-\beta}{2m}\left[\frac{2\pi k}{N_x}\right]^2\right)\right], \tag{2.8}$$

(where N_x^d is the spatial d-dimensional volume), and the noninteracting density n_0 is related by a derivative with respect to μ,

$$n_0 = \frac{\partial \ln \mathcal{Z}}{\partial(\beta\mu)} = \frac{2}{N_x^d} \sum_{k=-N_x/2}^{N_x/2-1} \frac{1}{1 + z \exp\left(\frac{\beta}{2m}\left[\frac{2\pi k}{N_x}\right]^2\right)}. \tag{2.9}$$

If we wish to compute the noninteracting density n_0 in the continuum limit in one spatial dimension (taking the infinite volume limit while maintaining a constant finite density), we may perform a change of variables in Eq. (2.8) to a dimensionless quantity, $x = \beta p^2/2m$, and consider that the pressure in the continuum is

$P_0\lambda_T^3 = \sqrt{16\pi} I_0(z)$ where $\lambda_T \equiv \sqrt{2\pi\beta}$ is the thermal de Broglie wavelength and

$$I_0(z) = \int_{-\infty}^{\infty} dx \ \ln(1 + ze^{-x^2}). \tag{2.10}$$

Correspondingly, the density in the continuum limit is related to $I_0(z)$ by

$$n_0\lambda_T = \frac{2z}{\sqrt{\pi}} \frac{\partial I_0(z)}{\partial z}. \tag{2.11}$$

We will use these expressions for the noninteracting system in cases where a Monte Carlo calculation demonstrates convergence to the continuum limit. In the case of a two-component polarized gas, for which we will analyze the interacting case in this thesis, we modify the chemical potential for one species by a difference h such that $\mu_\uparrow = \bar{\mu} + h$ and $\mu_\downarrow = \bar{\mu} - h$, where $\bar{\mu}$ is the average chemical potential of the system, $\bar{\mu} = (\mu_\uparrow + \mu_\downarrow)/2$. By modifying the above derivation, it is straightforward to see that for the pressure P_0,

$$P_0 = \frac{1}{N_x^d} \left(\sum_{k=-N_x/2}^{N_x/2-1} \ln(1 + e^{\epsilon_k - \bar{\mu} - h}) \right) \left(\sum_{k=-N_x/2}^{N_x/2-1} \ln(1 + e^{\epsilon_k - \bar{\mu} + h}) \right) \tag{2.12}$$

where $\epsilon_k = 2\pi k/N_x$; the density for the polarized case still follows from Eq. (2.11).

Section 2.2: Auxiliary field representation of the partition function

In order to study the systems we are interested in using a stochastic technique, we must rewrite the grand-canonical partition function in a form that is tractable; namely, we must decompose the two-body interaction into a sum over one-body operators. We perform this change by the means of a *Hubbard-Stratonovich transformation*, where we introduce an auxiliary field σ which exists in the spatial and temporal dimensions of the system. We will provide an overview of this transformation in the following section.

Recall that the grand-canonical partition function for a general system of quantum particles is given by the trace over Boltzmann weights,

$$\mathcal{Z} = \mathrm{Tr}\left[e^{-\beta(\hat{H} - \mu\hat{N})} \right], \tag{2.13}$$

where $\beta = 1/k_B T$, $\hat{H}$ is the Hamiltonian operator, μ is the chemical potential, and $\hat{N}$ is the particle number operator. In order to study the thermodynamics of a system governed by a particular Hamiltonian in the most straightforward way, one must transform the operator $\hat{H}$ to a basis in which it is diagonal, which is a highly non-trivial task for the vast majority of interesting systems. In the case of interacting systems, the kinetic and potential energy operators do not commute ($[\hat{T}, \hat{V}] \neq 0$) which implies each N-particle subspace must individually be diagonalized. In addition, the size of the applicable single-particle basis and the number of degrees of freedom are typically very large. As such, most studies of quantum many-body systems turn to alternate routes that rewrites the problem in a form that is tractable by analytical or numerical means. In the majority of the approaches we use in the following work, we choose the rewrite the grand-canonical partition function as a path integral over a continuously-varying auxiliary field using a Hubbard-Stratonovich transformation.

Our natural goal for this problem is not necessarily to compute the partition function $\mathcal{Z}$ itself per se, but rather to compute *physical observables* for the Hamiltonian of interest, which can analytically be computed by taking derivatives of the partition function with respect to various sources, e.g. for an inserted source j where $j\hat{O}$ is added to the Hamiltonian,

$$\langle \hat{O} \rangle = \left. \frac{\delta \ln \mathcal{Z}(j)}{\delta j} \right|_{j=0} = \left. \frac{1}{\mathcal{Z}} \frac{\delta \mathcal{Z}(j)}{\delta j} \right|_{j=0}, \tag{2.14}$$

or one may follow the more conventional route of numerically computing the expectation value of some observable $\hat{O}$ via,

$$\langle \hat{O} \rangle = \frac{1}{\mathcal{Z}} \mathrm{Tr} \left[\hat{O} e^{-\beta(\hat{H} - \mu \hat{N})} \right]. \tag{2.15}$$

However, computing this in a naive manner by taking a complete trace over the Fock space is generally an intractable task; our present goal is to rewrite the problem in a form such that $\langle \hat{O} \rangle$ can be reasonably computed. The first step is to consider the Trotter-Suzuki factorization [64] of the *transfer matrix* $\mathcal{T}_\beta \equiv e^{-\beta \hat{H}}$, such that we discretize imaginary time (which is named as such if we consider $it \rightarrow \tau$),

$$\beta = \tau N_\tau \tag{2.16}$$

where τ is referred to as the temporal lattice spacing, and N_τ is the temporal volume in integer units. Given that $\hat{H} = \hat{T} + \hat{V}$, where $\hat{T}$ is the kinetic energy operator and $\hat{V}$ is the potential energy operator, we then proceed with the approximation

$$e^{-\tau\hat{H}} = e^{-\tau\hat{T}/2}e^{-\tau\hat{V}}e^{-\tau\hat{T}/2} + O(\tau^3), \tag{2.17}$$

which we truncate to order τ^2 under the requirement that τ is made appropriately small.

2.2.1: Hubbard-Stratonovich transformation for contact interactions

To proceed reformulating our problem of computing observables in a tractable form, we must specify the form of the Hamiltonian of interest. For all of the work developed here, we will study a system of fermions with zero-range contact interactions such that for a two-component system,

$$\hat{H} = \frac{\hat{p}_\uparrow^2 + \hat{p}_\downarrow^2}{2} - g\sum_x \hat{n}_{x,\uparrow}\hat{n}_{x,\downarrow} \tag{2.18}$$

where $\hat{p}_s$ are operators in momentum space for the subspace of component s, and $\hat{n}_{x,s}$ are density operators for the component s at the spatial lattice point x. The density operators may be expressed in terms of creation and annihilation operators as $\hat{n}_s = \hat{\psi}_s^\dagger\hat{\psi}_s$. When combined with a non-relativistic formalism on a lattice in one spatial dimension, this system is known as the Gaudin-Yang model [12, 13].

We will consider a transformation of the partition function for this Hamiltonian to one where the exponential of the two-body operator $\hat{V}$ is written as a field integral over a one-body operator in the presence of all possible external fields,

$$e^{-\tau\hat{V}} = \int \mathcal{D}\sigma\ \exp(-\tau\hat{V}_{\text{ext}}[\sigma]). \tag{2.19}$$

To proceed further explicitly we must specify the form of the interaction potential $\hat{V}$; here we will specify a *zero-range contact interaction* which will become the focus for the rest of the dissertation. Let us formally specify the interaction matrix as

$$\hat{V} = -g\sum_j \hat{n}_{\uparrow,x}\hat{n}_{\downarrow,x} \tag{2.20}$$

where the real constant g is the *bare coupling* which specifies the strength of the interaction, and the particle number operator is again $\hat{n}_{s,x} = \psi_{s,x}^\dagger\psi_{s,x}$. In one spatial dimension, the bare coupling is inversely proportional to the s-wave scattering length $a_0 = 2/g$. More generally, the bare coupling may be renormalized to quantities used for physical systems by means of Lüscher's formula [65–67], where the two-body energy spectrum is studied in a finite but continuous volume. For instance, in three spatial dimensions, the limit of low-energy scattering gives for momentum p and phase shift δ,

$$p \cot \delta(p) = -\frac{1}{a} + \frac{1}{2} r_{\text{eff}} p^2 + O(p^4) \tag{2.21}$$

where r_{eff} is the effective interaction range and a is the scattering length; the right hand side is a series expansion in even powers of p [68]. In a finite box of width L with periodic boundary conditions, the scattering phase shift is related to the momentum by [69]:

$$p \cot \delta(p) = \frac{1}{\pi L} \lim_{\Lambda \to \infty} S_\Lambda(\eta) \tag{2.22}$$

where Λ is the ultraviolet cutoff (defined on the lattice by the lattice spacing ℓ, and in the continuum $\lambda \longrightarrow \infty$), $\eta = pL/2\pi$, and

$$S_\Lambda(\eta) = \sum_{\mathbf{n}} \frac{\Theta(\Lambda^2 - \mathbf{n}^2)}{\mathbf{n}^2 - \eta^2} - 4\pi\Lambda. \tag{2.23}$$

Note that here $\Theta(x)$ is the Heaviside step function, and $\mathbf{n}$ is a vector of integers labeling the energy eigenstates; the sum is over all such states. A solution of the two-body energy spectrum $E_n = p_n^2/2m$ on the lattice provides the effective range expansion for sufficiently small energies. The bare coupling g may therefore be connected to the constants appearing the expansion of $p \cot \delta(p)$ via a solution of the scattering states for a single body in an external potential.

The ultimate goal of the Hubbard-Stratonovich transformation is to rewrite the interaction $\hat{V}$ in terms of a path integral over decoupled one-body operators that are more easily handled. There are multiple ways of writing a solution. The first step is to exactly state that (by noting that for fermions $\hat{n}^2 = \hat{n}$),

$$\exp(\tau g \hat{n}_{\uparrow,x} \hat{n}_{\downarrow,x}) = 1 + (e^{\tau g} - 1)\hat{n}_{\uparrow,x} \hat{n}_{\downarrow,x}, \tag{2.24}$$

where we will further introduce an *auxiliary field* variable σ and the parameter $A \equiv \sqrt{2(e^{\tau g} - 1)}$ such that for a continuous and compact transformation,

$$\exp(\tau g \hat{n}_{\uparrow,x}\hat{n}_{\downarrow,j}) = \int_{-\pi}^{\pi} \frac{d\sigma}{2\pi}(1 + A\hat{n}_{\uparrow,x}\sin\sigma)(1 + A\hat{n}_{\downarrow,x}\sin\sigma). \tag{2.25}$$

Notice that after contracting σ in Eq. (2.25) we recover Eq. (2.24); in a sense, this method is simply a rewriting of the interaction, but determining transformations for other interactions is generally nontrivial. This result also alludes to our first piece of evidence for the sign problem in terms of this system. In the case where $g < 0$, where we are in the regime of a repulsive interaction, A becomes complex, and as we will observe later, the probability measure for our Monte Carlo method becomes ill-defined.

To construct the full Hamiltonian, we should take a product of Eq. (2.25) over all lattice points (recall that $\hat{V}$ is written in terms of a spatial sum),

$$\begin{aligned} e^{-\tau\hat{V}} &= \prod_x e^{\tau g \hat{n}_{\uparrow,x}\hat{n}_{\downarrow,x}} && (2.26)\\ &= \prod_x \int_{-\pi}^{\pi}\frac{d\sigma}{2\pi}[1 + A\hat{n}_{\uparrow,x}\sin\sigma_t(x)][1 + A\hat{n}_{\downarrow,x}\sin\sigma_t(x)] && (2.27)\end{aligned}$$

where here we have explicitly noted that the matrix elements of σ are indexed by both space and imaginary time. Additionally, we must include the proper kinetic energy operator, noting that it is composed as a sum of operators for each component, $\hat{T} = \hat{T}_\uparrow + \hat{T}_\downarrow$, and therefore,

$$\begin{aligned} e^{-\tau(\hat{T}+\hat{V})} &= e^{-\tau\hat{T}/2}\left(\prod_x \int_{-\pi}^{\pi}\frac{d\sigma}{2\pi}[1 + A\hat{n}_{\uparrow,x}\sin\sigma_t(x)][1 + A\hat{n}_{\downarrow,x}\sin\sigma_t(x)]\right)e^{-\tau\hat{T}/2} && (2.28)\\ &= \prod_x \int_{-\pi}^{\pi}\frac{d\sigma}{2\pi}e^{-\tau\hat{T}_\uparrow/2}[1 + A\hat{n}_{\uparrow,x}\sin\sigma_t(x)]e^{-\tau\hat{T}_\uparrow/2} \times \\ &\qquad e^{-\tau\hat{T}_\downarrow/2}[1 + A\hat{n}_{\downarrow,x}\sin\sigma_t(x)]e^{-\tau\hat{T}_\downarrow/2}. && (2.29)\end{aligned}$$

Here we will define an operator that in generality appears for each component s, or flavor, in the system,

$$\hat{\mathcal{U}}_s(\sigma) \equiv e^{-\tau\hat{T}_s/2}[1 + A\hat{n}_{s,x}\sin\sigma_t(x)]e^{-\tau\hat{T}_s/2}, \tag{2.30}$$

giving that

$$e^{-\tau\hat{H}} = \prod_x \int_{-\pi}^{\pi}\frac{d\sigma}{2\pi}\hat{\mathcal{U}}_\uparrow(\sigma)\hat{\mathcal{U}}_\downarrow(\sigma). \tag{2.31}$$

The full Boltzmann weight for this system is given by the product of the above right hand side over all points in imaginary time,

$$e^{-\beta\hat{H}} = \prod_t^{N_\tau} \prod_x^{N_x} \int_{-\pi}^{\pi} \frac{d\sigma}{2\pi} \hat{\mathcal{U}}_\uparrow(\sigma)\hat{\mathcal{U}}_\downarrow(\sigma), \tag{2.32}$$

where we may formally define the transfer matrix of a single component as a product of $\mathcal{U}$ over all such points,

$$\mathcal{T}_s(\sigma) = \prod_t^{N_\tau} \mathcal{U}_s(\sigma). \tag{2.33}$$

We additionally define the path integral operator

$$\int \mathcal{D}\sigma = \prod_x \int_{-\pi}^{\pi} \frac{d\sigma_t(x)}{2\pi}, \tag{2.34}$$

such that

$$e^{-\beta\hat{H}} = \int \mathcal{D}\sigma\, \hat{\mathcal{T}}_\uparrow(\sigma)\hat{\mathcal{T}}_\downarrow(\sigma), \tag{2.35}$$

where after taking a trace over the Boltzmann weights,

$$\mathcal{Z} = \int \mathcal{D}\sigma\, \mathrm{Tr}[\mathcal{T}_\uparrow(\sigma)\mathcal{T}_\downarrow(\sigma)], \tag{2.36}$$

which can further shown to be written as

$$\mathcal{Z} = \int \mathcal{D}\sigma\, \det{}^2(1 + z\mathcal{U}[\sigma]), \tag{2.37}$$

where $z = \exp(\beta\mu)$. This form of the partition function, where the size of the matrix that is an argument to the determinant is of size $N_x^d \times N_x^d$ (rather than the full extent of spacetime), is known as the *BSS formalism*, first introduced by Blankenbecler, Scalapino, and Sugar in Ref. [70]. We will curiously note that although the smaller size of the matrix $\mathcal{U}$ provides a performance advantage in Monte Carlo calculations, it becomes prohibitively expensive to use in our perturbation theory formalism (discussed later in this dissertation), and it is actually better to return to the full fermion matrix, which is of extent $V \times V$.

To see how the trace is recast as a determinant, first note that the proof relies on the statistics of fermions; an analogous but different result which contains the inverse of the fermion determinant can be obtained for bosons. Recall that the operators that appear in $\mathcal{U}[\sigma]$ are of the form $\exp(-\tau\hat{T})$ and $\exp(-\tau\hat{V})$. Therefore, for a generic operator M_{ij} written in the occupation number basis (for which $a^\dagger$ and a are the creation and annihilation operators, respectively), consider its exponential such that we want to show

$$\mathrm{Tr}\left[\exp\sum_{i,j}a_i^\dagger M_{ij}a_j\right]=\det\left(1+e^M\right). \tag{2.38}$$

If M is transformed to a diagonal basis where for a unitary transformation U, $M = U^\dagger DU$ and $b = Ua$, $b^\dagger = a^\dagger U^\dagger$, then

$$\sum_{i,j}a_i^\dagger M_{ij}a_j=\sum_k b_k^\dagger D_k b_k=\sum_k D_k n_k, \tag{2.39}$$

where n_k is the occupation number of state k. Since b_k, $b_k^\dagger$ obeys the same fermion commutation relations as a_k, $a_k^\dagger$ under the unitary transformation, the trace over Fock space will give only $n_k = 0$ and 1. As such,

$$\mathrm{Tr}\left[\exp\sum_{i,j}a_i^\dagger M_{ij}a_j\right]=\prod_k\sum_{n_k=0,1}e^{D_k n_k}=\prod_k(1+e^{D_k})=\det(1+e^M), \tag{2.40}$$

where the last equality is made by the fact that the product is taken over all eigenvalues of M, which is equivalent to the determinant. A similar proof can be shown for a product of operators,

$$\mathrm{Tr}\left[\prod_i e^{a^\dagger A_i a}\right]=\det\left(1+\prod_i e^{A_i}\right), \tag{2.41}$$

from which Eq. (2.37) can be shown to hold.

Section 2.3: Difficulty of direct linear algebra and mean field approaches

The naive approach to computing basic equations of state from the Hamiltonian is to directly compute the trace over the spectrum as it appears in Eq. (2.1). Constructing the matrix elements of the Hamiltonian for the many-particle system is in itself a significant challenge, in the sense that the size of the many-particle basis grows exponentially with the number of particles in the system. Of course, such an approach involves accurately computing the eigenvalues of the Hamiltonian, which proves to be an challenging task. To compute the spectrum analytically, one would have to solve for roots of the characteristic equation which is a high-order polynomial – clearly such a goal would be fruitless. Finding such roots numerically are known to be sensitive to accumulation of error, particularly when the system is ill-conditioned, e.g. a significant number eigenvalues are close to and may lie on either side of zero. In this sense, it may be difficult to even have enough precision to accurately determine the signs of eigenvalues, which are critical to reasonably computing quantities of the partition function. However, highly-efficient software packages which perform exact diagonalization methods [71] do exist, but are generally not an appropriate choice for studying strongly-interacting systems at finite temperature. In this sense, we choose to exchange the problem of explicitly working with a large number of particles for high-dimensional integrals which are evaluated stochastically.

Another conventional approach to probe analytically intractable systems is via mean field, but it is generally known that these kinds of techniques are unable to capture important fluctuations which contribute to the thermodynamics. Nevertheless, let's take a very brief look at this method and see how it fails. We will simply attempt to compute the pressure P/P_0 of a weakly-interacting system in one spatial dimension, where P_0 refers to the pressure of the non-interacting counterpart. Mean field approaches generally improve in higher dimensions, so the 1D system is in a way a "worst-case" scenario for this type of analysis. The Hamiltonian can be built by taking advantage of the Fourier transform, where we define $\hat{H} = \hat{T} + \hat{V}$. The kinetic energy operator $\hat{T}$ can be constructed as a diagonal matrix in momentum space, where the elements T_n are given by (note that the fugacity z is absorbed into these matrix elements):

$$T_n = \frac{p_n^2}{2} - \mu \quad , \quad p_n = \frac{2\pi n}{L} \tag{2.42}$$

where the extent of the one-dimensional lattice is of L sites. The potential energy operator $\hat{V}$ for an attractive contact interaction controlled by the coupling strength g is correspondingly diagonal in coordinate space, where in this mean-field approach we simply take

$$\langle \hat{V} \rangle = -g \, \hat{n}_\uparrow(x) \, \hat{n}_\downarrow(x). \tag{2.43}$$

Here $\hat{n}_s$(x) corresponds to the density of the spin-1/2 free gas where $\hat{n}_\uparrow = \hat{n}_\downarrow$. The full Hamiltonian can therefore be constructed in coordinate space via

$$\hat{H} = U^\dagger \hat{T} U + \hat{V} \tag{2.44}$$

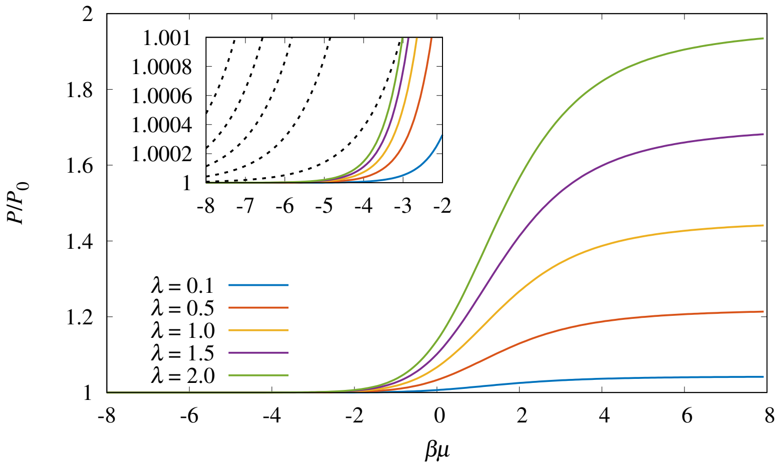

Figure 2.1: Result for the pressure P normalized by the non-interacting counterpart P_0 that is obtained when attempting a mean-field analysis for the interacting Hamiltonian. The results are shown for a variety of dimensionless couplings λ, which is related to the bare coupling by $\lambda = \sqrt{\beta}g$. Comparing to the result obtained via HMC in Fig. 3.2, we can see the result is somewhat qualitatively correct within the virial region, but the result is completely wrong for large values of $\beta\mu$. *Inset:* A comparison of the mean-field result with the second-order virial expansion of the pressure (shown as a dashed black line). Mean field fails to correctly quantitatively capture the behavior of the virial region.

where U is the Fourier transform matrix. We must therefore compute the eigenvalues ϵ_k for the interacting Hamiltonian H. An understanding of the relative bounds on the error of this operation may be obtained from the *condition number*, which provides an estimate of the error in the solution vector $\vec{x}$ based on the error in input vector $\vec{y}$ for the linear system $\mathbf{A}\vec{x} = \vec{y}$. Here we define the condition number $\kappa \equiv ||\mathbf{A}^{-1}||\,||\mathbf{A}||$, where a small condition number ($\kappa \sim 1$) indicates $\mathbf{A}$ is well-conditioned, and a large condition number will denote that it is ill-conditioned [72]. Depending on the choice of μ, we find that $\kappa \sim 10^2 - 10^5$, which confirms our suspicion that accurately extracting the spectrum could be a challenge. Indeed, when we attempt to compute the pressure from the interacting Hamiltonian for small choices of g, the result is incorrect compared to a variety of other methods developed throughout this dissertation; although, this limitation is of course due to the mean-field approach in addition to any numerical challenge. Fig. 2.1 shows the result for the pressure using mean-field approach for the one-dimensional system on a lattice size of $N_x = 61$ and temperature of $\beta = 8$. Although the results for the regime of $\beta\mu < 0$ are somewhat qualitatively correct, a comparison with the second-order virial expansion (see inset) indicates that the result is not accurate. More importantly, this mean field completely fails to capture the physics as the temperature is lowered toward large values of $\beta\mu$ where quantum mechanical effects dominate; the pressure P/P_0 should tend back toward the non-interacting value in this limit. Varying the lattice size N_x and temperature β does not improve this behavior by a significant amount.

Section 2.4: Finite-temperature determinantal Monte Carlo

Since we know that more straightforward approaches will not work for our studies of the systems we are interested in, we will turn to introducing the foundation for Monte Carlo techniques we use throughout this dissertation. All Monte Carlo techniques, in one form or another, use algorithms that rely on random numbers to study a problem of interest. As a small example, one may estimate the value of π using a simple Monte Carlo program. Consider a circle of radius a inscribed inside a square whose side length is $2a$. The program can choose N coordinate points (x, y) from a uniform distribution [such that $x, y \in (-a, a)$]. If k is the number of points that fall inside the circle, than approximately $\pi = 4k/N$. As $N \to \infty$, this approximation will improve. As a more relevant example of a Monte Carlo algorithm to this work, consider that we are attempting to numerically estimate the value of the integral of a one-dimensional function $f(x)$ over the domain (a, b), which may not necessarily be easily determined analytically. If we choose a suitable *weight function* or probability distribution $p(x)$ we can rewrite the integral as an expectation value:

$$\int_a^b f(x)\,dx = \int_a^b \frac{f(x)}{p(x)} p(x)\,dx = \left\langle \frac{f(x)}{p(x)} \right\rangle . \tag{2.45}$$

We can approximate the value of this integral by randomly sampling N values over the domain of x according to the probability distribution $p(x)$, and appropriately summing over all samples taken. The choice of how to properly select a set of x_i that will well-represent the integral being taken is a delicate one. Deciding on an algorithm to perform this sampling may be straightforward for a one-dimensional integral, but in the case of the many-body systems we will be looking at over the next several chapters, the integral we are attempting to estimate (the grand-canonical partition function, which is a path integral over the auxiliary field) has an incredible number of dimensions, which makes this issue drastically more complicated. In the remainder of this chapter, we will discuss the Monte Carlo sampling techniques we use for the quantum many-body problem.

In Sec. 2.2.1, we have rewritten the grand-canonical partition function $\mathcal{Z}$ as a path integral over an auxiliary field σ which casts the interaction matrix $\hat{V}$ as a one-body operator in an external field. Although this recasting makes working with this form of the partition function feasible, we must now in principle evaluate the path integral over all possible fields. To make such a problem fit on a computer of finite size, we must discretize the system on to a spacetime lattice to make the number of degrees of freedom of the auxiliary field finite. However, one would note that visiting every possible field configuration very quickly becomes impossible since the number of configurations scales exponentially with the spacetime volume; for instance, for a discrete field that takes on one of two states and is of a spacetime dimension $N_x^d \times N_\tau$, the number of configurations is $2^{N_x^d N_\tau}$. As is commonly seen in statistical mechanics, the vast majority of these configurations contribute negligibly to the dynamics of the system, and in reality, to study the relevant physics, we need only to visit the important contributions to the partition function. In order to do so in practice, we need to construct an algorithm which is capable of sampling such field configurations. In this section, we will discuss aspects of quantum Monte Carlo algorithms which serves as the foundation of stochastic calculations seen in this thesis.

When adding a source term to the Hamiltonian which contains the observable we wish to compute [see Eq. (2.14)], and take a derivative of $\ln \mathcal{Z}$ to compute $\langle \hat{O} \rangle$, if the partition function is written as a path integral

$$\mathcal{Z} = \int \mathcal{D}\sigma\, \mathcal{P}(\sigma), \tag{2.46}$$

we can arrive at something of the form

$$\langle \hat{O} \rangle = \frac{1}{\mathcal{Z}} \int \mathcal{D}\sigma\, \mathcal{P}(\sigma) \hat{O}(\sigma). \tag{2.47}$$

We can identify $\mathcal{P}(\sigma)$ as a probability measure that will govern our Monte Carlo simulation via *importance sampling*; in the case of fermionic systems, this probability measure will be given by a product of fermion determinants, as derived in a previous section. If we are given a total of N_σ samples of the auxiliary field σ that obey such a probability measure, than we can state that by a Monte Carlo calculation over a discretized field,

$$\langle \hat{O} \rangle = \frac{1}{N_\sigma} \sum_{\{\sigma\}} \hat{O}(\sigma), \tag{2.48}$$

whose measurement has an uncertainty of order $\mathcal{O}(1/\sqrt{N_\sigma})$ given independent samples. At this point, in order to compute an observable from the partition function we must design an efficient algorithm that samples the probability distribution with particular properties, such as decorrelation, reproducibility, ergodicity, and detailed balance. The *Metropolis-Hastings algorithm* satisfies these mathematical underpinnings that provides certain guarantees about the calculation. We will see later, however, that these guarantees are not always required to perform a Monte Carlo calculation and are even a source of issues in the context of the sign problem. In the case of the complex Langevin method, the Metropolis accept-reject step is replaced with the use of a stochastic noise term that is inserted in the action.

The Metropolis-Hastings algorithm produces a Markov chain of states σ that follows a particular probability (or weight) distribution. The algorithm defines a method of either accepting a proposed move to the next state in the Markov chain, or rejecting it, based on the probability of a system being in the proposed state relative to the current one. In the conventional description of the algorithm [73, 74], if a system in state s is proposed to move to a new state r, the total energies of each state E_s and E_r and the energy difference ΔE are calculated. The proposed step is automatically *accepted* if $\Delta E < 0$, otherwise, if $\Delta E > 0$ we choose a random number $R \in [0, 1]$, where

$$\text{if} \quad \begin{cases} R < \exp(-\beta\,\Delta E) & \text{accept the proposed state} \\ R > \exp(-\beta\,\Delta E) & \text{reject the proposed state} \end{cases} \tag{2.49}$$

In this manner, the algorithm can be shown to sample the states of higher probability for a given system. Note that if a proposed state is rejected, the current state is entered as the next state in the chain; that is, the attempt is not simply discarded from the Monte Carlo simulation. In the case of determinantal Monte Carlo, $\beta\,\Delta E$ in the Metropolis algorithm is replaced by an *action* in Euclidean time, $-S = \ln(\det^2 M)$ (or the equivalent appropriate fermion determinants for a system of study). Therefore, in the context of QMC, the partition function must generally be written in the path-integral form

$$\mathcal{Z} = \int \mathcal{D}\sigma(x,\tau)\, e^{-S[\sigma(x,\tau)]}, \tag{2.50}$$

where one may say we have integrated out the fermionic degrees of freedom and are left only with a path integral over a scalar field. In hybrid Monte Carlo, which we discuss next, we introduce a second auxiliary field that greatly increases the efficiency of the Metropolis sampling algorithm.

2.4.1: Hybrid quantum Monte Carlo

In the previous section, we discussed how the Metropolis-Hastings algorithm can accept or reject proposed states along a Markov chain, given the probability of a particular state occurring in a system of interest. However, we also need to consider how to properly propose the next random sample in the chain according to our distribution $P[\sigma]$. A naive approach may choose to flip one or more spins within a local area of the field configuration at a time, however, in the interest of achieving good correlation properties, it can be shown that a better approach is to propose *global* updates to the auxiliary field configuration. The hybrid Monte Carlo algorithm is known to efficiently achieve this proposal through the use of classical molecular dynamics.

In the hybrid Monte Carlo (HMC) algorithm [75], the value of the auxiliary field σ at each position in the spatial lattice $\mathbf{x}$ and imaginary time τ is updated according to classical Hamiltonian dynamics. As such, we introduce a new momentum auxiliary field variable π, where $\pi(\mathbf{x}, \tau)$ corresponds to the momentum of the lattice point $\sigma(\mathbf{x}, \tau)$ through configuration space. This flow of the field σ is governed by the Hamilton equations

$$\dot{\sigma} = \pi \qquad , \qquad \dot{\pi} = -\frac{\delta S_{\text{eff}}[\sigma, \pi]}{\delta \sigma}, \tag{2.51}$$

where the time derivative that appears is a new time coordinate that is distinct from the imaginary time τ, and $S_{\text{eff}}[\sigma, \pi]$ is the *effective action*. The conventional action $S[\sigma]$ is related to the probability distribution $P[\sigma]$ as

$$P[\sigma] = e^{-S[\sigma]}, \tag{2.52}$$

and the definition of the effective action includes the addition of the momentum field π,

$$S_{\text{eff}}[\sigma, \pi] = S[\sigma] + \int d\mathbf{x}\, d\tau\, \frac{[\pi(\mathbf{x}, \tau)]^2}{2}, \tag{2.53}$$

where the initial state of the momentum field is chosen from a normal distribution. Note that this field is reset to a new initial state after a HMC trajectory through configuration space is completed.

The derivative of the momentum field π requires a computation of the functional derivative of the effective action with respect to the auxiliary field σ. This derivative is taken for each point on the spacetime lattice such that $\dot{\pi}$ is a matrix of extent $N_x^d \times N_\tau$. We can compute the elementwise result according to

$$[\dot{\pi}]_{\mathbf{x},\tau} = -\frac{\partial S[\sigma]}{\partial \sigma_{\mathbf{x},\tau}} \tag{2.54}$$

where for a system of two flavors of fermions (note that we have absorbed the fugacity z into the definition of $\mathcal{U}[\sigma]$),

$$[\dot{\pi}]_{\mathbf{x},\tau} = \frac{\partial}{\partial \sigma_{\mathbf{x},\tau}} 2 \, \ln \det(1 + \mathcal{U}[\sigma]) \tag{2.55}$$

$$= 2 \, \mathrm{Tr} \left[\frac{1}{1 + \mathcal{U}[\sigma]} \frac{\partial \mathcal{U}[\sigma]}{\partial \sigma_{\mathbf{x},\tau}} \right]. \tag{2.56}$$

The partial derivative inside the trace evaluates to

$$\frac{\partial \mathcal{U}[\sigma]}{\partial \sigma_{\mathbf{x},\tau}} = \mathcal{U}_1 \mathcal{U}_2 \mathcal{U}_3 \cdots \frac{\partial \mathcal{U}_\tau[\sigma]}{\partial \sigma_{\mathbf{x},\tau}} \cdots \mathcal{U}_{N_\tau - 1} \mathcal{U}_{N_\tau}, \tag{2.57}$$

where $\frac{\partial \mathcal{U}_\tau[\sigma]}{\partial \sigma_{\mathbf{x},\tau}}$ has one non-zero element $A \cos \sigma_{\mathbf{x},\tau}$. Notice that in the non-interacting limit, $\dot{\pi} = 0$.

Notice that the action is analogous to the total energy E as discussed in the previous section; as such, some texts may refer to the effective action as a fictitious Hamiltonian, particularly since S_{eff} is a conserved quantity. In the systems we will be looking at throughout this thesis, the action will generally be proportional to the quantity $\ln \det M[\sigma]$, where M is known as the fermion matrix. The functional derivative is taken with respect to σ, which will generate inverses of the determinant – as such, it is important check that $\det M$ does not approach singularities in the course of our HMC algorithm. Under this formalism, the path integral form of the partition function is

$$\mathcal{Z} = \int \mathcal{D}\pi \, \mathcal{D}\sigma \exp(-S_{\text{eff}}[\sigma, \pi]), \tag{2.58}$$

where the path integral over π simply scales $\mathcal{Z}$ by an irrelevant scalar factor [76].

An advantage of using equations of motion for the evolution of σ which satisfy Hamilton's equations is the consequence of S being conserved from one state to the next. Since S_{eff} is held constant, ΔE as it appears in the Metropolis algorithm will be zero, and a proposed state *will always be accepted*, provided that the integration time step is small enough. This greatly increases the efficiency of the algorithm compared to those which may propose a significant fraction of states which will end up being rejected. Since this constant action corresponds to a fixed orbit in phase space, a new trajectory is started after each series of samples where the momentum field is reinitialized according to a Gaussian distribution.

In order to build the matrices $\mathcal{U}_i[\sigma]$ in practice, we can take advantage of *Fourier acceleration*, in which we construct the kinetic energy and interaction matrices in their respective diagonal representations, and apply one diagonal vector to the other in sequence by performing a fast Fourier transform (FFT) on

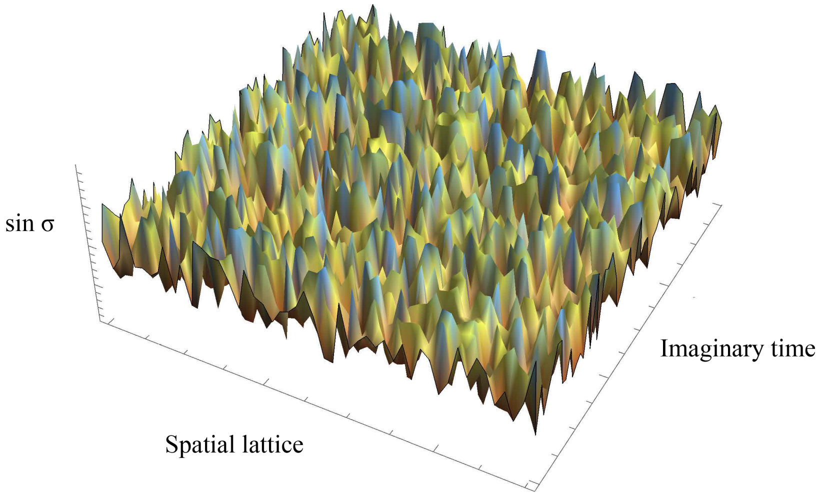

Figure 2.2: Rendering of an auxiliary field σ which is of spacetime extent $N_x \times N_\tau = 51 \times 60$ at a given point in its classical trajectory some time after thermalization has occurred. Note that the field is valid only at integer lattice points; the solid planes between such points are for visualization only.

one to the conjugate basis, and then perform the inverse transform on the product. This technique has the advantage in that the full dense operators in their non-diagonal representation does not need to be computed, and only vector multiplication need be performed. When an optimized FFT algorithm is used, such as the implementation FFTW [77], the transform is very fast.

One could be curious as to what the plot of a typical auxiliary field configuration may look like. Fig. 2.2 displays a rendering of such a field of extent $N_x \times N_\tau = 51 \times 60$ for at a given point in its classical trajectory after thermalization. It should be pointed out that although this plot is continuous for clarity, the field itself is discretized and is not valid at non-integer sites. If one were to watch the field evolve, the peaks and valleys would fluctuate up and down with no discernible pattern, yet different configurations that look similar to the eye can produce vastly different values for calculated observables. The corresponding momentum field, however, remains relatively static in comparison with the auxiliary field, with values slowly fluctuating about their initial condition.

2.4.2: Computing observables stochastically

Our primary goal in studying these physical systems is to compute equations of state such as the pressure and density. The route we have chosen to take involves sampling the set of field configurations according to a probability measure given by the partition function of the system. To obtain analytic expressions for computing these equations of state, first recall that for a real parameter λ and square matrix M,

$$\frac{d}{d\lambda}\det M(\lambda) = \det M(\lambda)\,\mathrm{Tr}\left[M^{-1}(\lambda)\frac{dM(\lambda)}{d\lambda}\right]. \tag{2.59}$$

Using this result, we obtain for the density n via a derivative with respect to μ,

$$n = \frac{2}{\mathcal{Z}}\int \mathcal{D}\sigma\,\det{}^2(1 + z\mathcal{U}[\sigma])\,\mathrm{Tr}\left(\frac{z\mathcal{U}[\sigma]}{1 + z\mathcal{U}[\sigma]}\right), \tag{2.60}$$

where we identify the probability measure as $P[\sigma] = \det^2(1 + z\mathcal{U}[\sigma])$ and the observable to be

$$O[\sigma] = \mathrm{Tr}\left(\frac{z\mathcal{U}[\sigma]}{1 + z\mathcal{U}[\sigma]}\right). \tag{2.61}$$

Performing this operation of course involves computing an inverse of $\mathcal{U}[\sigma]$. The pressure P and isothermal compressibility κ can be obtained by computing the integral and derivative of n with respect to $\beta\mu$, respectively. For the case of spin-polarized systems, where $\mu_\uparrow \neq \mu_\downarrow$,

$$\begin{aligned} n &= n_\uparrow + n_\downarrow = \left(\frac{d}{d(\beta\mu_\uparrow)} + \frac{d}{d(\beta\mu_\downarrow)}\right)\ln\mathcal{Z} &(2.62)\\ &= \frac{1}{\mathcal{Z}}\sum_{s=\uparrow,\downarrow}\int \mathcal{D}\sigma\left[\det(1 + z_\uparrow\mathcal{U}[\sigma])\,\det(1 + z_\downarrow\mathcal{U}[\sigma])\,\mathrm{Tr}\left(\frac{z_s\mathcal{U}[\sigma]}{1 + z_s\mathcal{U}[\sigma]}\right)\right]. &(2.63)\end{aligned}$$

We frequently find the *virial expansion* to be a useful tool in the regime where $z \simeq 0$. This expansion will be discussed in further detail in the next chapter, but it is interesting to point out here that the coefficients that appear in this power series expansion may be computed stochastically using a Monte Carlo algorithm. Consider that the virial expansion is given by

$$\ln\mathcal{Z} = Q_1\sum_{n=1}^{\infty} b_n z^n \tag{2.64}$$

where b_n are the virial coefficients, which one could write in terms of the canonical partition functions Q_n, e.g. at second order,

$$b_2 = \frac{1}{2Q_1}\left(2Q_2 - Q_1^2\right). \tag{2.65}$$

Notice that we may write these canonical partition functions in terms of various products of traces over the matrix $\mathcal{U}$, therefore allowing us to compute estimates of b_n stochastically. In practice, this numerical evaluation is tricky to perform since the scaling of Q_n with volume must be carefully canceled exactly to produce the intensive quantity b_n.

The punchline of the above discussion is that non-trivial observables may be computed when they are rewritten in terms of the field variable σ and placed under the path integral. Other quantities, such as the interaction energy, can also be obtained by taking derivatives of $\ln \mathcal{Z}$ with respect to other parameters, such as the bare coupling g or the temporal lattice spacing τ. We will see later that by computing the expectation value of the potential energy, we can determine a thermodynamic quantity of interest known as Tan's contact, which provides particular information about the momentum distribution.

CHAPTER 3: Strongly Interacting Fermi Gases in One Dimension

After summarizing the theoretical fundamentals of computing equations of state using auxiliary field and stochastic techniques, we will now move to determining results for strongly-interacting quantum gases. Throughout the next several chapters, we will study the thermodynamics of spin-1/2 fermions with a contact interaction given by the Gaudin-Yang model,

$$\hat{H} = -\frac{\hbar^2}{2m}\sum_i \nabla_i^2 - g\sum_{i<j}\delta(x_i - x_j), \tag{3.1}$$

where g is the bare coupling constant and the sum is taken over all particles. Throughout this work, we will take units such that $\hbar = m = 1$. In this chapter, we will restrict our study to the thermodynamics of one-dimensional unpolarized fermions (where $\mu_\uparrow = \mu_\downarrow$), but will cover weakly to strongly coupled regimes, as well as a wide variety of temperatures. Results for lattice Monte Carlo calculations will be presented for the particle number density n, the pressure P, the compressibility κ, and Tan's contact C.[1]

The Hamiltonian given in Eq. (3.1) clearly has a non-relativistic dispersion, indicating that the system may correspond to systems including the interacting low-temperature Fermi gas. The contact interaction is valid for the study of these kinds of systems in the limit where the gas is dilute enough such that the more complex form of the short-range interaction between fermions is not apparent, namely where the interparticle spacing k_F^{-1} is large enough (where k_F is the Fermi momentum). This interaction is characterized by a single parameter g which in one dimension is directly related to the s-wave scattering length by $g = 2/a_s$; the corresponding relationship between the value of g in our model and the strength of the physical interaction in higher spatial dimensions must be considered separately by studying the properties of the two-body spectrum in a finite volume [65].

The technique we use to compute the thermodynamic observables of interest here is hybrid Monte Carlo, as presented in Sec. 2.4.1. The two species of fermions is placed on a Euclidian space-time lattice of extent $N_x \times N_\tau$, where the lattice has periodic boundary conditions in the spatial direction and antiperiodic in the time direction; these boundary conditions become evident in the form of the Matsubara frequencies used for fermions. The physical spatial extent is $L = N_x \ell$, where we simply take $\ell = 1$ to set the length and momentum scales. The corresponding extent of the temporal lattice is set by the inverse temperature $\beta = 1/T = \tau N_\tau$. Throughout this work, we typically always use a time step of $\tau = 0.05$ (in lattice units) which balances temporal discretization effects with computational efficiency.

---

[1] This chapter is based upon the work published in Ref. [1].

The physical input parameters are clearly the inverse temperature β, the chemical potential μ, and for the case of this chapter, the attractive coupling strength $g > 0$. We choose to report all results in terms of two dimensionless quantities: the fugacity z and the dimensionless coupling λ, which are defined as

$$z = e^{\beta\mu} \quad \text{and} \quad \lambda^2 = \beta g^2. \tag{3.2}$$

Notice that for a fixed choice of g, taking $\lambda \to \infty$ at fixed μ corresponds to the zero-temperature limit.

Section 3.1: Equation of state results for the unpolarized system

We will most frequently present results in dimensionless form by normalizing the displayed quantities in units of their noninteracting counterparts at the same value of the input parameters, or by scaling it by the appropriate factor of the thermal wavelength $\lambda_T = \sqrt{2\pi\beta}$. The most natural output for our HMC calculations is the density equation of state $n(\lambda, \beta\mu)$, which we compute from the path-integral representation of $\mathcal{Z}$ by taking a analytic derivative of $\ln \mathcal{Z}$ with respect to $\beta\mu$, such that

$$n = \frac{2}{\mathcal{Z}} \int \mathcal{D}\sigma \, \det{}^2(1 + z\mathcal{U}[\sigma]) \, \mathrm{Tr}\left(\frac{z\mathcal{U}[\sigma]}{1 + z\mathcal{U}[\sigma]}\right), \tag{3.3}$$

where we sample the trace as our observable according to the probability measure $P[\sigma] = \det^2(1 + z\mathcal{U}[\sigma])$. We can obtain the pressure equation of state P by integrating the density with respect to $\beta\mu$,

$$P\lambda_T^3 = 2\pi \int_{-\infty}^{\beta\mu} n\lambda_T \, d(\beta\mu)', \tag{3.4}$$

where the integral in the $(\beta\mu)' \to -\infty$ limit is taken over the corresponding second-order virial expansion for the density. Correspondingly, taking a derivative of the density produces the isothermal compressibility

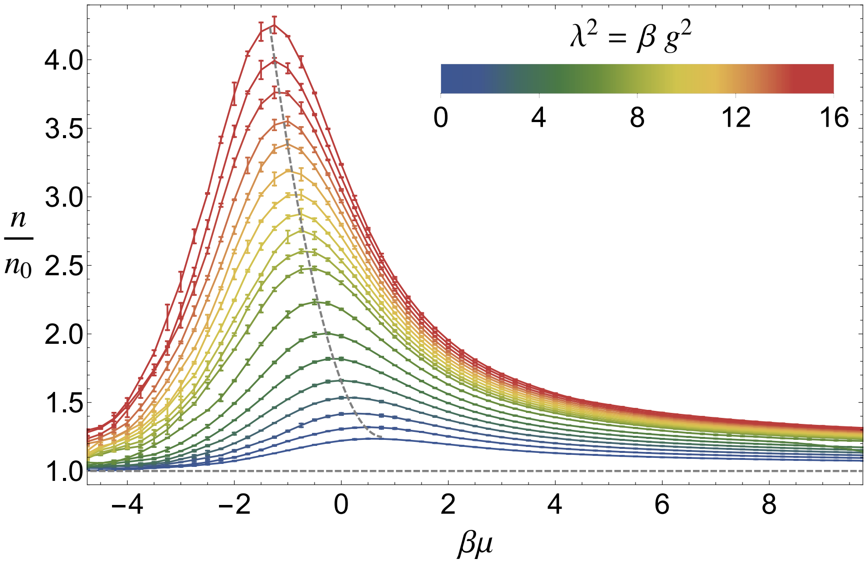

Figure 3.1: Density n, in units of the density of the noninteracting system n_0, as a function of the dimensionless chemical potential $\beta\mu$ and coupling λ. From bottom to top, the coupling is $\lambda = 0.0, 1.0, 1.25, 1.5, \ldots, 2.5, 2.75, 3.0, 3.1, 3.2, \ldots, 4.0$. The dashed line joins the maxima at each λ.

κ where

$$\kappa = \lambda_T^3 \frac{\sqrt{2\pi}}{(n\lambda_T)^2} \frac{\partial(n\lambda_T)}{\partial(\beta\mu)}\bigg|_\beta . \tag{3.5}$$

We display the results for these equations of state as computed using HMC below. In Fig. 3.1 we display the density n/n_0, in Fig. 3.2 we display the pressure P/P_0, and in Fig. 3.3 we display the isothermal compressibility κ/κ_0.

3.1.1: Calculating the second-order virial coefficient on the lattice exactly

The *virial expansion* is a power series expansion in the fugacity z of, most commonly, the pressure equation of state for a particular system. This expansion is valid in the high-temperature limit where $z \simeq 0$ (or correspondingly, where $\beta\mu \to -\infty$), and is useful because it captures the few-body dynamics which contribute to properties of the many-body system. The expansion is defined such that

$$\ln \mathcal{Z} = Q_1 \sum_{n=1}^{\infty} b_n z^n = Q_1(z + b_2 z^2 + b_3 z^3 + \cdots). \tag{3.6}$$

where $Q_1 = 2L/\lambda_T$ is the single-particle canonical partition function, and the *virial coefficients* are b_n. Note that we define $b_1 = 1$. It is also useful to recall the definition of the thermodynamic potential $\Omega = -PV$,

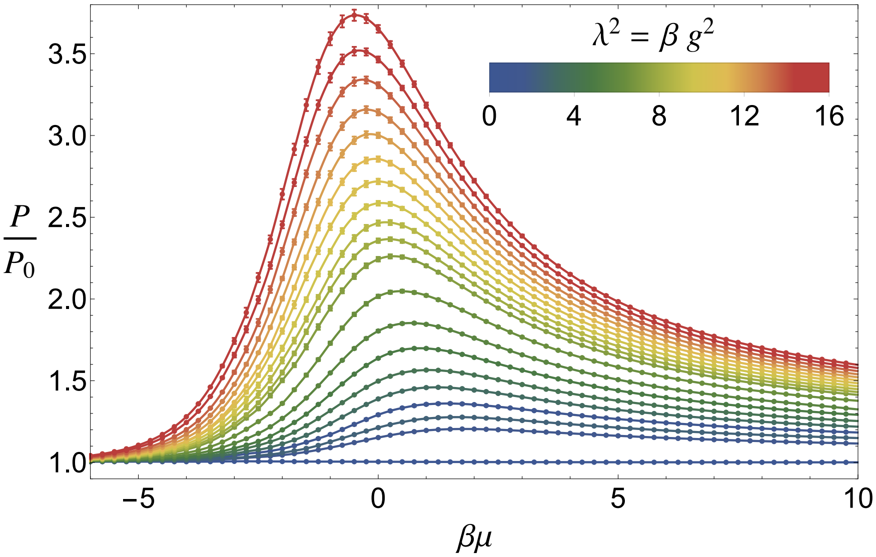

Figure 3.2: Pressure P, in units of the pressure of the noninteracting system P_0, as a function of the dimensionless chemical potential $\beta\mu$ and coupling λ, as obtained by $\beta\mu$ integration of the density. The values of λ shown in this plot are the same as in Fig. 3.1.

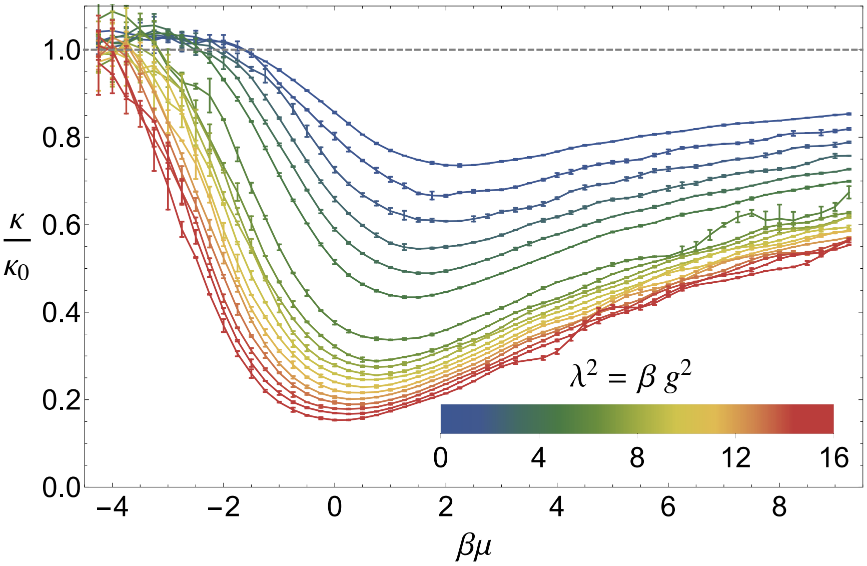

Figure 3.3: Isothermal compressibility κ, in units of the compressibility of the noninteracting system κ_0, as a function of the dimensionless chemical potential $\beta\mu$ and coupling λ, as obtained by $\beta\mu$ differentiation of the density. The values of λ shown in this plot are the same as in Fig. 3.1, but from top to bottom instead.

where $\ln \mathcal{Z} = -\beta\Omega$. These virial coefficients are real numbers which characterize the n-body contribution to $\ln \mathcal{Z}$; in general, these coefficients are difficult to compute since determining b_n involves solving the m-body spectrum for up to the n-body system. To see how this requirement comes about, we can compute useful expressions for b_n in terms of the canonical partition functions Q_n. Recall that

$$\mathcal{Z} = \sum_{n=0}^{\infty} Q_n z^n \tag{3.7}$$

so therefore,

$$z + b_2 z^2 + b_3 z^3 + \cdots = \frac{1}{Q_1} \ln\left(1 + Q_1 z + Q_2 z^2 + Q_3 z^3 + \cdots\right). \tag{3.8}$$

By expanding the logarithm on the right hand side and gathering terms at each order in z, we can see that

$$\begin{aligned} b_2 &= \frac{Q_2}{Q_1} - \frac{Q_1}{2} && (3.9)\\ b_3 &= \frac{Q_3}{Q_1} - Q_2 + \frac{Q_1^2}{3} && (3.10)\\ b_4 &= \frac{Q_4}{Q_1} - Q_3 - \frac{Q_2^2}{2Q_1} + Q_1 Q_2 - \frac{Q_1^3}{4} && (3.11)\\ &\vdots\ . \end{aligned}$$

It is evident that the expression for b_n involves up to and including Q_n, where we know that computing Q_n requires the n-body spectrum. However, at this point we can note that we should be able to compute b_2 exactly since it only involves the two-body problem, which can easily be solved in the center-of-mass frame using relative coordinates. As such, we will numerically compute the value of b_2 for Eq. (3.1) on the lattice (the result for b_2 in the continuum is provided in Ref. [1]) given a few choices of λ. Since this type of analysis is not affected by the sign problem, we can compute this coefficient for both attractive and repulsive couplings. Later in this dissertation, we will see how to calculate estimates for higher-order coefficients using lattice perturbation theory.

Computing non-interacting lattice virial coefficients

To begin our calculation of b_2, let's first overview the computation of the non-interacting counterpart. Recall the grand-canonical partition function for N_f flavors of non-interacting fermions on the lattice is

$$\ln \mathcal{Z}_0(z) = N_f \sum_n \ln\left(1 + z e^{-\beta p_n^2/2}\right) \tag{3.12}$$

where $p_n = 2\pi n/N_x$ and $n = -N_x/2, \ldots, N_x/2 - 1$. We know Q_1 (single fermions are non-interacting), and can determine $Q_2^{(0)}$ (the non-interacting counterpart of Q_2) from Eq. 3.7 by noting

$$Q_n = \frac{1}{n!} \left.\frac{\partial^n \mathcal{Z}}{\partial z^n}\right|_{z=0}. \tag{3.13}$$

By performing the Taylor expansion of Eq. (3.8) as discussed above, we can determine b_n for the non-interacting system by numerically evaluating the free Q_n, from which we find that in the continuum limit

$$b_2^{(0)} = -0.353553\ldots \tag{3.14}$$

$$b_3^{(0)} = 0.19245\ldots \tag{3.15}$$

$$b_4^{(0)} = -0.125. \tag{3.16}$$

Of course, the sum in grand-canonical partition function may be evaluated as an integral to find an analytic solution in the continuum, from which we find $b_n^{(0)} = (-1)^{n+1} n^{-3/2}$.

3.1.2: Tan's contact for the unpolarized system

We have also computed a thermodynamic quantity known as the contact (see Refs. [78–80]). Although much is known about this quantity in various situations (see, e.g., Ref. [81] for a review), the full temperature dependence in 1D was not previously known, to the best of our knowledge. By calculating the density as detailed above, one may use the Maxwell relation to calculate the contact C from n (see also Refs. [82–87]), or may use the Feynman-Hellman theorem to compute the contact directly from the expectation value of the potential energy,

$$C = -g\langle \hat{V} \rangle. \tag{3.17}$$

In order to characterize the contact within the virial region, it is useful to compute the virial expansion and corresponding coefficients for the contact. Recall that the virial expansion for the grand thermodynamic potential Ω is given by

$$-\beta\Omega = Q_1(z + b_2 z^2 + b_3 z^3 + \cdots) \tag{3.18}$$

where $Q_1 = 2L/\lambda_T$ is the single-particle canonical partition function, and the virial coefficients b_n are those corresponding to the density equation of state. Therefore, we may consider the virial expansion for the contact C to take the form

$$\beta C = \frac{2}{\lambda_T} Q_1(c_2 z^2 + c_3 z^3 + c_4 z^4 + \cdots), \tag{3.19}$$

where c_n may be related to b_n by

$$c_n = -\frac{\partial b_n}{\partial(a_0/\lambda_T)} = \sqrt{\frac{\pi}{2}}\lambda^2 \frac{\partial b_n}{\partial \lambda}. \tag{3.20}$$

The results for the contact as calculated by HMC, including the leading-order virial expansion (see inset) is displayed in Fig. 3.4. We show the statistical error in the inset; however, in the main plot, the smoothness of the results across $\beta\mu$ indicate that the statistical effects are of the order of the size of the symbols. As can be seen from the inset, the data captures the correct asymptotic behavior at small z for all values of λ shown, but the agreement slowly deteriorates at large λ, suggesting that the virial expansion breaks down earlier in that regime. In the limit of $\beta\mu \gg 1$ the contact satisfies

$$C\pi\beta^2/(2L\lambda^2) = \langle \hat{n}_\downarrow \hat{n}_\uparrow \rangle \pi\beta/2 \to \zeta_1 \beta\mu + \zeta_2 \tag{3.21}$$

where we find $\zeta_1 = 0.35(1)$ is nearly λ-independent. On the other hand, as is evident from the plot, ζ_2 is approximately linear in λ at large $\beta\mu$. We find $\zeta_2(\lambda) \simeq a + b\lambda$ with $a = -0.34(1)$ and $b = 0.701(5)$ at $\beta\mu = 10$. An analytic estimate in the absence of interactions yield $\zeta_1 = 1/\pi \approx 0.318$.

3.1.3: Extending the unpolarized system to more flavors

The above analysis has been performed for a system of fermions with two spin degrees of freedom, but can be extended to cases for a number of particle flavors greater than 2 ($N_f > 2$) by modifying the partition

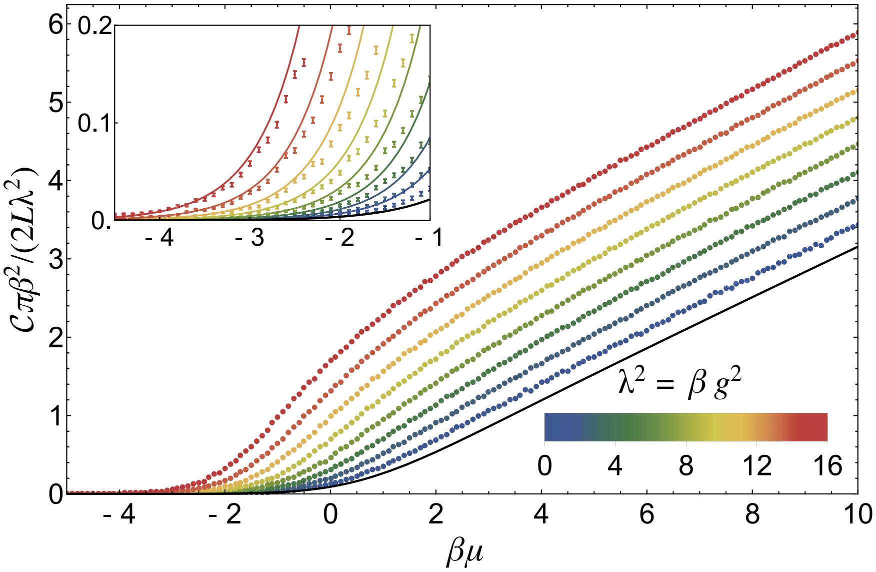

Figure 3.4: Tan's contact C scaled by $\beta\lambda_T/(2Q_1\lambda^2) = \pi\beta^2/(2L\lambda^2)$ as a function of $\beta\mu$. The black line shows C in the absence of interactions. *Inset:* Zoom-in of the main plot on the region $-4.5 \leq \beta\mu \leq -1.0$, also showing the leading-order virial expansion. Both plots show data for $\lambda = 0.5, 1.0, 1.5, \ldots, 4.0$, which appear from bottom to top.

function $\mathcal{Z}$ such that, for the unpolarized system of N_f flavors,

$$\mathcal{Z} = \int \mathcal{D}\sigma \, \det{}^{N_f}(1 + z\mathcal{U}[\sigma]). \tag{3.22}$$

The results of such an analysis are presented in Ref. [88]. We find that for a system of more flavors, the interaction is effectively greatly enhanced, and the density n/n_0 can increase by up to a factor of ~ 100 for the case of $N_f = 6$.

CHAPTER 4: Interacting Spin-Polarized Fermi Gases via Complex Chemical Potentials

In the previous chapter we studied the thermodynamic properties of an unpolarized Fermi gas; that is, the system of interest was such that the chemical potential of two species of fermions were equal ($\mu_{\uparrow} = \mu_{\downarrow}$). In the context of this dissertation, this is one the most elementary systems to consider, which allowed us to benchmark our algorithms and better understand the characterizing features of interacting systems. Naturally, one of the next steps in understanding this class of systems would be to ask about the equations of state for the case of polarized systems, where these chemical potentials were *not* equal. However, in such a case, hybrid Monte Carlo breaks down in the presence of a sign problem, which is generally a significant roadblock for lattice Monte Carlo calculations of asymmetric systems, for instance, systems with mass or spin imbalance [89–91], or systems at finite quark density in the context of QCD [92–97]. In order to navigate around such an obstacle, we introduce an imaginary chemical potential asymmetry such that the two chemical potentials are complex conjugates of one another.[1] In this case, the product of determinants that form the probability measure under the path integral is positive definite, and the quantum Monte Carlo method may be implemented as before. However, all observables now lie on the imaginary axis, and must be analytically continued to obtain the physical thermodynamics of the system. We will see later in Chapter 6 that the complex Langevin method, in which the auxiliary field is taken to be complex, reproduces the results here without resorting to an analytic continuation. Given the nature of the technique developed in this chapter, the method is sometimes referred to as *iHMC*.

Systems of spin-polarized, attractively interacting fermions, are particularly appealing because of the potential occurrence of spontaneously broken translation invariance in exotic superfluid phases [98, 99]. As a stepping stone toward these more interesting systems in higher dimensions, we focus here on the basic thermodynamic equations of state for fermions in one dimension, rather than on detecting potential exotic superfluid phases. In the upcoming sections, we compute the density, the spin magnetization, as well as Tan's contact, which encodes the importance of high-momentum correlations in systems with short-range interactions [68, 78–80, 82, 84, 85, 100–104].

---

[1] This chapter is based upon the work published in Ref. [2].

The Hamiltonian we analyze here is again the Gaudin-Yang model [12, 13],

$$\hat{H} = \frac{-\hbar^2}{2m} \sum_i \nabla_i^2 - g \sum_{i<j} \delta(x_i - x_j) \tag{4.1}$$

where both sums are over all particles. The partition function in the grand-canonical ensemble for such a system with two spin degrees of freedom is

$$\mathcal{Z}(\mu_\uparrow, \mu_\downarrow) = \operatorname{Tr} \exp[-\beta(\hat{H} - \mu_\uparrow \hat{N}_\uparrow - \mu_\downarrow \hat{N}_\downarrow)], \tag{4.2}$$

where μ_s is the chemical potential corresponding to particles of spin $s = \uparrow, \downarrow$, $\hat{N}_s$ is the corresponding particle number operator, and β is the inverse temperature.

Section 4.1: Observables, scales and computational technique

To characterize the thermodynamic properties of spin-polarized interacting fermions in one spatial dimension, we compute three physical quantities, namely the density n, the spin magnetization m, and Tan's contact C, as functions of the inverse temperature $\beta \equiv 1/k_B T$, the average chemical potential μ, the chemical potential difference h, and the coupling g. To make the independent quantities μ, h and g dimensionless, we scale by the appropriate factor of β; that is, using the same quantities used in the previous chapter, we report the physical results as functions of

$$\beta\mu, \quad \beta h, \quad \text{and} \quad \lambda \equiv \sqrt{\beta} g. \tag{4.3}$$

To make the measured quantities dimensionless, we scale the density and magnetization by the density of the unpolarized system n_0, where we report n/n_0 and m/n_0. In the case of the contact, we scale by C_0, the unpolarized result at $\beta\mu = 0$.

From the density and magnetization, one may obtain response functions such as the isothermal compressibility κ and the magnetic susceptibility χ simply by taking derivatives with respect to $\beta\mu$ and βh, respectively. Mixed response functions (of a derivative of n with respect to βh, or m with respect to $\beta\mu$) may also be obtained. Conversely, numerical integration of the density with respect to $\beta\mu$ provides the pressure P for each value of βh.

The computational methods used here for polarized systems is very similar to that of Refs. [6, 105, 106], but reduced to one spatial dimension and generalized to complex chemical potentials. One dimensional systems are relatively computationally inexpensive, and it is therefore possible to calculate on very large lattices, e.g. $N_x \approx \mathcal{O}(10^2)$. For such volumes, the continuum limit is easily reached by lowering the density while still remaining in the thermodynamic (many-particle) regime. As previously mentioned, for the spin-polarized case one encounters a sign problem which can be avoided by taking the complex chemical potential for each fermion species to be the complex conjugate of the other. The overall chemical potential $\mu = (\mu_\uparrow + \mu_\downarrow)/2$ is real as usual, but the asymmetry $h = (\mu_\uparrow - \mu_\downarrow)/2$ is imaginary. For convenience and clarity, we define the real parameter $h_\mathrm{I} := \mathrm{Im}\, h = -ih$. As such, the total density $n = n_\uparrow + n_\downarrow$ based on the grand-canonical ensemble is real, while the spin magnetization $m = n_\uparrow - n_\downarrow$ is imaginary. Each of these output observables must be analytically continued to the real-h axis in order to obtain the physical results. This procedure is achieved by fitting a given ansatz $f(\beta h_\mathrm{I})$ to the imaginary Monte Carlo results for each observable, and then taking the transformation $\beta h_\mathrm{I} \longrightarrow \beta h$ such that $\tilde{f}(\beta h)$ corresponds to proper density, magnetization, or contact. As will be discussed later in detail, the analytic continuation procedure introduces a degree of arbitrariness in the final results; however, it should be noted that the results on the imaginary side are fully non-perturbative and in principle exact up to controlled systematic and statistical uncertainties. Certain aspects of the functional dependence with respect to βh are known. For example, the symmetry under spin exchange as is apparent in the partition function indicates that the physics is independent of the sign of h; we expect our results to be either odd or even functions of h (and also h_I) depending on the quantity in question. Furthermore, it can be shown that the results for imaginary asymmetry will be 2π-periodic in βh_I (see Refs. [89, 90]), and is therefore a compact parameter which will be restricted to the interval $[-\pi, \pi]$.

For the calculations we present here, the dimensionless coupling is fixed at a value of $\lambda = 1$, although results for alternative couplings using this method are presented in Ref. [2]. This was chosen as being in the intermediate-to-strong coupling regime, which is typically outside the range of validity for low-order perturbative approaches. A spatial lattice volume of $N_x = 61$, which was fixed through this study, is sufficient to provide a quantitative understanding of the continuum limit (see Ref. [1]), in the sense that the thermal de Broglie wavelength $\lambda_T = \sqrt{2\pi\beta}$ is much smaller then the lattice spacing. The physical extent of the system is $L = N_x \ell$, and the extent of the temporal lattice is given by $\beta = \tau N_\tau$, where we take $\tau = 0.05/\ell^2$ and $\ell = 1$.

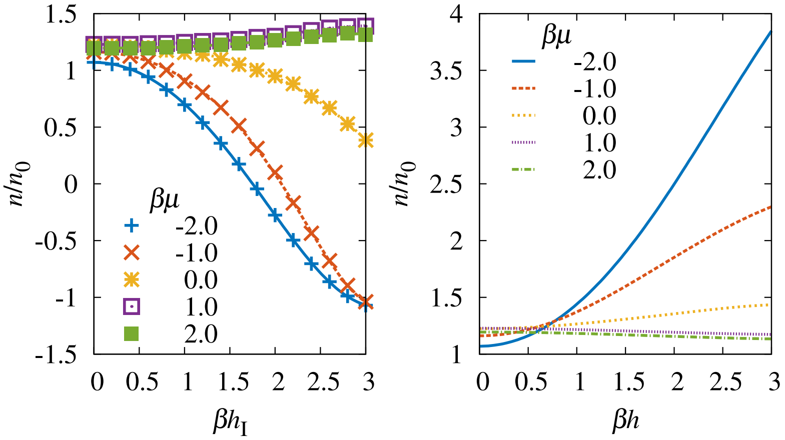

Figure 4.1: *Left:* Density as a function of the imaginary chemical potential difference βh_I at various values of $\beta\mu$. *Right:* Analytic continuation of the density as a function of βh. In both plots the density is an even function about the origin. Both plots are at a dimensionless coupling of $\lambda = 1.0$, and the physical quantities are plotted in units of the density of the noninteracting, unpolarized system.

Section 4.2: Monte Carlo results and the analytic continuation

Throughout the preceding calculations, we have fixed $\beta = 8$, $\lambda = 1$, and have a lattice size of $N_x = 61$. The chemical potential asymmetry parameter βh_I was varied over a full period $[-\pi, \pi]$, and the chemical potential parameter $\beta\mu$ was varied in the interval $[-4, 4]$, which covers the semiclassical regime (where the virial expansion is valid) to the fully quantum mechanical regime where interactions are the strongest. For each data point on the imaginary side in the plots below, we have taken 1000 de-correlated Monte Carlo samples, ensuring that the statistical uncertainty is below 10%.

In Fig. 4.1, we show the density n/n_0 as a function of βh_I and βh, respectively, for representative values of $\beta\mu$. Similarly, Fig. 4.2 displays the magnetization m/n_0 and Fig. 4.3 shows Tan's contact C. The statistical error of the Monte Carlo calculations on the imaginary side is estimated to be on the order of the symbol size in all three figures. In all cases we show the Monte Carlo results as a function of βh_I on the left panel, and the corresponding analytic continuation on the right. Although the imaginary side of the problem is not physically meaningful, it is reassuring that the data falls on smooth curves that respect even or odd symmetry around $\beta h_\mathrm{I} = 0$. We therefore have chosen to display only the positive interval $\beta h_\mathrm{I} \in [0, \pi]$.

As previously discussed, in order to obtain the results of physical interest, we need to analytically continue the data from our Monte Carlo study to real-valued chemical potential difference. To this end, we fit our data to a specific ansatz for each observable, of which the functional form is *a priori* unknown. It is known that such an ansatz must respect the correct symmetry about the origin and is formally periodic in βh_I. Further,

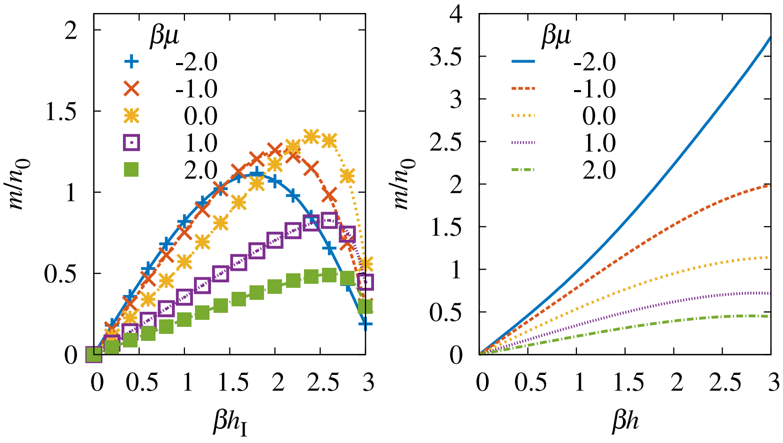

Figure 4.2: *Left:* Magnetization as a function of the imaginary chemical potential difference βh_I at various values of $\beta\mu$. *Right:* Analytic continuation of the magnetization as a function of βh. In both plots the magnetization is an odd function about the origin, are at a dimensionless coupling of $\lambda = 1.0$, and the physical quantities are plotted in units of the density of the noninteracting, unpolarized system.

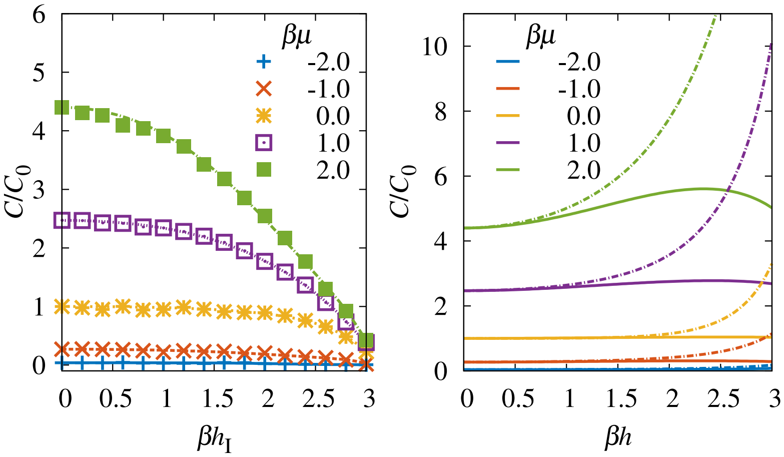

Figure 4.3: *Left:* Tan's contact as a function of the imaginary chemical potential difference βh_I at various values of $\beta\mu$ for a dimensionless coupling of $\lambda = 1.0$. C_0 is the contact at $\beta h = \beta\mu = 0$. *Right:* Analytic continuation of the contact as a function of βh at various values of $\beta\mu$. In both plots the contact is an even function about the origin. The curves on the right are color-wise paired by their value of $\beta\mu$, which coincides with the value on the left (by color code, or from top to bottom). Dashed-dotted lines give the results from a fit of the data to the polynomial-type ansatz (4.10), whereas solid lines result from fits of the data to our Padé-type ansatz (4.8) for the fit functions.

the virial expansion of the grand-canonical partition function suggests that it may be written as an asymptotic series in powers of $\cos(\beta h_{\mathrm{I}})$, from which it follows that higher-order terms become particularly important for the strongly-interacting regime $\beta\mu > 1$. To take such a high-order expansion into account, an ansatz of the Padé approximant of cosines,

$$\sim \frac{1}{1 + \cos(\beta h_{\mathrm{I}})} \tag{4.4}$$

may be considered appropriate as it may be written as an asymptotic series in powers of $\cos(\beta h_{\mathrm{I}})$ which still obeys the periodicity in βh_{I}.

Specifically, we choose to fit our Monte Carlo results for the magnetization at finite βh_{I} with the odd function

$$f(\beta h_{\mathrm{I}}) = -i \frac{\mathcal{A} \sin(\beta h_{\mathrm{I}})}{1 + \mathcal{B} \cos(\beta h_{\mathrm{I}}) + \mathcal{C} F(\beta h_{\mathrm{I}})} \tag{4.5}$$

where $\mathcal{A}$, $\mathcal{B}$, and $\mathcal{C}$ are real-valued fit parameters and the function F is given by

$$F(x) = \cos(x^3/\pi^2). \tag{4.6}$$

This last function was determined empirically. As written, it is analytic on the whole complex plane, in particular on a disk of radius π centered at the origin. However, it is clearly not periodic in βh_{I} as we demanded earlier. We have given up this constraint as practically a large number of fit parameters is required to meet this criterion, rendering the fitting algorithm potentially unstable. For example, a true Padé ansatz of the form $\sim \sum_{k=1} \mathcal{A}_k \sin(k\beta h_{\mathrm{I}})/[1 + \sum_{k=1} \mathcal{B}_k \cos(k\beta h_{\mathrm{I}})]$ is compatible with the previously mentioned constraints; however, the fit is consistently of much lower quality then those obtained using Eq. (4.5). In fact, in most cases the parameter $\mathcal{C}$ associated with the function F is found to be small. Formally, since the domain of βh is restricted to $[-\pi, \pi]$, we define a periodic Fourier series of Eq. (4.5) valid within only that interval.

The analytic continuation $\tilde{F}(\beta h)$ of Eq. (4.5) is simply obtained by setting $h_{\mathrm{I}} = -ih$, which is therefore given by

$$\tilde{f}(\beta h) = -\frac{\mathcal{A} \sinh(\beta h)}{1 + \mathcal{B} \cosh(\beta h) + \mathcal{C} \tilde{F}(\beta h)}, \tag{4.7}$$

where $\tilde{F}$ is the analytic continuation of F, $\tilde{F}(x) = \cosh(x^3/\pi^2)$.

In the case of the density n/n_0 and Tan's contact C/C_0, we expect even functions of βh_{I}, and therefore have chosen to fit the function

$$g(\beta h_{\mathrm{I}}) = \gamma \left[\frac{1 + \mathcal{A}\eta(\beta h_{\mathrm{I}})}{1 + \mathcal{B}\eta(\beta h_{\mathrm{I}}) + C\eta[(\beta h_{\mathrm{I}})^3/\pi^2]} \right] \tag{4.8}$$

where $\eta(x) = 1 - \cos(x)$. Here, γ is a parameter that is fixed by the exactly known value at $\beta h = \beta h_{\mathrm{I}} = 0$, while $\mathcal{A}$, $\mathcal{B}$ and C are free real-valued parameter. Once the set of parameters are obtained, the analytic continuation $\tilde{g}(\beta h)$ of Eq. (4.8) is given by

$$\tilde{g}(\beta h) = \gamma \left[\frac{1 + \mathcal{A}\tilde{\eta}(\beta h)}{1 + \mathcal{B}\tilde{\eta}(\beta h) + C\tilde{\eta}[(\beta h)^3/\pi^2]} \right] \tag{4.9}$$

where $\tilde{\eta}(x) = 1 - \cosh(x)$.

The fit parameters for the density, magnetization, and Tan's contact are provided in Tables 4.1, 4.2, and 4.3, respectively. Since the fits to the Monte Carlo data are sensitive to initial parameter values, the fitting algorithm performs several such fits with random initial parameter values in the interval $[-1, 1]$, and the best fit with the minimum mean residuals is chosen for the analytic continuation. Given the functional form of Eqs. (4.5) and (4.8), one should consider that poles may appear in either the fit or analytic continuation for a given set of fit parameters. Since we expect these quantities to be analytic for one dimensional Fermi gases, the fitting algorithm eliminates any fits that demonstrate such behavior. Of course, other functional forms may be considered for the analytic continuation with consideration to the constraints already discussed.

Note that in Fig. 4.1 we also show the analytic continuation of the density, in Fig. 4.2 of the magnetization, and in Fig. 4.3 of Tan's contact to real-valued chemical potential differences. Although these functions are not periodic in βh (which is not expected to be a constraint), they remain valid only in the original restricted domain of $[-\pi, \pi]$. A few representative values of $\beta\mu$ are shown in each of these figures, however such analytic continuations may be performed for many values of $\beta\mu$ on an unrestricted domain, and the equations of state for various imaginary asymmetries may be constructed. Such plots for representative values of βh at a dimensionless coupling strength of $\lambda = 1$ for the density, magnetization, and Tan's contact are shown in Figs. 4.6 and 4.7.

One of the more interesting features we observe in our results is in the behavior of the magnetization

Table 4.1: Fit parameters for the density as they appear in Eq. (4.8) at a constant dimensionless coupling of $\lambda = 1.0$ for various values of $\beta\mu$, as well as the χ^2 per degree of freedom for each fit. Note that γ is not a fit parameter (see main text).

$\beta\mu$	γ	$\mathcal{A}$	$\mathcal{B}$	$\mathcal{C}$	χ^2
-3.6	1.0080	-0.9670(4)	-0.0415(10)	-0.001(1)	0.71
-3.2	1.0172	-0.9511(4)	-0.0565(9)	-0.0022(10)	0.58
-2.8	1.0294	-0.9281(4)	-0.080(1)	-0.006(1)	0.54
-2.4	1.0461	-0.8942(9)	-0.118(3)	0.005(3)	1.29
-2.0	1.0698	-0.848(1)	-0.156(3)	-0.000(4)	1.66
-1.6	1.1026	-0.7904(6)	-0.198(2)	-0.016(2)	0.35
-1.2	1.1245	-0.7156(10)	-0.276(3)	-0.008(4)	1.25
-0.8	1.1731	-0.6334(6)	-0.323(2)	-0.019(3)	0.63
-0.4	1.1921	-0.5433(9)	-0.364(4)	-0.034(7)	1.30
0.0	1.2240	-0.492(2)	-0.415(2)	-0.056(5)	2.74
0.4	1.2359	-0.503(3)	-0.493(3)	-0.009(1)	5.21
0.8	1.2361	-0.4(1)	-0.4(1)	0.00(1)	0.54
1.2	1.2214	-0.18(5)	-0.22(5)	-0.013(6)	0.97
1.6	1.2109	-0.32(2)	-0.34(2)	0.004(1)	0.71
2.0	1.1948	-0.33(3)	-0.35(3)	0.005(2)	1.81
2.4	1.1763	-0.22(2)	-0.24(2)	-0.002(1)	0.41
2.8	1.1625	-0.11(3)	-0.13(3)	-0.007(1)	0.43
3.2	1.1507	-0.20(3)	-0.22(3)	-0.001(1)	0.45
3.6	1.1397	-0.07(6)	-0.08(6)	-0.009(3)	0.60

m/n_0 as a function of βh and $\beta\mu$. On the imaginary side (at least in the region studied), this quantity is non-monotonic in both of those variables. In particular, we note that the ordering of the curves as a function of βh, for differing values of $\beta\mu$, is partially inverted at large enough βh. This behavior, however, results in a perfectly ordered set of curves on the real-valued side in a way that respects both thermodynamic stability and physical intuition.

In Fig. 4.3 we show two possible fits and their corresponding analytic continuations for the contact, namely the Padé form given in Eqs. (4.8) and (4.9), as well as a polynomial function

$$q(\beta h_{\mathrm{I}}) = \gamma \left[1 + \mathcal{A}\eta(\beta h_{\mathrm{I}}) + \mathcal{B}\eta([\beta h_{\mathrm{I}}]^3)/\pi^2)\right], \tag{4.10}$$

where again $\mathcal{A}$ and $\mathcal{B}$ are real-valued fit parameters, $\eta(x) = 1 - \cos(x)$, and γ is a fixed value, as discussed previously. The analytic continuation $\tilde{q}(\beta h)$ is given in terms of $\tilde{\eta}(x)$. While the fits on the imaginary side appear to be of comparable quality, they differ enough in the details that their analytic continuation to the real side displays noticeable discrepancies. This is particularly evident for large $\beta\mu$. We take this to be indicative

Table 4.2: Fit parameters for the magnetization as they appear in Eq. (4.5) at a constant dimensionless coupling of $\lambda = 1.0$ for various values of $\beta\mu$, as well as the χ^2 per degree of freedom for each fit.

$\beta\mu$	$\mathcal{A}$	$\mathcal{B}$	$\mathcal{C}$	χ^2
-3.6	1.022(4)	0.044(3)	0.011(5)	0.48
-3.2	1.031(4)	0.062(3)	0.011(5)	0.50
-2.8	1.048(3)	0.094(3)	0.012(4)	0.41
-2.4	1.047(6)	0.146(5)	-0.015(6)	1.01
-2.0	1.062(5)	0.202(4)	-0.023(6)	1.35
-1.6	1.098(4)	0.269(3)	0.000(4)	0.48
-1.2	1.134(4)	0.387(3)	0.017(4)	1.80
-0.8	1.142(3)	0.521(3)	0.037(3)	5.81
-0.4	1.089(4)	0.632(3)	0.052(3)	8.90
0.0	0.978(3)	0.702(2)	0.067(2)	23.32
0.4	0.833(3)	0.711(3)	0.088(3)	36.24
0.8	0.695(3)	0.684(3)	0.123(3)	7.36
1.2	0.574(2)	0.660(3)	0.156(3)	4.95
1.6	0.473(2)	0.651(3)	0.175(3)	7.57
2.0	0.397(2)	0.639(4)	0.193(4)	8.02
2.4	0.340(2)	0.630(5)	0.214(5)	11.10
2.8	0.292(2)	0.634(6)	0.215(6)	14.55
3.2	0.256(1)	0.638(5)	0.218(4)	14.73
3.6	0.227(2)	0.636(7)	0.218(7)	24.89

of the limitations of our approach, and should be viewed as a warning with respect to the choice of the fit function. The Padé form given in Eq. (4.8) effectively takes into account arbitrarily high powers of $\cos(\beta h_\mathrm{I})$ which is expected to be valid only in the vicinity of vanishing polarization.

Section 4.3: Magnetization-to-density ratio and magnetic susceptibility

It is important to understand whether the system we are studying is appreciably magnetized in the region of parameter space that we explore here. To clarify and expand on this point, in Fig. 4.4 we show the ratio of the magnetization m to the density n. In absolute value, this ratio can only vary between 0 (unpolarized) and 1 (fully polarized); it is therefore reassuring that m/n in fact lies within the interval $[0, 1]$ after analytic continuation, and is a monotonically increasing function with βh.

Our results for the magnetization allow us to compute the magnetic susceptibility χ of a polarized Fermi gas simply by taking a derivative,

$$\chi = \frac{1}{n_0}\frac{\partial m}{\partial(\beta h)}, \tag{4.11}$$

Table 4.3: Fit parameters for the contact as they appear in Eq. (4.8) at a constant dimensionless coupling of $\lambda = 1.0$ for various values of $\beta\mu$, as well as the χ^2 per degree of freedom for each fit. Note that γ is not a fit parameter (see main text).

$\beta\mu$	γ	$\mathcal{A}$	$\mathcal{B}$	C	χ^2
-3.6	0.0003	-0.4(2)	-0.60(4)	0.15(4)	0.47
-3.2	0.0019	-0.50(5)	-0.50(3)	-0.00(5)	0.52
-2.8	0.0062	-0.503(2)	-0.10(5)	-0.40(8)	0.12
-2.4	0.0159	-0.5(1)	-0.40(9)	0.4(6)	1.01
-2.0	0.0390	-0.45(8)	-0.39(6)	0.3(4)	1.30
-1.6	0.0971	-0.5025(5)	-0.22(2)	-0.27(3)	0.42
-1.2	0.1712	-0.49(1)	-0.42(1)	-0.00(4)	0.98
-0.8	0.3542	-0.496(2)	-0.418(4)	-0.051(10)	0.32
-0.4	0.5722	-0.493(2)	-0.473(3)	0.006(8)	0.64
0.0	1.0000	-0.496(1)	-0.464(3)	-0.016(6)	1.02
0.4	1.4929	-0.4974(7)	-0.450(2)	-0.029(4)	0.70
0.8	2.1795	-0.4978(7)	-0.402(2)	-0.075(4)	0.60
1.2	2.7994	-0.494(1)	-0.386(2)	-0.061(6)	0.49
1.6	3.6330	-0.4986(7)	-0.331(3)	-0.138(7)	1.09
2.0	4.3998	-0.498(1)	-0.304(4)	-0.16(1)	2.21
2.4	5.0691	-0.4980(5)	-0.298(2)	-0.157(5)	0.61
2.8	5.8386	-0.4975(5)	-0.278(2)	-0.166(5)	0.53
3.2	6.6344	-0.4967(7)	-0.256(2)	-0.180(7)	0.69
3.6	7.3683	-0.4982(6)	-0.240(2)	-0.211(6)	0.85

where in practice we simply take an analytic derivative of Eq. (4.7) for each discrete value of $\beta\mu$. The magnetic susceptibility as a function of βh for representative values of $\beta\mu$ at a fixed dimensionless coupling of $\lambda = 1.0$, as well as the noninteracting case, is shown in Fig. 4.5.

Section 4.4: Comparison with other approaches

In this section, we compare the results from the Monte Carlo simulations with those from other approaches which helped guide the analytic continuation of the numerical data from imaginary to real-valued chemical potential differences.

4.4.1: Virial expansion

Consider the virial expansion of the partition function, i.e. an expansion in powers of $z \equiv e^{\beta\mu}$. In the $\beta\mu \to -\infty$ limit, where the virial expansion is valid, we can evaluate the density and the magnetization order by order. At leading order in z, $n_{\uparrow,\downarrow}\lambda_T = z_{\uparrow,\downarrow}$, and therefore

$$n\lambda_T = (n_\uparrow + n_\downarrow)\lambda_T = 2e^{\beta\mu}\cosh(\beta h) \tag{4.12}$$

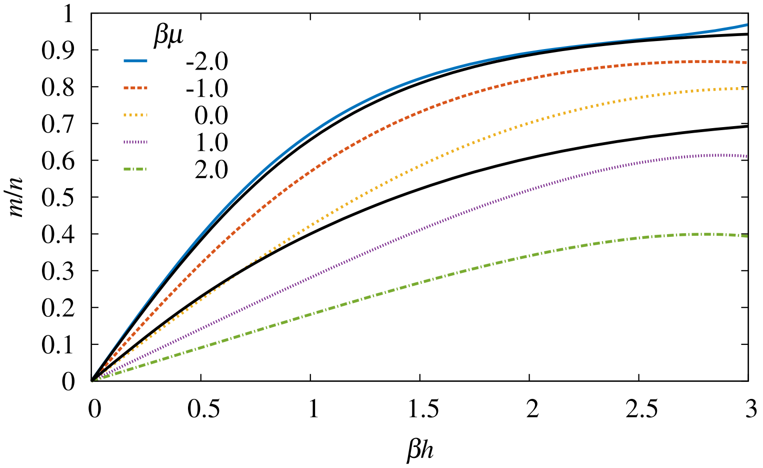

Figure 4.4: Ratio of the magnetization m to the density n as a function of the real-valued βh and $\beta\mu = -2.0, -1.0, 0, 1.0, 2.0$. The solid lines show the second-order virial expansion at $\beta\mu = -2$ (top) and -1 (bottom). Note that the virial expansion works well for $\beta\mu = -2$, but fails dramatically for $\beta\mu = -1$ and above; see Sec. 4.4.1 for details.

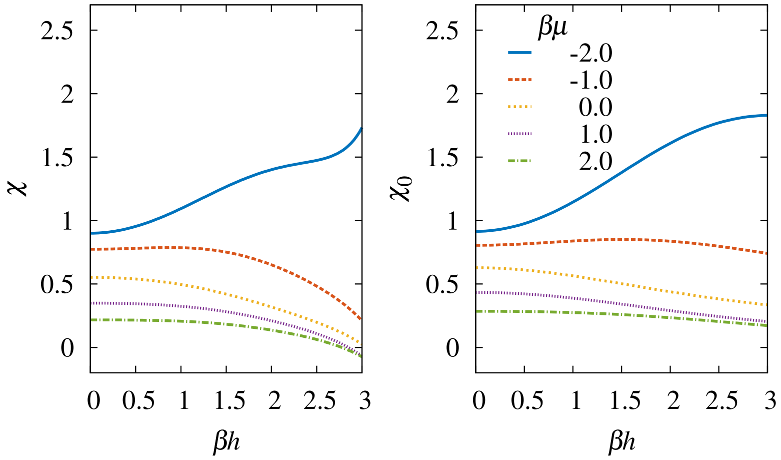

Figure 4.5: The magnetic susceptibility χ as a function of βh at representative values of $\beta\mu$, obtained by taking an analytic derivative of the magnetization with respect to βh. *Left:* Interacting case at $\lambda = 1$. *Right:* Noninteracting case in the continuum.

which leads to, noting that $n_0 = 2z_\uparrow z_\downarrow$ at leading order,

$$\frac{n}{n_0} = \cosh(\beta h) \tag{4.13}$$

where n_0 is the density for the unpolarized system. This result is the leading order in the virial expansion and therefore is independent of the interaction. Similarly, we find for the magnetization that

$$\frac{m}{n_0} = \frac{n_\uparrow - n_\downarrow}{n_0} = \sinh(\beta h), \tag{4.14}$$

which then at leading order in z yields

$$\frac{m}{n} = \tanh(\beta h). \tag{4.15}$$

In general, accessing higher orders in the virial expansion requires solving the two-, three-, . . . , N-body problem (see, e.g., Ref. [81]). The grand-canonical partition function for systems with a chemical potential asymmetry may be written as

$$\mathcal{Z} = \sum_{N=0}^{\infty} \sum_{M} z^N w^M Q_{N_\uparrow, N_\downarrow}, \tag{4.16}$$

where $N = N_\uparrow + N_\downarrow$ is the total particle number and $M = N_\uparrow - N_\downarrow$ measures the spin polarization. Moreover, we have introduced the quantities $w \equiv e^{\beta h}$ and $Q_{N_\uparrow, N_\downarrow}$ being the canonical partition function of a system with $N_\uparrow$ spin-up fermions and $N_\downarrow$ spin-down fermions. Expanding Eq. (4.16) to second order in z yields

$$\mathcal{Z} = 1 + 2Q_{1,0} z \cosh(\beta h) + Q_{1,1} z^2 + 2Q_{2,0} z^2 \cosh(2\beta h) + \mathcal{O}(z^3), \tag{4.17}$$

where $Q_{1,0} = L/\lambda_T$ and $Q_{1,1}$ and $Q_{2,0}$ may be determined by direct calculation [1] without determining the explicit form of the partition function. Note that the expansion coefficients $Q_{N_\uparrow, N_\downarrow}$ depend implicitly on the coupling λ. To determine all coefficients, recognize that the expression for b_2 in terms of the generic canonical partition functions Q_1 and Q_2 is given as

$$b_2 = \frac{Q_2}{Q_1} - \frac{Q_1}{2} \tag{4.18}$$

where for the present polarized system, for the interacting case $Q_2 = 2Q_{2,0} + Q_{1,1}$ and $Q_1 = 2Q_{1,0}$ since the exchange of spin-up particles for spin-down particles is symmetric (i.e., $Q_{1,0} = Q_{0,1}$). This gives for the interacting system at $\lambda = 1$ on the lattice,

$$b_2 = -0.035 = \frac{2Q_{2,0} + Q_{1,1}}{2Q_{1,0}} - Q_{1,0}. \tag{4.19}$$

In the case of the non-interacting system, $Q_{1,1} = Q_{1,0}^2$ so the above reduces to

$$b_2^{(0)} = -0.35355\cdots = \frac{Q_{2,0}}{Q_{1,0}} - \frac{Q_{1,0}}{2}. \tag{4.20}$$

Solving Eqs. (4.19) and (4.20) simultaneously gives the result

$$\begin{aligned} Q_{1,1} &= 2(b_2 - b_2^{(0)})Q_{1,0} + Q_{1,0}^2 && (4.21)\\ Q_{2,0} &= \frac{1}{2}Q_{1,0}(2b_2^{(0)} + Q_{1,0}) && (4.22)\end{aligned}$$

which fully defines the system. The density n and magnetization m in the second-order virial expansion may then be determined to the proper order by expanding the quantities

$$n\lambda_T = \frac{\lambda_T}{L}\frac{\partial \ln \mathcal{Z}}{\partial(\beta\mu)} \quad , \quad m\lambda_T = \frac{\lambda_T}{L}\frac{\partial \ln \mathcal{Z}}{\partial(\beta h)} \tag{4.23}$$

in a series to second order. Each of these outputs are then normalized by

$$n_0\lambda_T = \frac{2}{\sqrt{\pi}}\int_{-\infty}^{\infty} dx\, \frac{e^{-x^2}}{1 + ze^{-x^2}} \tag{4.24}$$

to obtain n/n_0 and m/n_0. These calculations are compared with Monte Carlo results in the $z \to 0$ limit, which we do explicitly in Fig. 4.6 and find excellent agreement for small z and βh. However, the quality of the agreement deteriorates quickly as βh is increased unless $z \approx 0$, as expected. For completeness, Fig. 4.7 shows Tan's contact as a function of $\beta\mu$, for several values of βh, and at $\lambda = 1.0$.

4.4.2: Lattice perturbation theory

As an additional verification of the equations of state obtained through an analytic continuation, we performed a next-to-leading order lattice perturbation theory calculation by expanding the lattice grand-

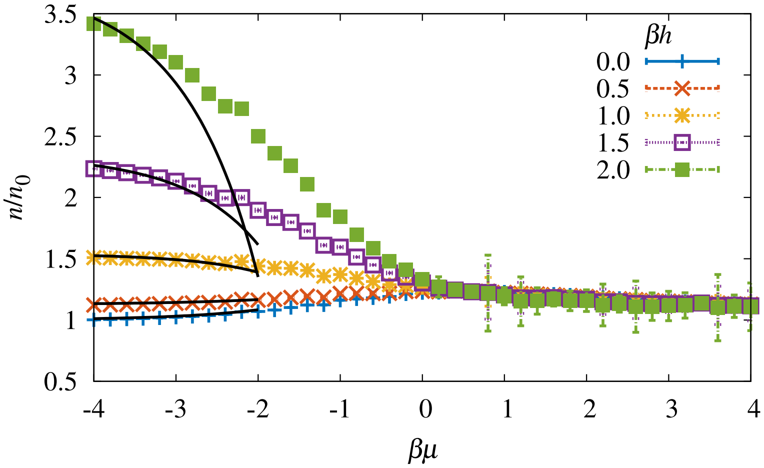

(a) Analytic continuation of the density n as a function of $\beta\mu$ and βh = 0, 0.5, 1.0, 1.5 and 2.0.

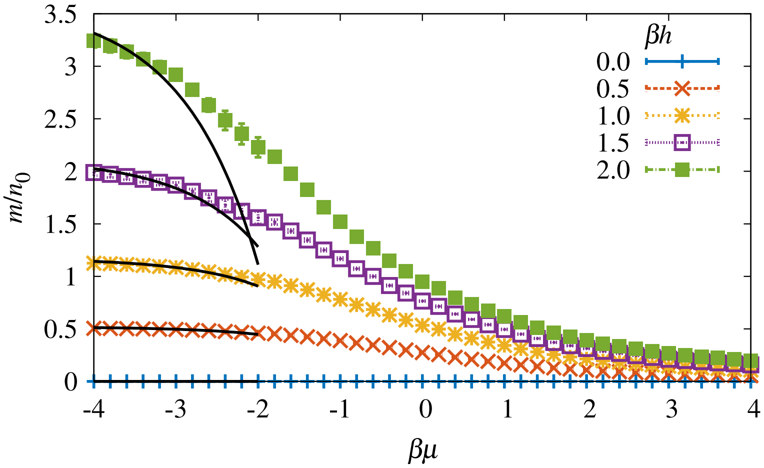

(b) Analytic continuation of the magnetization m as a function of $\beta\mu$ and $\beta h - 0, 0.5, 1.0, 1.5$ and 2.0.

Figure 4.6: Density and magnetization at a dimensionless coupling of $\lambda = 1.0$ in units of the unpolarized, noninteracting density n_0. The solid black lines how the second-order virial expansion for each value of βh. Error bars were estimated by varying the fit parameters by an amount given by the uncertainty in the calculated fits.

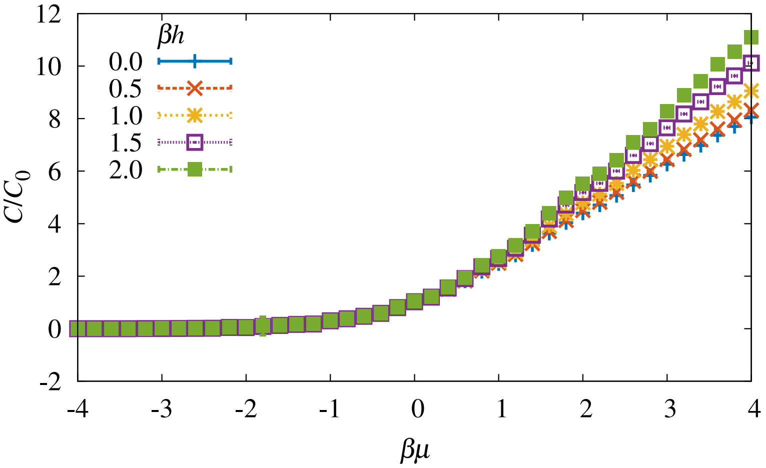

Figure 4.7: *Left:* Tan's contact as a function of the imaginary chemical potential difference βh_{I} at various values of $\beta\mu$ for a dimensionless coupling of $\lambda = 1.0$. C_0 is the contact at $\beta h = \beta\mu = 0$. *Right:* Analytic continuation of the contact as a function of βh at various values of $\beta\mu$. In both plots the contact is an even function about the origin. The curves on the right are color-wise paired by their value of $\beta\mu$, which coincides with the value on the left (by color code, or from top to bottom). Dashed-dotted lines give the results from a fit of the data to the polynomial-type ansatz (4.10), whereas solid lines result from fits of the data to our Padé-type ansatz (4.8) for the fit functions.

canonical partition function $\mathcal{Z}(\beta\mu, \beta h)$ in the dimensionless parameter $A \equiv \sqrt{2(e^{\tau g} - 1)}$ (which arises naturally in lattice calculations, see e.g., Refs. [107–109]) about the non-interacting limit ($A = 0$), up to the second non-vanishing term. Such an expansion on the lattice yields

$$\ln \mathcal{Z} = \ln \mathcal{Z}_0 + \frac{\beta}{2\tau N_x}(Ae^{\beta\mu})^2 \prod_{s=\uparrow,\downarrow} \left(\sum_k \frac{e^{-\beta\epsilon_k}}{1 + z_s e^{-\beta\epsilon_k}} \right), \tag{4.25}$$

where $\mathcal{Z}_0(\beta\mu, \beta h)$ is the partition function of the noninteracting gas, $\epsilon_k = k^2/2m$, and the sum over k is over all possible lattice momenta. The form of this result was derived using a slightly different, and more unwieldy, formalism used for the high-order perturbative expansion shown in Chapter 5. An explicit derivation of this result is shown in the Appendix. The density n/n_0 and magnetization m/n_0 in terms of this NLO result follow from Eq. (4.25) using the definitions of the density n and magnetization m. We display the results of this analytic calculation with the numerical Monte Carlo results and the equations of state of the free gas in Figs. 4.8a and 4.8b. In all cases the results obtained with our proposed analytic continuation approach lie generally between the leading (noninteracting) calculation and the next-to-leading-order result. Later in this thesis, we will see comparisons of polarized gases in one dimension with higher-order perturbation theory beyond NLO, as well as comparisons of this result with complex Langevin.

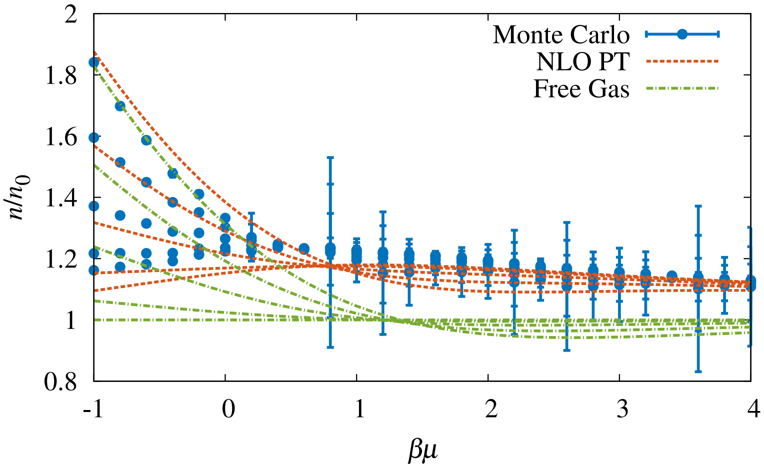

(a) Density as a function of $\beta\mu$ in terms of the non-interacting density.

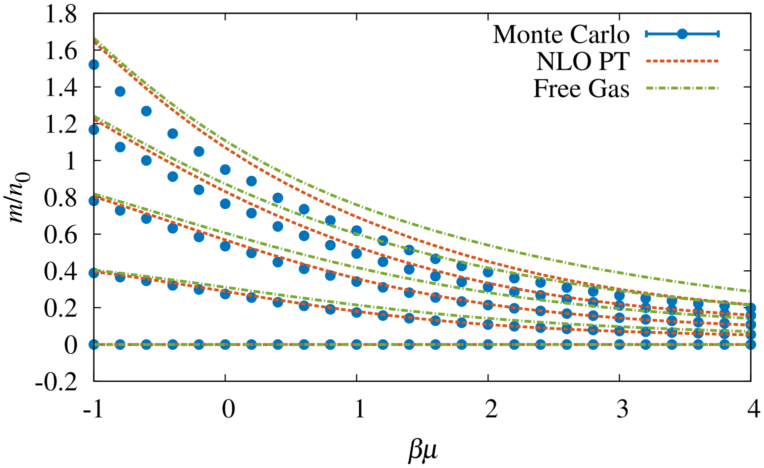

(b) Magnetization as a function of $\beta\mu$ in terms of the non-interacting density.

Figure 4.8: Comparison of the Monte Carlo results after the analytic continuation, a next-to-leading-order perturbation theory calculation, and the free gas for the density and the magnetization. Results are displayed in $\beta h = 0.0, 0.5, 1.0, 1.5$ and 2.0 in the strongly interacting region $\beta\mu > -1$.

CHAPTER 5: High-Order Lattice Perturbation Theory for Interacting Fermions

From previous discussions, it is evident that even though conventional quantum Monte Carlo methods are powerful tools in the sense that they are exact up to controlled systematic and statistical uncertainties, their application is frequently limited to a small subset of systems that are not plagued by the sign problem. Other analytical devices such as the Bethe ansatz (see, e.g., Refs. [110, 111]) can complement such calculations, but are unable to address strong interactions or finite temperature in a controlled manner. As a complement to stochastic methods, we present a novel perturbation theory formalism on the lattice that can be automated (in principle) to arbitrarily high order. Such an expansion takes advantage of the quantum Monte Carlo formalism in that this is an expansion on the lattice where the grand-canonical partition function undergoes a Trotter-Suzuki decomposition and a Hubbard-Stratonovich transformation that allows for a trivial path integral to be computed over an auxiliary field.[1]

Section 5.1: Weak-coupling lattice perturbation theory formalism

In a nutshell, the procedure for analytically calculating the perturbative expansion involves evaluating the diagrammatic expansion and resulting path integral on a computer using an object-oriented approach. The final expressions, which contain sums over the complete frequency-momentum basis, are evaluated numerically to determine the pressure equation of state, or other physical observable.

5.1.1: Path integral form of the grand-canonical partition function

The starting point of our lattice perturbative expansion of the equation of state is the grand-canonical partition function,

$$\mathcal{Z} = \mathrm{Tr}\left[e^{-\beta(\hat{H}-\mu\hat{N})}\right], \tag{5.1}$$

where, as is generally the case, $\hat{H}$ is the Hamiltonian, $\hat{N}$ is the particle number, and $\hat{V}$ is the potential energy operator, which for this work we will generally take to be a two-body operator. Rather than expanding directly in powers of $\hat{V}$, as is conventional in perturbation theory, we will introduce a Hubbard-Stratonovich (HS) transformation. We discretize the imaginary time direction as $\beta = \tau N_\tau$, where τ is an appropriately small number, and apply a third-order Suzuki-Trotter factorization,

---

[1] This chapter is based on the work published in Refs. [112] and [113]. Fig. 5.5 as it appears in Ref. [114] is published by EDP Sciences under the Creative Commons Attribution License 4.0.

$$e^{-\tau \hat{H}} = e^{-\tau \hat{T}/2} e^{-\tau \hat{V}} e^{-\tau \hat{T}/2} + O(\tau^3) \tag{5.2}$$

followed by a HS transformation,

$$e^{-\tau \hat{V}} = \int \mathcal{D}\sigma \, e^{-\tau \hat{W}[\sigma]}, \tag{5.3}$$

where $\hat{W}[\sigma]$ is a one-body operator representing an external potential set by the spacetime auxiliary field σ, and where the path integral is over all possible configurations of that auxiliary field. The specific form of the one-body operator $\hat{W}[\sigma]$ depends on the choice of the HS transformation, as even multiple transformations can be considered for the same interaction. In the case of fermions, this transformation can be either discrete or continuous, and in the latter case it can be compact or noncompact [115]. For the purposes of the perturbative expansion shown here, the particular form of the HS transformation is immaterial, as the transformation is undone order-by-order.

The use of the HS transform is much more common in quantum Monte Carlo approaches than in perturbative ones, and is the natural path to mean-field theory calculations. We will show here, however, that the HS transformation recovers the results of Wick's theorem but bypasses the operator algebra completely. In addition, this approach has the advantage of facilitating the use of many-body forces, as it is relatively simple to write down HS transforms for these systems, and the steps after the transform remain mechanical (which strongly motivates our formalism).

After collecting all the auxiliary field integrals and performing the trace over the resulting product of exponentials of one-body operators, we obtain a path-integral form of the grand-canonical partition function $\mathcal{Z}$,

$$\mathcal{Z} = \int \mathcal{D}\sigma \, \det{}^2 M[\sigma], \tag{5.4}$$

where in the above form, for the sake of demonstration here, we have assumed that the system contains two identical species. This formalism can certainly be extended to a larger number of spin degrees of freedom or polarized systems. The matrix M, which is of dimension $N_\tau \times V$ by $N_\tau \times V$ (where N_τ is the temporal volume and V is the spatial volume), encodes all relevant system dynamics such that

$$M[\sigma] \equiv \begin{pmatrix} 1 & 0 & \cdots & \mathcal{U}_{N_\tau}[\sigma] \\ -\mathcal{U}_1[\sigma] & 1 & \cdots & 0 \\ 0 & -\mathcal{U}_2[\sigma] & \ddots & 0 \\ \vdots & \vdots & \ddots & \vdots \\ 0 & \cdots & -\mathcal{U}_{N_\tau - 1}[\sigma] & 1 \end{pmatrix}. \tag{5.5}$$

For the case of contact interactions, such as in the Gaudin-Yang model, the matrix $\mathcal{U}[\sigma]$ can be written as

$$[\mathcal{U}_t[\sigma]]_{\mathbf{x},\mathbf{x}'} = [e^{-\tau(\mathbf{p}^2/2m-\mu)}]_{\mathbf{x},\mathbf{x}'}[1 + A \sin\sigma(\mathbf{x}', t)] \tag{5.6}$$

where $\mathbf{x}$ and $\mathbf{x}'$ are spatial indices, t is a temporal index, and where $A \equiv \sqrt{2(e^{\tau g} - 1)}$, g is the zero-range coupling, and τ is the temporal lattice spacing (see, e.g., Ref. [1]). We have chosen a realization of the HS transformation in which the continuous field σ takes values between $-\pi$ and π at each point in spacetime, such that the path integral operator is defined as

$$\int \mathcal{D}\sigma \equiv \prod_{\mathbf{x},\tau} \int_{-\pi}^{\pi} \frac{d\sigma(\mathbf{x},\tau)}{2\pi}. \tag{5.7}$$

This particular kind of HS transformation was first explored in Refs. [108, 109].

At this point, we have eliminated from the problem all the quantum operators, which highlights one of the main advantages of the method. Moreover, we have accomplished this by “integrating out” the fermionic degrees of freedom, which is an unorthodox route to perturbation theory. We will see, however, that this is a useful way to proceed in the sense that it mechanically generates the correct answers, and is therefore amenable to automation.

5.1.2: Expanding the fermion determinant

To obtain the perturbative expansion of the grand-canonical partition function on the lattice, we expand the determinant of the matrix M in powers of the dimensionless parameter A defined above, which is related to the bare coupling g that appears in the interaction term of the Hamiltonian. To this end, first note that

$$M = M_0 + A\mathcal{T}\mathcal{S}[\sigma] \tag{5.8}$$

where M_0 is the non-interacting counterpart, and

$$\mathcal{T} \equiv \begin{pmatrix} 0 & 0 & \cdots & T \\ -T & 0 & \cdots & 0 \\ 0 & -T & \ddots & 0 \\ \vdots & \vdots & \ddots & \vdots \\ 0 & \cdots & -T & 0 \end{pmatrix}, \tag{5.9}$$

where $[T]_{\mathbf{x},\mathbf{x}'}$ is the kinetic energy operator (where we have taken units such that $\hbar = k_B = m = 1$), and

$$[\mathcal{S}(\sigma)]_{\mathbf{x},t;\mathbf{x},t} = \delta_{t,t'}\delta_{\mathbf{x},\mathbf{x}'} \sin\sigma(\mathbf{x},t). \tag{5.10}$$

Therefore, we further obtain that $M = M_0(\mathbb{1} + AK\mathcal{S}[\sigma])$, where $K \equiv M_0^{-1}\mathcal{T}$ will play the role of the free propagator, as we explain below, and of course

$$\det M = \det M_0 \det(\mathbb{1} + AK\mathcal{S}[\sigma]). \tag{5.11}$$

At this point, we set aside the non-interacting factor and make use of the identity $\det = \exp \operatorname{Tr} \ln$ to formally expand the logarithm in powers of A, such that

$$\det(\mathbb{1} + AK\mathcal{S}[\sigma]) = \exp\left[\sum_{k=1}^{\infty} A^k E_k\right], \tag{5.12}$$

where we define

$$E_k = \frac{(-1)^{k+1}}{k} \operatorname{Tr}\left[(K\mathcal{S}[\sigma])^k\right]. \tag{5.13}$$

Note that each power of the fermion determinant translates simply as a prefactor in the definition of E_k. Thus, the expansion coefficients for an unpolarized system of N_f species are simply $N_f E_k$. We further write the determinant as

$$\exp\left[\sum_{k=1}^{\infty} A^k E_k\right] = \prod_{k=1}^{\infty} \exp\left[A^k E_k\right] \tag{5.14}$$

$$= \prod_{k=1}^{\infty} \sum_{\{i_k\}=0}^{\infty} \frac{(A^k E_k)^{i_k}}{i_k!}. \tag{5.15}$$

Eq. (5.13) begins to expose the powers of A in the perturbative expansion. The task ahead is to isolate those powers and carry out the path integral exactly. Using these expressions, by fully expanding and combining terms of identical powers of A, it is straightforward to see that

$$\det(\mathbb{1} + AK\mathcal{S}[\sigma]) = 1 + AE_1 + A^2\left(\frac{E_1^2}{2!} + E_2\right) + A^3\left(\frac{E_1^3}{3!} + E_1E_2 + E_3\right) + \cdots . \tag{5.16}$$

The above expansion corresponds to one of the spin degrees of freedom and therefore it is to be combined with a corresponding expansion for the other spin, which could be done for polarized (different μ for each species) or unpolarized (same μ) cases. For the moment, we focus on the latter with a two-component system, which simply means that we are expanding the square of the determinant. As mentioned above, this can be accomplished easily by setting $E_k \to N_f E_k$ for the general case of N_f flavors.

5.1.3: Recovering Wick's theorem by calculating the path integral exactly at each order

Once the determinants are expanded to the desired power of A, which is easy to automate, one obtains products of powers of the various E_k defined in Eq. (5.13). The path integral of each of these products must be evaluated to obtain the expansion of the partition function. For instance, at second order, one of the terms is

$$\int \mathcal{D}\sigma E_2[\sigma] = -\frac{1}{2}\int \mathcal{D}\sigma \ \mathrm{Tr}\left[(K\mathcal{S}[\sigma])^2\right]$$

$$= -\frac{1}{2}K_{ij}K_{km}\int \mathcal{D}\sigma \ \mathcal{S}[\sigma]_{jk}\mathcal{S}[\sigma]_{mi}, \tag{5.17}$$

where all the (collective, spacetime) indices i, j, k, m on the right-hand side are assumed to be summed over.

Writing out the indices explicitly at each order, we see that the main problem is computing path integrals of the form

$$I_m(b_1, b_2, \ldots, b_m) = \int \mathcal{D}\sigma \sin(\sigma[b_1])\sin(\sigma[b_2])\ldots\sin(\sigma[b_m]),$$

where each b_k represents a spacetime coordinate. These integrals vanish if m is odd, but otherwise the result is generally finite and positive. For instance, for $m = 2$,

$$I_2(b_1, b_2) \quad = \quad \frac{1}{2}\delta_{b_1,b_2}, \tag{5.18}$$

and for $m = 4$,

$$\begin{aligned} I_4(b_1, b_2, b_3, b_4) \quad = \quad & \frac{3}{8}\,\delta_{b_1,b_2}\,\delta_{b_1,b_3}\,\delta_{b_1,b_4} + \frac{1}{4}\left[\delta_{b_1,b_2}\,\delta_{b_3,b_4}(1 - \delta_{b_2,b_3})\right. \\ & \left. + \,\delta_{b_1,b_3}\,\delta_{b_2,b_4}(1 - \delta_{b_3,b_2}) + \delta_{b_1,b_4}\,\delta_{b_2,b_3}(1 - \delta_{b_4,b_2})\right], \end{aligned} \tag{5.19}$$

where $3/8$ is the result for the case of all four coordinates coinciding, i.e.

$$\int_{-\pi}^{\pi} \frac{d\sigma}{2\pi} \sin^4 \sigma = \frac{3}{8}. \tag{5.20}$$

It is the tensor expressions like Eq. (5.19) that automatically implement Wick's theorem when contracting with the various K propagators. As with the Taylor expansion of the determinant, the calculation of the I_m needed for each of the terms at a given order was also automated, as was the subsequent index contraction with the propagators. The result of that process is that not only the diagrams themselves, but also all the symmetry factors are generated automatically, minimizing the amount of manual bookkeeping. Naturally, the topology of the diagrams enters through the I_m tensors, which encode the multiple ways in which the corresponding path integral can give a non-vanishing result.

The complexity of the expression for I_m grows with each order in the perturbative expansion and causes the number of terms in the expansion of $\mathcal{Z}$ (i.e. after contracting with the K's) to grow very quickly. Although the next-to-leading (NLO) contribution can easily be verified by hand, the next-to-next-to-next-to-leading (N3LO) (i.e. A^6) order produces (naively) on the order of 10^3 terms, all of which must be simplified to obtain the final results. Moreover, in the case of polarized systems, multiple products of the determinant must be expanded. This scaling underscores why the method we proposed here is well suited for automation, but it is otherwise not ideal for manual calculation, especially if a high-order, finite-temperature expansion is the goal.

5.1.4: Transforming to frequency-momentum space on the lattice

Naturally, the matrix K can be diagonalized in the momentum basis with a discrete Fourier transform, such that

$$[K]_{ab} = \sum_{q} U^{\dagger}_{aq}[D_0]_q U_{qb} \tag{5.21}$$

where a, b are collective spacetime indices of the form (t, x), and $q = (\omega, k)$ is a collective frequency-momentum index, with $\omega = (2n_\omega + 1)/N_\tau$ being a fermionic Matsubara frequency ($n_\omega = 1, \ldots, N_\tau$), and $\mathbf{k} = 2\mathbf{n}_\mathbf{k}\pi/N_x$ ($\mathbf{n}_{\mathbf{k},i} = 1, \ldots, N_x$) a d-dimensional spatial wavevector. The free propagator D_0 is then

$$[D_0]_q \equiv \frac{1}{1 - \exp[i\omega + \tau(\mathbf{k}^2/2 - \mu)]}, \tag{5.22}$$

while the Fourier transform matrices take the form

$$U_{aq} = \frac{1}{\sqrt{N_x^d N_\tau}} \exp[i(\omega t - \mathbf{k} \cdot \mathbf{x})]. \tag{5.23}$$

By computing the path integral over the auxiliary field σ for all the terms in the expansion of the determinant at a particular order, we are left with an object of the generic schematic form

$$S = \sum [K]_{a_1 a_2}[K]_{a_3 a_4} \ldots [K]_{a_{2m-1} a_{2m}} I_{a_1 \ldots a_{2m}} \tag{5.24}$$

where the sum is taken over all free spacetime indices, and the object $I_{a_1 \ldots a_{2m}}$ results from the path integral over the interaction terms $\sin(\sigma_i)$.

Upon inserting the Fourier representation of the propagator [c.f. Eq. (5.21)], we obtain a form that is described by a collection of indices in the frequency-momentum basis:

$$S = \sum [D_0]_{q_1}[D_0]_{q_2} \ldots [D_0]_{q_m} \tilde{I}_{q_1, \ldots, q_m} \tag{5.25}$$

where $\tilde{I}_{q_1, \ldots, q_m}$ results from appropriately contracting the various Fourier tensors U and $U^\dagger$ with $I_{a_1 \ldots a_{2m}}$. The $\tilde{I}$ tensors represent momentum conservation laws for each specific term.

The advantage of going to frequency-momentum space is that S can be obtained by performing m

frequency-momentum sums instead of the $2m$ spacetime sums. This optimization, however, is not enough; it is crucial to carry out the frequency sums analytically in order to have a numerically manageable expression at the end. We turn to those sums next.

5.1.5: Computing finite Matsubara frequency sums analytically: two tricks

In the evaluation of expressions at a given order n, we are faced with nested frequency sums that schematically look like the expression

$$\sum_{q_1,q_2,\ldots,q_m} [D_0]_{q_1}[D_0]_{q_2}\ldots[D_0]_{q_m}\delta(\{q_k\}), \tag{5.26}$$

where we have left out sums over momenta, which are to be carried out afterwards, and the delta factor represents an energy-momentum conservation law that is derived from each diagram's topology. Note that, here and below, we will use the delta notation to represent the discrete Kronecker symbol rather than the Dirac symbol (we have no need for Dirac deltas here, as all our expressions are discrete). In this section, we show how we performed the frequency sums in a way that does not use complex contour integration and, moreover, allows us to treat all the sums simultaneously.

We begin with an example. The simplest case is that of a single factor, which may seem trivial but is nevertheless instructive:

$$S_1 = \sum_{n=1}^{N_\tau}[D_0]_n = \sum_{n=1}^{N_\tau}\frac{1}{1-Q\exp(i\omega_n)}, \tag{5.27}$$

where we have encoded all the momentum and chemical potential dependence in the factor Q, and where $\omega_n = (2n+1)\pi/N_\tau$. In this case we expand the expression inside the sum as a geometric series:

$$\begin{aligned} S_1 &= \sum_{n=1}^{N_\tau}\sum_{k=0}^{\infty} Q^k e^{i\omega_n k} = \sum_{k=0}^{\infty} Q^k \sum_{n=1}^{N_\tau} e^{i\omega_n k} && (5.28)\\ &= \sum_{m=0}^{\infty}\sum_{k=0}^{\infty} Q^k \delta(k-mN_\tau)(-1)^m && (5.29)\\ &= \sum_{m=0}^{\infty} Q^{mN_\tau}(-1)^m = \frac{N_\tau}{1+Q^{N_\tau}}, && (5.30)\end{aligned}$$

where we used the fact that $k \geq 0$ and

$$\sum_{n=1}^{N_\tau} e^{i2\pi nk/N_\tau} = N_\tau \sum_{m=-\infty}^{\infty} \delta(k - mN_\tau). \tag{5.31}$$

The S_1 sum is useful per se, but also because high-order calculations need the more general sums, such as

$$S_1^{(k)} = \sum_{n=1}^{N_\tau} \left(\frac{1}{1 - Q \exp(i\omega_n)} \right)^{k+1}, \tag{5.32}$$

such that $S_1^{(0)} = S_1$. For general k, this is easy to compute by introducing a new parameter λ via

$$S_1(\lambda) \equiv \sum_{n=1}^{N_\tau} \frac{1}{\lambda - Q \exp(i\omega_n)} = \frac{1}{\lambda} \frac{N_\tau}{1 + (Q/\lambda)^{N_\tau}}, \tag{5.33}$$

and differentiate with respect to λ as needed,

$$S_1^{(k)} = \frac{(-1)^k}{k!} \left. \frac{d^k S_1(\lambda)}{d\lambda^k} \right|_{\lambda=1}. \tag{5.34}$$

Clearly, $S_1(\lambda)$ is a generating function for frequency sums of higher order. In particular, for instance,

$$S_1^{(1)} = \frac{[1 - Q^{N_\tau}(N_\tau - 1)]N_\tau}{(1 + Q^{N_\tau})^2}. \tag{5.35}$$

The method of expanding the numerator as a power series applies as well when multiple sums are present, such as for higher-order diagrams for which the corresponding frequency sums are listed in Sec. 5.3.

The general procedure of the method is as follows. First, take a step backward and use the Fourier-sum representation of all the frequency Kronecker deltas, i.e.

$$\delta[f(\omega_1, \omega_2, \ldots)] = \frac{1}{N_\tau} \sum_{p=0}^{N_\tau - 1} e^{ipf(\omega_1, \omega_2, \ldots)}, \tag{5.36}$$

in combination with the geometric series expression of the denominators. This first step is similar to that of techniques used in the continuum, where an integral representation of a Dirac delta function is utilized. Beyond this point, however, the calculations differ considerably.

The second step is to sum over each fermionic frequency ω_n, which yields as many delta functions as denominators, with their corresponding "boundary" sums and factors of $(-1)^m$, i.e. use

$$\sum_{n=1}^{N_\tau} e^{i\omega_n y} = N_\tau \sum_{m=-\infty}^{\infty} \delta(y - mN_\tau)(-1)^m. \tag{5.37}$$

Here it is important to keep the terms for all m, as y will generally vary over a semi-infinite range due to the geometric series expansion.

Third, sum over the geometric sum index to saturate the delta functions generated in the previous step. To this end, it is useful to extend the geometric sum index to $-\infty$, such that Heaviside step functions should be inserted accordingly.

Fourth, implement the constraints over the boundary sums and evaluate such sums, which lead to the expected $(1 + Q_k^{N_\tau})^{-1}$ factors. Finally, sum over the Fourier index of the energy-conserving delta functions. As is clear from the above, the operations to be performed are rather elementary and do not involve complex analysis, only a small amount of bookkeeping. It is the order of the operations that is crucial for the simplicity of the method.

Section 5.2: Perturbative results for the equation of state

In this section we show the results of implementing the lattice perturbation theory formalism first to the case of unpolarized, spin-1/2 fermions in one spatial dimension, and then address the spin-polarized case. The specific Hamiltonian we explore is the Gaudin-Yang form [12, 13], where $\hat{H} = \hat{T} + \hat{V}$ with the kinetic energy operator

$$\hat{T} = \int dx \sum_{s=\uparrow,\downarrow} \hat{\psi}_s^\dagger(x) \left(-\frac{\hbar^2}{2m}\frac{d^2}{dx^2}\right) \hat{\psi}_s(x), \tag{5.38}$$

and the potential energy operator

$$\hat{V} = -g \int dx\, \hat{n}_\uparrow(x)\hat{n}_\downarrow(x), \tag{5.39}$$

where $\hat{\psi}_s^\dagger(x)$ and $\hat{\psi}_s(x)$ are the creation and annihilation operators in coordinate space for particles of spin s, and $\hat{n}_s = \hat{\psi}_s^\dagger(x)\hat{\psi}_s(x)$ are the corresponding density operators. As usual, there are only two dimensionless parameters characterizing this one-dimensional problem at finite temperature: the fugacity $z = e^{\beta\mu}$ and the interaction coupling $\lambda = \sqrt{\beta}g$.

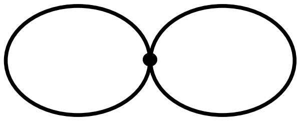

Figure 5.1: Feynman diagram for the next-to-leading order (NLO) contribution to the grand canonical partition function.

5.2.1: Analytic expressions for the perturbative expansion

Among the main results of this formalism are the final expressions for the perturbative contributions to the partition function $\mathcal{Z}$ at each order n up to N4LO, which are shown in Tables 5.1, 5.2, and 5.3 (explained in further detail below). Each term at order n is to be accompanied by a factor of A^{2n}, but all the information required to reproduce the numerical results shown are presented in tables and the provided expressions for the relevant frequency sums within this chapter. Note however, that the numerical evaluation of these expressions has only been carried out to N3LO; the limiting factor here is the analytic evaluation of fourth-order frequency sums.

Each contribution to the perturbative expansion of the partition function corresponds to a fully connected Feynman diagram of n vertices (or a product of two or more such diagrams), and can be described by the product of some scalar prefactor with a $1/(N_x N_\tau)^n$ dependence, and one or more sums over the complete momentum-frequency basis. The Feynman diagrams that appear at NLO, N2LO, N3LO, and N4LO are provided in Figs. 5.1, 5.2, 5.3, and 5.4, respectively. The Matsubara-frequency sums in the analytic expressions provided have already been carried out using the technique outlined in Sec. 5.1.5; therefore, all sums and indices that remain in these expressions are over spatial momenta. The frequency sums always contain Q_n as parameters that encode the spatial momentum dependence:

$$Q_n \equiv e^{\tau(\mathbf{k}_n^2/2-\mu)}. \tag{5.40}$$

A variety of frequency sums over various products of propagators and momentum conservation conditions appear in these expressions. The expressions for S_1 and $S_1^{(1)}$ are given earlier in the text by Eqs. (5.30) and (5.35), respectively. The remainder of the frequency sums are provided for reference in Sec. 5.3.

The number of loops, or the number of nested momentum sums that appear for each expression, is also provided explicitly in the tables of perturbative contributions. Since the momentum sums are generally computed in full, this number provides an estimate for the computational scaling that is required to compute the value of each diagram; the number of terms that must be computed scales as $N_x^{\ell d}$, where ℓ is the number

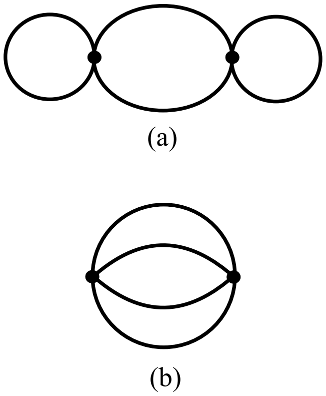

Figure 5.2: Feynman diagrams for the next-to-next-to-leading order (N2LO) contribution to the grand canonical partition function.

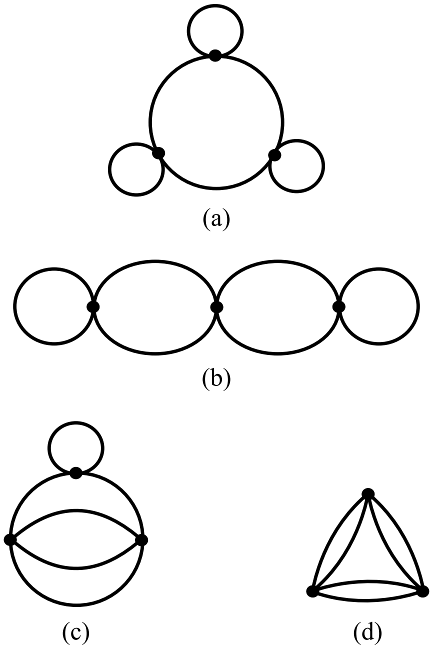

Figure 5.3: Feynman diagrams for the next-to-next-to-next-to leading order (N3LO) contribution to the grand canonical partition function.

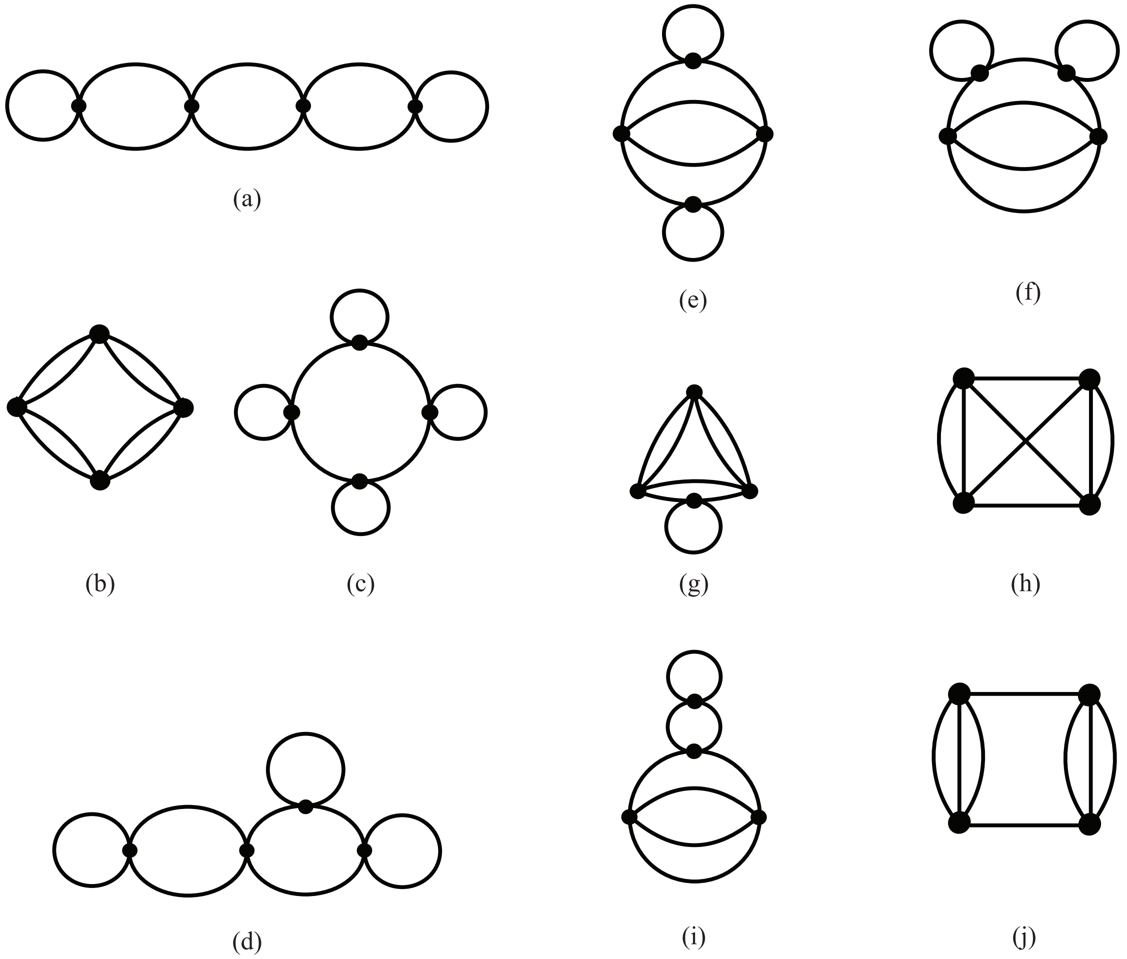
(a) (b) (c) (d) (e) (f) (g) (h) (i) (j)

Figure 5.4: Feynman diagrams for the next-to-next-to-next-to-next-to leading order (N4LO) contribution to the grand canonical partition function.

of loops and d is the spatial dimension. Notice that although the expansion is formally in powers of the parameter A^2, one may regard this procedure directly as a weak-coupling expansion in g, given $A^2 \sim \tau g$ for $\tau g \ll 1$. As such, one may qualitatively think of the representation of $\ln \mathcal{Z}$ in this expansion as it appears in Fig. 5.5.

5.2.2: Pressure equation of state via perturbation theory

To determine the pressure P of a system of any dimension, we use the perturbative expansion of the interacting partition function $\mathcal{Z}$, which we expand to order $2n$ in the parameter A and write as

$$\mathcal{Z} = e^{\beta PV} = \mathcal{Z}_0(1 + A^2\Delta_1 + A^4\Delta_2 + A^6\Delta_3 + A^8\Delta_4 + \cdots) \tag{5.41}$$

Table 5.1: Detail of next-to-leading order (NLO), next-to-next-to-leading order (N2LO), and next-to-next-to-next-to-leading order (N3LO) contributions (respectively, order A^2, A^4, and A^6) to the grand-canonical partition function $\mathcal{Z}$. The indicated diagram figure refers to the corresponding fully-connected Feynman diagram or product of such diagrams for each contribution. The volume $V = N_x N_\tau$ that appears in all expressions refers to the spacetime volume of the lattice. The greatest number of loops that appear for each fully-connected diagram is also provided. It is implicit in the notation that a momentum-conserving Kronecker delta has been utilized to eliminate momentum sums: one in the case of S_4 and $S_4^{(1)}$, but two in the case of S_6.

Order	Diagram Figure	Prefactor	Diagram Frequency Sum	Loops
NLO	Fig. 5.1	$1/(2\,V)$	$\left[\sum_{\mathbf{p}_1} S_1(Q_1)\right]^2$	1-loop
N2LO	[Fig. 5.1]^2	$1/(8\,V^2)$	$\left[\sum_{\mathbf{p}_1} S_1(Q_1)\right]^4$	1-loop
N2LO	Fig. 5.2(a)	$-1/(4\,V^2)$	$\left[\sum_{\mathbf{p}_1} S_1^{(1)}(Q_1)\right]\left[\sum_{\mathbf{p}_1} S_1(Q_1)\right]^2$	1-loop
N2LO	Fig. 5.2(b)	$1/(8\,V^2)$	$\sum_{\mathbf{p}_1,\mathbf{p}_2,\mathbf{p}_3} S_4(Q_1, Q_2, Q_3)$	3-loop
N3LO	[Fig. 5.1]^3	$1/(48\,V^3)$	$\left[\sum_{\mathbf{p}_1} S_1(Q_1)\right]^6$	1-loop
N3LO	Fig. 5.2(a) × Fig. 5.1	$-1/(8\,V^3)$	$\left[\sum_{\mathbf{p}_1} S_1^{(1)}(Q_1)\right]\left[\sum_{\mathbf{p}_1} S_1(Q_1)\right]^4$	1-loop
N3LO	Fig. 5.2(b) × Fig. 5.1	$1/(16\,V^3)$	$\left[\sum_{\mathbf{p}_1,\mathbf{p}_2,\mathbf{p}_3} S_4(Q_1, Q_2, Q_3)\right]\left[\sum_{\mathbf{p}_1} S_1(Q_1)\right]^2$	3-loop
N3LO	Fig. 5.3(a)	$1/(12\,V^3)$	$\left[\sum_{\mathbf{p}_1} S_1^{(2)}(Q_1)\right]\left[\sum_{\mathbf{p}_1} S_1(Q_1)\right]^3$	1-loop
N3LO	Fig. 5.3(b)	$1/(8\,V^3)$	$\left[\sum_{\mathbf{p}_1} S_1^{(1)}(Q_1)\right]^2\left[\sum_{\mathbf{p}_1} S_1(Q_1)\right]^2$	1-loop
N3LO	Fig. 5.3(c)	$-1/(4\,V^3)$	$\left[\sum_{\mathbf{p}_1,\mathbf{p}_2,\mathbf{p}_3} S_4^{(1)}(Q_1, Q_2, Q_3)\right]\left[\sum_{\mathbf{p}_1} S_1(Q_1)\right]$	3-loop
N3LO	Fig. 5.3(d)	$1/(12\,V^3)$	$\sum_{\mathbf{p}_1,\mathbf{p}_2,\mathbf{p}_3,\mathbf{p}_4} S_6(Q_1, Q_2, Q_3, Q_4)$	4-loop

Table 5.2: Part I detail of next-to-next-to-next-to-next-to (N4LO) contribution (order A^8) to the grand-canonical partition function $\mathcal{Z}$. The remainder of the N4LO contributions are provided in Table 5.3. All diagrams that appear in this table are disconnected diagrams, and will cancel after the logarithm of the partition function is taken. The indicated diagram figure refers to the corresponding fully-connected Feynman diagram or product of such diagrams for each contribution. The volume $V = N_x N_\tau$ that appears in all expressions refers to the spacetime volume of the lattice. The greatest number of loops that appear for each fully-connected diagram is also provided. It is implicit in the notation that a momentum-conserving Kronecker delta has been utilized to eliminate momentum sums.

Diagram Figure	Prefactor	Diagram Frequency Sum	Loops
[Fig. 5.1]^4	$1/(384\,V^4)$	$\left[\sum_{\mathbf{p}_1} S_1(Q_1)\right]^8$	1-loop
[Fig. 5.2(a)] × [Fig. 5.1]^3	$-1/(32\,V^4)$	$\left[\sum_{\mathbf{p}_1} S_1^{(1)}(Q_1)\right]\left[\sum_{\mathbf{p}_2} S_1(Q_2)\right]^6$	1-loop
[Fig. 5.2(b)] × [Fig. 5.1]^2	$1/(64\,V^4)$	$\left[\sum_{\mathbf{p}_1,\mathbf{p}_2,\mathbf{p}_3} S_4(Q_1,Q_2,Q_3)\right]\left[\sum_{\mathbf{p}_1} S_1(Q_1)\right]^4$	1-loop
[Fig. 5.3(a)] × [Fig. 5.1]^5	$1/(24\,V^4)$	$\left[\sum_{\mathbf{p}_1} S_1^{(2)}(Q_1)\right]\left[\sum_{\mathbf{p}_1} S_1(Q_1)\right]^5$	3-loop
[Fig. 5.3(b)] × [Fig. 5.1]^2	$1/(16\,V^4)$	$\left[\sum_{\mathbf{p}_1} S_1^{(1)}(Q_1)\right]^2\left[\sum_{\mathbf{p}_1} S_1(Q_1)\right]^4$	1-loop
[Fig. 5.3(c)] × [Fig. 5.1]^3	$-1/(8\,V^4)$	$\left[\sum_{\mathbf{p}_1,\mathbf{p}_2,\mathbf{p}_3} S_4^{(1)}(Q_1,Q_2,Q_3)\right]\left[\sum_{\mathbf{p}_1} S_1(Q_1)\right]^3$	3-loop
[Fig. 5.3(d)] × [Fig. 5.1]^2	$1/(24\,V^4)$	$\left[\sum_{\mathbf{p}_1,\mathbf{p}_2,\mathbf{p}_3,\mathbf{p}_4} S_6(Q_1,Q_2,Q_3,Q_4)\right]\left[\sum_{\mathbf{p}_1} S_1(Q_1)\right]^2$	4-loop
[Fig. 5.2(b)]^2	$1/(32\,V^4)$	$\left(\left[\sum_{\mathbf{p}_1} S_1^{(1)}(Q_1)\right]\left[\sum_{\mathbf{p}_1} S_1(Q_1)\right]^2\right)^2$	1-loop
[Fig. 5.2(c)]^2	$1/(128\,V^4)$	$\left[\sum_{\mathbf{p}_1,\mathbf{p}_2,\mathbf{p}_3} S_4^{(1)}(Q_1,Q_2,Q_3)\right]^2$	3-loop
[Fig. 5.2(b)] × [Fig. 5.2(c)]	$-1/(32\,V^4)$	$\left[\sum_{\mathbf{p}_1} S_1^{(1)}\right]\left[\sum_{\mathbf{p}_1,\mathbf{p}_2,\mathbf{p}_3} S_4^{(1)}\right]\left[\sum_{\mathbf{p}_1} S_1\right]^2$	3-loop

Table 5.3: Part II detail of the next-to-next-to-next-to-next-to (N4LO) contribution (order A^8) to the grand-canonical partition function $\mathcal{Z}$. The first part of the N4LO contributions are provided in Table 5.2. All diagrams that appear in this table are new fully-connected diagrams that appear at this order. The indicated diagram figure refers to the corresponding fully-connected Feynman diagram or product of such diagrams for each contribution. The volume $V = N_x N_\tau$ that appears in all expressions refers to the spacetime volume of the lattice. The greatest number of loops that appear for each fully-connected diagram is also provided. It is implicit in the notation that a momentum-conserving Kronecker delta has been utilized to eliminate momentum sums.

Diagram Figure	Prefactor	Diagram Frequency Sum	Loops
Fig. 5.4(a)	$-1/(16\,V^4)$	$\left[\sum_{\mathbf{p}_1} S_1^{(1)}(Q_1)\right]^3 \left[\sum_{\mathbf{p}_1} S_1(Q_1)\right]^2$	1-loop
Fig. 5.4(b)	$-1/(16\,V^4)$	$\left[\sum_{\mathbf{p}_1,\mathbf{p}_2,\mathbf{p}_3,\mathbf{p}_4,\mathbf{p}_5} S_{8\alpha}(Q_1,Q_2,Q_3,Q_4,Q_5)\right]$	5-loop
Fig. 5.4(c)	$-1/(32\,V^4)$	$\left[\sum_{\mathbf{p}_1} S_1^{(3)}(Q_1)\right]\left[\sum_{\mathbf{p}_1} S_1(Q_1)\right]$	1-loop
Fig. 5.4(d)	$-1/(8\,V^4)$	$\left[\sum_{\mathbf{p}_1} S_1^{(2)}\right]\left[\sum_{\mathbf{p}_1} S_1^{(1)}\right]\left[\sum_{\mathbf{p}_1} S_1\right]^3$	1-loop
Fig. 5.4(e)	$3/(16\,V^4)$	$\left[\sum_{\mathbf{p}_1,\mathbf{p}_2,\mathbf{p}_3} S_4^{(2)}(Q_1,Q_2,Q_3)\right]\left[\sum_{\mathbf{p}_1} S_1(Q_1)\right]$	3-loop
Fig. 5.4(f)	$1/(8\,V^4)$	$\left[\sum_{\mathbf{p}_1,\mathbf{p}_2,\mathbf{p}_3} S_4^{(3)}(Q_1,Q_2,Q_3)\right]\left[\sum_{\mathbf{p}_1} S_1(Q_1)\right]$	3-loop
Fig. 5.4(g)	$-1/(4\,V^4)$	$\left[\sum_{\mathbf{p}_1} S_1\right]\left[\sum_{\mathbf{p}_1,\mathbf{p}_2,\mathbf{p}_3,\mathbf{p}_4,\mathbf{p}_5} S_6^{(1)}\right]$	5-loop
Fig. 5.4(h)	$1/(32\,V^4)$	$\left[\sum_{\mathbf{p}_1,\mathbf{p}_2,\mathbf{p}_3,\mathbf{p}_4,\mathbf{p}_5} S_{8\beta}(Q_1,Q_2,Q_3,Q_4,Q_5)\right]$	5-loop
Fig. 5.4(i)	$1/(8\,V^4)$	$\left[\sum_{\mathbf{p}_1} S_1^{(1)}\right]^2 \left[\sum_{,\mathbf{p}_2,\mathbf{p}_3} S_4^{(1)}\right]\left[\sum_{\mathbf{p}_1} S_1\right]$	3-loop
Fig. 5.4(j)	$-1/(16\,V^4)$	$\sum_{\mathbf{p}_1,\mathbf{p}_2,\mathbf{p}_3,\mathbf{p}_4,\mathbf{p}_5} S_7^{(1)}(Q_1,Q_2,Q_3,Q_4,Q_5)$	5-loop

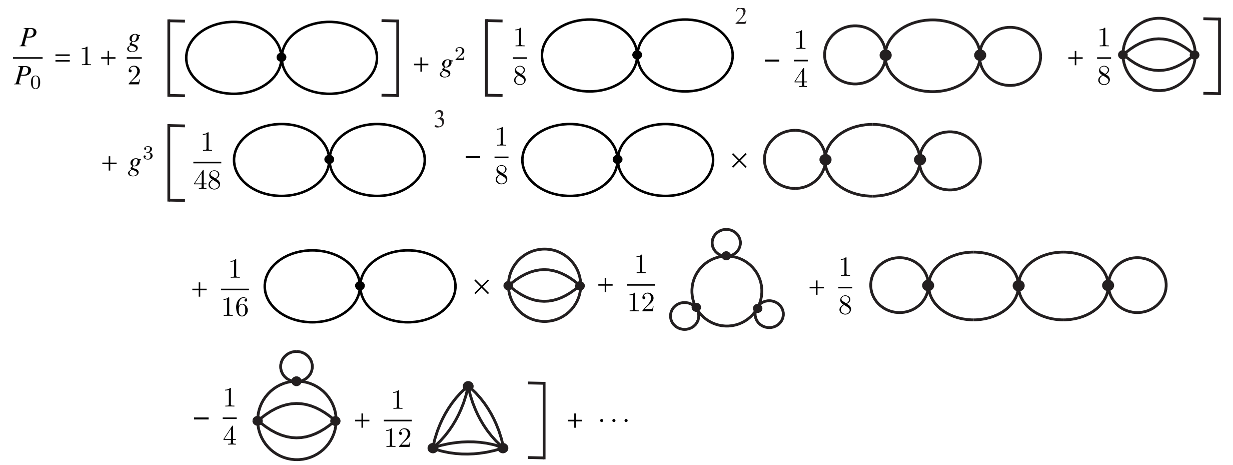

Figure 5.5: The perturbative expansion for the grand-canonical partition function as $\ln \mathcal{Z} = P/P_0$ written explicitly up to N3LO, where we consider the weak coupling limit $A^2 \sim \tau g$. In this respect, one may qualitatively regard the expansion as expanding in g directly on the lattice.

where Δ_n is the NnLO contribution, as given by the expressions in Tables 5.1, 5.2, and 5.3, and where $\mathcal{Z}_0$ is the non-interacting grand-canonical partition function, e.g. for an unpolarized system in one spatial dimension,

$$\ln \mathcal{Z}_0 = \beta P_0 V = \sum_{k=-N_x/2}^{N_x/2-1} \ln(1 + z e^{-\beta \epsilon_k}) \tag{5.42}$$

with $\epsilon_k = (2\pi k/N_x)^2/2$. Therefore, the interacting pressure P, relative to the non-interacting result P_0, becomes

$$\frac{P}{P_0} = 1 + \frac{\ln(1 + A^2\Delta_1 + A^4\Delta_2 + A^6\Delta_3 + A^8\Delta_4 + \cdots)}{\ln \mathcal{Z}_0}. \tag{5.43}$$

To keep the computed value of $\ln \mathcal{Z}$ consistent with the highest order of A in the expansion of $\mathcal{Z}$, we expand the numerator $\ln(1 + \sum_n A^{2n}\Delta_n)$ in a Taylor series about $A = 0$, such that the expanded form up to N4LO is

$$\frac{P}{P_0} = 1 + \frac{1}{\ln \mathcal{Z}_0}(A^2\zeta_1 + A^4\zeta_2 + A^6\zeta_3 + A^8\zeta_4) \tag{5.44}$$

where we define

$$\begin{aligned}
\zeta_1 &= \Delta_1, && (5.45)\\
\zeta_2 &= \Delta_2 - \frac{1}{2}\Delta_1^2, && (5.46)\\
\zeta_3 &= \Delta_3 - \Delta_1\Delta_2 + \frac{1}{3}\Delta_1^3, && (5.47)\\
\zeta_4 &= \Delta_4 - \Delta_1\Delta_3 - \frac{1}{2}\Delta_2^2 + \Delta_1^2\Delta_2 - \frac{1}{4}\Delta_1^4. && (5.48)
\end{aligned}$$

Note that while this procedure offers consistency in the order of the coupling at all stages of the calculation, in performing this expansion it is important to be mindful of the validity of choosing to expand about the non-interacting limit. Since the partition function is an extensive quantity, this expansion may yield unphysical results in cases where $\sum_n A^{2n}\Delta_n \gg 1$, which may occur in cases where stronger effective interactions are present, as is the case when $N_f > 2$. However, in all cases shown here, the observables demonstrate physical behavior and are in agreement with alternative methods where available.

5.2.3: Pressure and density equations of state for the unpolarized one-dimensional system

Using Eq. (5.44), we computed the pressure equation of state at NLO, N2LO, and N3LO as a function of the dimensionless parameter $\beta\mu = \ln z$. Our results for this quantity, for the case of attractive interactions, are shown for a variety of interaction strengths in Fig. 5.6 (top). Remarkably, we see evidence of convergence for $\beta\mu \geq 2$, even for a coupling of $\lambda = 2$. For $\beta\mu \leq 2$, on the other hand, our results are qualitatively correct but fail to match the hybrid Monte Carlo answers by roughly 10% in the worst case of $\lambda = 2$.

A possible explanation of this behavior is that perturbation theory simply fails to capture the effect of the two-body bound state in the virial coefficients as λ is increased, which in the case of the second-order coefficient b_2 involves a dominant inverse gaussian contribution $\propto \exp(\lambda^2/4)$. One could choose to absorb this effect into the definition of λ by way of a new renormalization scheme defined by matching to an exact (lattice or continuum) calculation of b_2, instead of identifying the coupling g with the inverse scattering length. Of course, such a renormalization scheme would improve the agreement with the Monte Carlo results in the semiclassical regime of negative $\beta\mu$, but by the same token it would spoil it for $\beta\mu \geq 2$. Nevertheless, as the perturbative expansion is extended to higher order, the convergence properties of the regime is expected to improve.

In all cases, the NLO results are quantitatively disappointing, but N2LO and N3LO display substantial improvement both in convergence and in approaching the Monte Carlo results. Naturally, this improvement

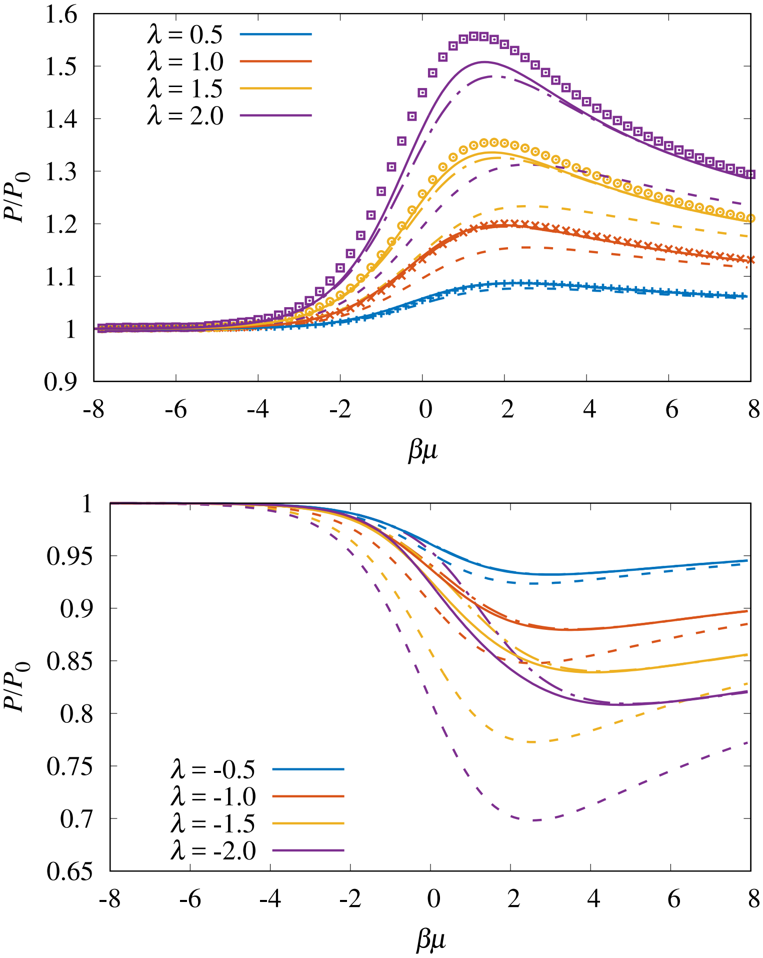

Figure 5.6: Pressure P of the attractive (top) and repulsive (bottom) unpolarized Fermi gas in units of the pressure of the noninteracting system P_0, as shown for the dimensionless interaction strengths $\lambda = 0.5$, 1.0, 1.5, 2.0, and $\lambda = -0.5$, -1.0, -1.5, -2.0 for the attractive and repulsive cases, respectively. The NLO (dashed line), N2LO (dash-dotted line), and N3LO (solid line) results from perturbation theory are displayed for each coupling. The corresponding data points for each attractive coupling are computed using HMC (see Ref. [1]).

is not free: the computational effort increases dramatically for N2LO and N3LO relative to NLO. Similar behavior is seen for the repulsive case in Fig. 5.6 (bottom) but with an important difference, where the results oscillate as the perturbative order is increased, whereas in the attractive case convergence appears to be monotonic.

Based on our knowledge of the pressure, differentiation with respect to $\beta\mu$ gives access to the density of the system, for which results from perturbation theory can be compared more directly with quantum Monte Carlo results (the pressure is not typically a quantity computed directly in Monte Carlo calculations, but is rather obtained by integrating the density; see Ref. [1] for details). We show a comparison in Fig. 5.7 (top) for the case of attractive interactions where Monte Carlo calculations are possible without a sign problem.

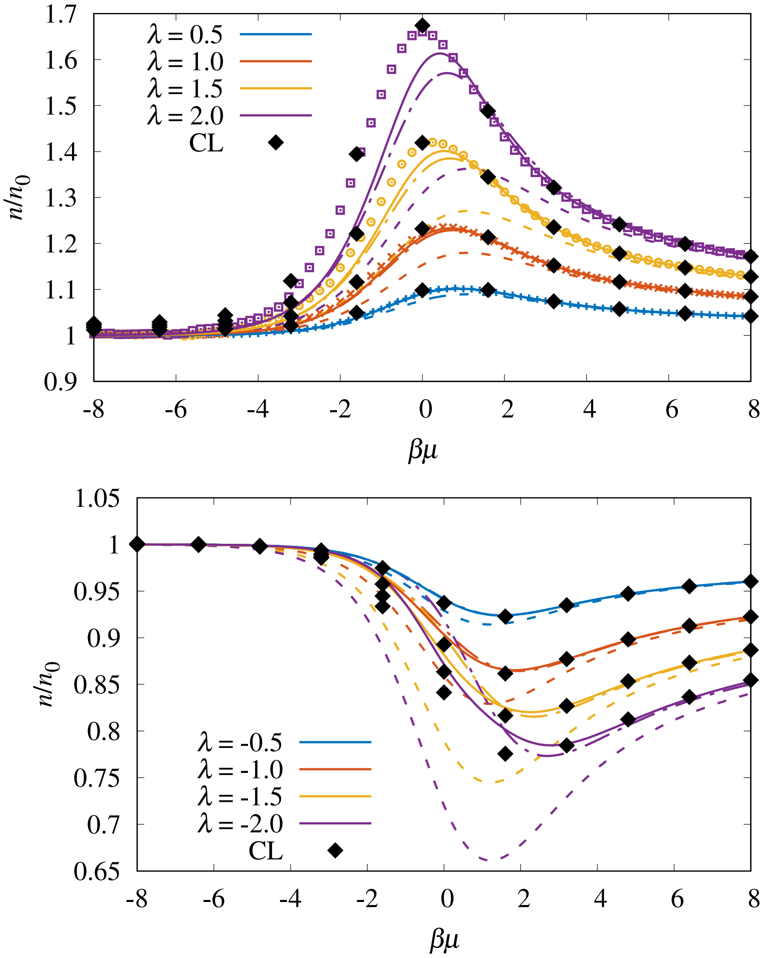

Figure 5.7: Density n of the attractive (top) and repulsive (bottom) unpolarized Fermi gas in units of the density of the noninteracting system n_0, as shown for the dimensionless interaction strengths $\lambda = 0.5$, 1.0, 1.5, 2.0 (attractive), and $\lambda = -0.5$, -1.0, -1.5, -2.0 (repulsive). The NLO (dashed line), N2LO (dash-dotted line), and N3LO (solid line) results of perturbation theory are displayed for each coupling and are compared with HMC results (see Ref. [1]) in the attractive case. For both plots, the black diamonds show CL results (RL for the attractive case), regulated with $\xi = 0.1$ as described in the main text. The statistical uncertainty of the CL results is estimated to be on the order of the size of the symbols, or less, as supported by the smoothness of those results.

For repulsive interactions, where a sign problem is present, our calculations yield the results shown in Fig. 5.7 (bottom). In both cases, we have numerically differentiated with a point spacing of $d\mu = 0.01$. Both figures also display comparisons with results obtained using complex Langevin techniques (which will be introduced in Chapter 6) and agrees well with the perturbative results across attractive and repulsive couplings.

In addition to displaying the density equation of state for weak to moderate couplings of $\lambda = \pm 0.5$ to 2.0, we display in Fig. 5.8 the density for stronger couplings of $\lambda = \pm 2.5$ to 4.0 for both perturbation theory and complex Langevin. The perturbative results, even at N3LO, fail miserably in the strongly interacting and virial regions beyond λ of 2.5; however, complex Langevin still agrees well with HMC where it is available

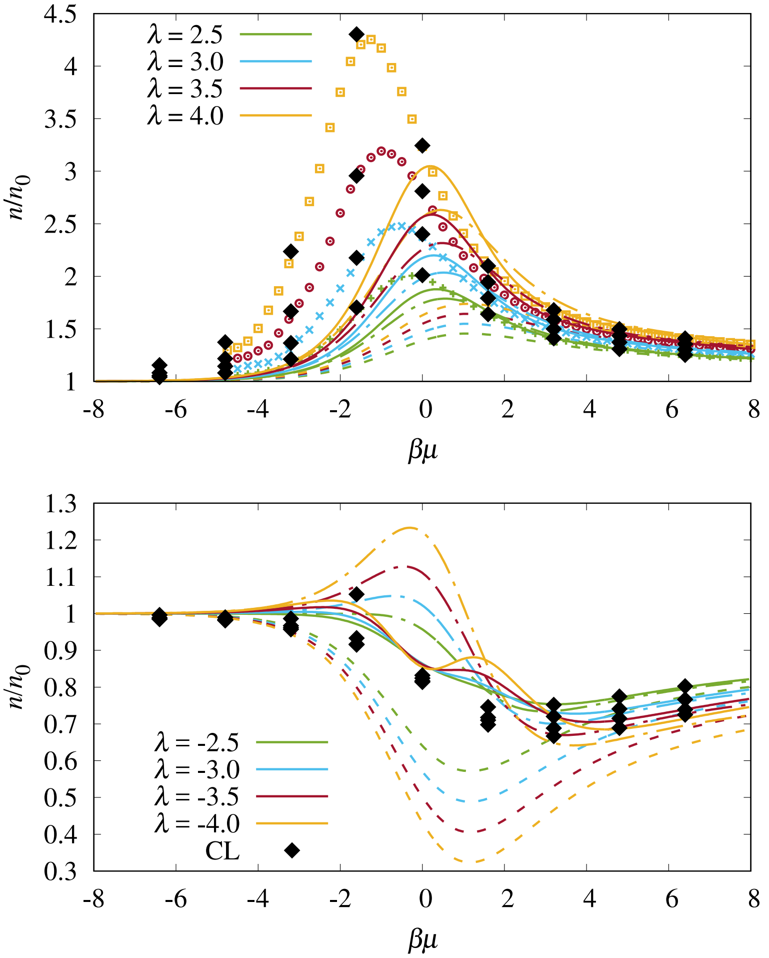

Figure 5.8: Density n of the attractive (top) and repulsive (bottom) unpolarized Fermi gas in units of the density of the noninteracting system n_0, as shown for the dimensionless interaction strengths $\lambda = 2.5, 3.0, 3.5, 4.0$ (attractive), and $\lambda = -2.5$, -3.0, -3.5, -4.0 (repulsive). The NLO (dashed line), N2LO (dash-dotted line), and N3LO (solid line) results of perturbation theory are displayed for each coupling and are compared with HMC results (see Ref. [1]) in the attractive case. It is evident that perturbation theory fails miserably at these higher couplings, and competing oscillations set in for the repulsive case. For both plots, the black diamonds show CL results (RL for the attractive case), regulated with $\xi = 0.1$ as described in the main text. The statistical uncertainty of the CL results is estimated to be on the order of the size of the symbols, or less, as supported by the smoothness of those results.

for attractive couplings. In the case of repulsive couplings, it is evident that oscillations across successive perturbative orders are setting in, and are competing to converge to the proper result.

5.2.4: Equations of state for the polarized one-dimensional system

We can extend our analysis of the perturbative expansion of the partition function for the unpolarized system to the case of a two-component spin-polarized system quite naturally, without resorting to another full derivation. Recall that $\mathcal{Z}$ for the polarized spin-1/2 system will have two distinct fermion determinants, such that

$$\mathcal{Z} = \int \mathcal{D}\sigma \ \det M_{\uparrow}(\sigma) \ \det M_{\downarrow}(\sigma) \tag{5.49}$$

where $\mu_{\uparrow} \neq \mu_{\downarrow}$. If we were to again perform the analysis to a particular order in A but keep track of the flavor labels on each term, we would arrive at the same symmetry factors and diagrams for the unpolarized case, but find that exactly half of the propagators are a function of $z_{\uparrow}$, and the remaining half are a function of $z_{\downarrow}$. This translates to modifying all of our momentum sum expressions in Tables 5.1, 5.2, and 5.3 such that they are invariant under exchange of spin-up and spin-down fermions, and considering all permutations of $z_{\uparrow}$ and $z_{\downarrow}$ across non-commuting propagators. In cases of diagrams such that the product of frequency sums are not invariant, the additional n combinations and an overall factor of $1/n$ is added, which leads to a small increase in computational complexity. For instance, S_4 has 6 combinations to consider, while S_6 has 20.

In Fig. 6.4 (deferred to Chapter 6, when we discuss CL in more detail) we display the density n/n_0 for the attractive polarized system at a constant coupling of $\lambda = 1$, and compare results across N3LO perturbation theory, complex Langevin, and results from the imaginary chemical potential technique discussed in Chapter 4. Since perturbation theory and complex Langevin are both capable of obtaining a prediction for the repulsive system, we display these results for the density at a variety of chemical potential asymmetries and a coupling of $\lambda = -1$, where the results compared across all techniques are quite satisfactory. We display additional density and polarization equations of state for the spin-polarized gas in Chapter 6, where we introduce the complex Langevin method which is capable of obtaining results outside the region of validity for perturbation theory.

5.2.5: Perturbative virial coefficients

Based on the results shown above for the pressure equation of state, we implemented a method of particle-number projection, which is well known in the area of nuclear physics, to calculate virial coefficients on the lattice perturbatively. To explain the method, recall that the virial expansion for the pressure is given by

$$\beta P V = \ln \mathcal{Z} = Q_1 \sum_{n=1}^{\infty} b_n z^n, \tag{5.50}$$

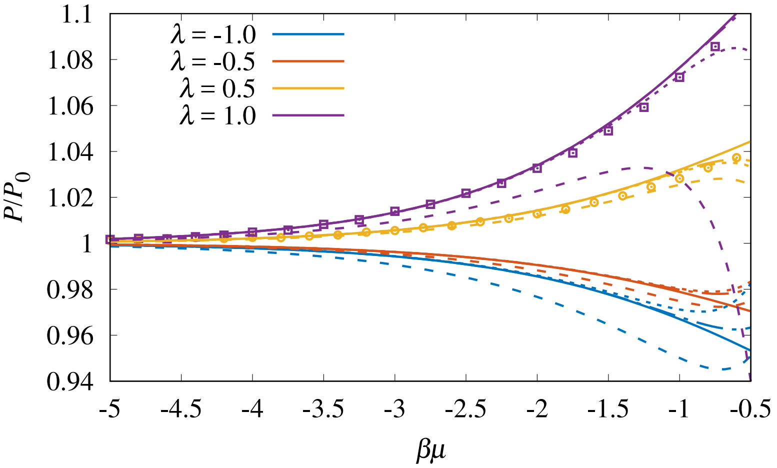

Figure 5.9: Fifth-order perturbative virial expansion for the pressure P/P_0 for two attractive and repulsive couplings. The expansions are shown for which the virial coefficients are computed at NLO (dashed line), N2LO, (dotted line), and N3LO (dash-dotted line). The fully solid line shows the full perturbative calculation of the pressure at N3LO, as shown in Fig. 5.6. Results from HMC data (see Ref. [1]) are displayed as corresponding data points for the attractive couplings.

where $Q_1 = N_f L/\lambda_T$ is the one-particle canonical partition function, $\lambda_T = \sqrt{2\pi\beta}$ is the thermal de Broglie wavelength, and b_n are the viral coefficients we want to extract.

Using our semi-analytic expressions for $\ln \mathcal{Z}(z)$, it is possible to extract the coefficients b_n via a numerical Fourier projection,

$$b_n = \frac{1}{Q_1\alpha^n}\int_0^{2\pi}\frac{d\phi}{2\pi}e^{-in\phi}\ln\mathcal{Z}(z\to\alpha e^{i\phi}), \tag{5.51}$$

where the partition function is evaluated at $z = \alpha\exp(i\phi)$ and α is an arbitrary real parameter that is independent of the result for b_n, but is used to ensure that a well-behaved integrand is used. A value of $\alpha = 0.01$ is well-suited for the evaluations performed here. An exploration of evaluating virial coefficients using a Fourier projection of the partition function but stochastically via complex Langevin was explored in Ref. [116].

We display the fifth-order perturbative viral expansion in the classical regime at NLO, N2LO, and N3LO in Fig. 5.9, which compares these results with the full perturbative calculation and with HMC data for attractive couplings. Perturbative values up to the fifth-order virial coefficient obtained using Fourier projection for four different values of the coupling are shown in Table 5.4. The perturbative expansion of virial coefficients b_n displays signs of convergence at weak coupling $|\lambda| \leq 1$ and for low enough virial order n. We find that for $\lambda = \pm1$ the predictions for b_5 cease to converge, at least at N3LO. For comparison, an exact

Table 5.4: Results for the second, third, fourth, and fifth-order virial coefficients of the pressure P [see Eq. (5.50)] at NLO, N2LO, and N3LO for two repulsive and attractive couplings. All coefficients are computed for a spatial lattice size of $N_x = 100$, $\beta = 8.0$, and a temporal lattice spacing of $\tau = 0.05$. The fifth-order virial expansion is displayed in Fig. 5.9.

λ	Coefficient	NLO	N2LO	N3LO
-1.0	b_2	-0.551	-0.473	-0.473
	b_3	0.472	0.373	0.342
	b_4	-0.452	-0.380	-0.280
	b_5	0.449	0.446	0.246
-0.5	b_2	-0.453	-0.433	-0.433
	b_3	0.333	0.308	0.304
	b_4	-0.289	-0.271	-0.259
	b_5	0.270	0.269	0.244
0.5	b_2	-0.253	-0.233	-0.233
	b_3	0.0508	0.0254	0.0295
	b_4	0.0408	0.0592	0.0461
	b_5	-0.0925	-0.0932	-0.0671
1.0	b_2	-0.152	-0.0712	-0.0712
	b_3	-0.0922	-0.194	-0.161
	b_4	0.208	0.282	0.176
	b_5	-0.276	-0.279	-0.0676

lattice calculation of the second-order virial coefficient at $N_x = 100$ and $\beta = 8$ under attractive interactions (see Ref. [1]) shows that for $\lambda = 0.5$, $b_2 = -0.230$, and for $\lambda = 1.0$, $b_2 = -0.0351$. This discrepancy compared with the perturbative value for b_2, particularly for larger values of the coupling, underscores the difficulty in quantitatively capturing the behavior in the virial region using perturbation theory.

In addition to displaying the perturbative values of the virial coefficients for a select few choices of the coupling, in Fig. 5.10 we plot b_n for $n = 2, 3, 4, 5$ and 6 as a function of the dimensionless coupling λ from the non-interacting limit to a strongly-coupled regime. Such an approximation at high interactions strengths is not expected to be reliable, but forms an interesting comparison in valid regions with stochastic methods of computing virial coefficients, as is discussed in Ref. [116].

Section 5.3: Second- and third-order Matsubara frequency sums

In this section, we will provide a listing of all Matsubara frequency sums that appear in the perturbative contributions to the grand-canonical partition function at second- and third-order. Note that the first-order sums S_1 and $S_1^{(1)}$ are provided elsewhere in the text. In all cases, our expressions were checked by comparing with a direct evaluation of the defining sums in a small spacetime volume.

The second-order frequency sum S_4 is defined as the sum over four free propagators, where the indices of the first three propagators are free, and the fourth is constrained by the momentum conservation condition

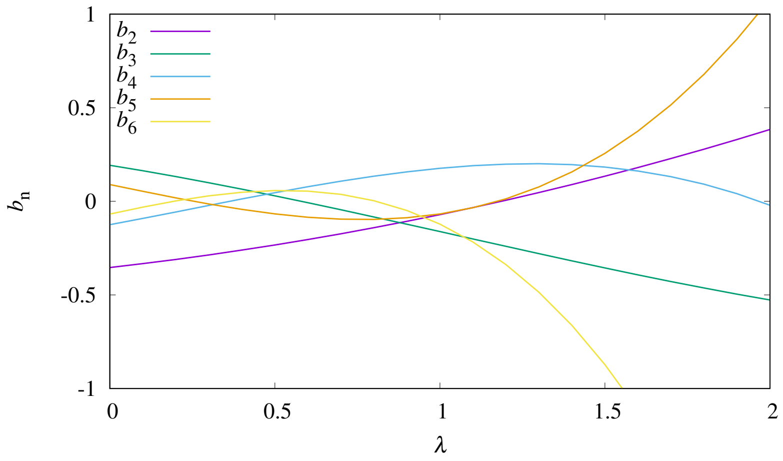

Figure 5.10: Plot of the second, third, fourth, fifth, and sixth-order virial coefficients as computed via Fourier projection under third-order lattice perturbation theory, shown as a function of the dimensionless coupling λ. The plot displays the virial coefficients from the non-interacting limit of $\lambda = 0$ to the strongly-coupled regime.

$\omega_4 = \omega_1 - \omega_2 + \omega_3$. Therefore, we write the expression for S_4 with a Kronecker delta such that

$$S_4 = \sum_{\{n\}=1}^{N_\tau} \left[\prod_{q=1}^{4} \frac{1}{1 - Q_q e^{i\omega_{n_q}}} \right] \delta(\omega_{n_3} - \omega_{n_2} + \omega_{n_1} - \omega_{n_4}). \tag{5.52}$$

After performing the procedure outlined earlier in this chapter, the final result is simply given by

$$S_4 = N_\tau^3 \left(\prod_{k=1}^{4} \frac{1}{1 + Q_k^{N_\tau}} \right) \left[1 + (Q_1 Q_3)^{N_\tau} \left(\frac{1 - X^{N_\tau}}{1 - X} - 1 \right) \right]. \tag{5.53}$$

Note that a complete derivation of S_4 is available in Ref. [112].

The frequency sum $S_1^{(2)}$ is defined as the sum over the product of three identical propagators, and the derived expression is given by

$$S_1^{(2)} = \sum_{n=1}^{N_\tau} \left(\frac{1}{1 - Q_1 e^{i\omega_n}} \right)^3 = \frac{N_\tau (2 - Q_1^{N_\tau} [N_\tau^2 + 3N_\tau - 4] + Q_1^{2N_\tau} [N_\tau^2 - 3N_\tau + 2])}{2(1 + Q_1^{N_\tau})^3}. \tag{5.54}$$

The frequency sum $S_4^{(1)}$ can be obtained, as explained in the main text, by using a differentiation trick:

$$S_4^{(1)} = - \left. \frac{dS_4(\lambda)}{d\lambda} \right|_{\lambda=1} \tag{5.55}$$

where $S_4(\lambda) \equiv \lambda^{-1} \left. S_4 \right|_{Q_1 \to Q_1/\lambda}$. Thus,

$$\begin{aligned}S_4^{(1)} &= \sum_{n_1,n_2,n_3,n_4=1}^{N_\tau} \left(\frac{1}{1-Q_1 e^{i\omega_{n_1}}}\right)^2 \frac{1}{1-Q_2 e^{i\omega_{n_2}}} \frac{1}{1-Q_3 e^{i\omega_{n_3}}} \frac{1}{1-Q_4 e^{i\omega_{n_4}}} \delta(\omega_{n_1} - \omega_{n_2} + \omega_{n_3} + \omega_{n_4}) \\ &= N_\tau^3 \left(\prod_{k=1}^{4} \frac{1}{1+Q_k^{N_\tau}}\right) \left\{ \left[1 + (Q_1 Q_3)^{N_\tau} \left(\frac{1-X^{N_\tau}}{1-X} - 1\right)\right] \left(\frac{(N_\tau - 1) Q_1^{N_\tau} - 1}{1+Q_1^{N_\tau}}\right) \right. \\ &\qquad \left. + N_\tau (Q_1 Q_3)^{N_\tau} \left[1 - \frac{1-X^{N_\tau}}{1-X} - \frac{X^{N_\tau}}{1-X} + \frac{X}{N_\tau} \frac{1-X^{N_\tau}}{(1-X)^2}\right] \right\} \qquad (5.56)\end{aligned}$$

where $X \equiv Q_2 Q_4/(Q_1 Q_3)$.

Finally, the frequency sum S_6 is defined as

$$\begin{aligned}S_6 &= \sum_{\substack{n_1,n_2,n_3,\\ n_4,n_5,n_6}} \left(\prod_{k=1}^{6} \frac{1}{1-Q_k e^{i\omega_{n_k}}}\right) \delta(\omega_{n_1} - \omega_{n_2} - \omega_{n_5} + \omega_{n_6})\, \delta(\omega_{n_3} - \omega_{n_4} + \omega_{n_1} - \omega_{n_6}) \\ &= N_\tau^4 \left(\prod_{k=1}^{6} \frac{1}{1+Q_k^{N_\tau}}\right) (S_{6A} + S_{6B} + S_{6C} + 1) \qquad (5.57)\end{aligned}$$

such that

$$S_{6A} \equiv (Q_2 Q_4)^{N_\tau} \left[\left(\frac{1-(XY)^{N_\tau}}{1-XY} - 1\right)(1 + Q_5^{N_\tau} + Q_6^{N_\tau}) + F(X,Y) Q_6^{N_\tau} + F(Y,X) Q_5^{N_\tau}\right], \qquad (5.58)$$

$$S_{6B} \equiv (Q_4 Q_6)^{N_\tau} \left(\frac{1-Y^{N_\tau}}{1-Y} - 1\right), \quad \text{and} \quad S_{6C} \equiv (Q_2 Q_5)^{N_\tau} \left(\frac{1-X^{N_\tau}}{1-X} - 1\right), \qquad (5.59)$$

where we also define

$$F(X,Y) \equiv \frac{1-Y^{N_\tau}}{1-Y} \left(1 - \frac{1-X^{N_\tau}}{1-X}\right) + \frac{1}{1-Y} \left(\frac{1-X^{N_\tau}}{1-X} - \frac{1-(XY)^{N_\tau}}{1-XY}\right), \qquad (5.60)$$

as well as $X \equiv Q_1 Q_6/(Q_2 Q_5)$ and $Y \equiv Q_3 Q_5/(Q_4 Q_6)$. As evident from the above expressions, it is important to consider limiting cases near poles (e.g. $X = 1$) when numerically evaluating these sums; such limits are straightforward to compute and implement.

Section 5.4: Object-oriented design for analytic perturbative expansions

The process of computing an analytic expression for the perturbative expansion of the grand-canonical partition function at finite temperature manually has shown to be infeasible beyond next-to-leading order, and more complex derivations demand enough computational resources to require a careful consideration of an appropriate software implementation to perform such a task. The scaling of both utilized memory and processing resources with the perturbative order of the calculation scales dramatically, and the use of parallelism adds great benefit at N4LO and beyond for even unpolarized systems. In the following section, in order to bridge the gap between the mathematical formalism and actual practice and implementation, we will provide a high-level overview of the software design used to derive the expressions for the perturbative contributions shown in previous discussions.

The implementation used to produce the results in this work was written in C++ and takes an object-oriented approach which does a significant portion of the "analytic heavy lifting", in the sense that common mathematical manipulations can be expressed in terms of recursive or iterative actions on collections of objects which symbolically represent items defined by the perturbation formalism. Operations such as expanding out the product of multiple sums and combining like terms become straightforward processes in such an implementation, particularly when abstracted to higher levels. The language of C++ was chosen specifically for the ability to directly manage memory of object allocation. A prototype of the software was written in Python, but it quickly became evident that garbage collection provided by the standard interpreter was not efficient enough on workstations with moderate resources, and a lower-level implementation would be required. A straightforward port to C++ provided greatly improved performance.

All of the classes defined in the implementation which represent mathematical objects in the formalism are shown in an abbreviated class diagram in Fig. 5.11. All such classes inherit the base class `SymbolicTerm` which provides a basic interface for identifying the type of an instance, generating pointers to copies of an instance, tracking spatial or temporal indices assigned to an object, as well as other tasks. They may conceptually be divided into two categories (a second level of inheritance was deemed to be unnecessary in this case). One set of objects represent various expressions (which we call here *expression objects*), such as a sum of terms, a product of factors, or a trace over expressions. Items stored in these data structures may themselves be expression objects such that a tree is generated. The elements, or child nodes, of each of these objects are stored in a `vector<SymbolicTerm>` container; since objects may generally be non-commuting, it is important to maintain an ordered set. On the other hand, a variety of classes for objects which explicitly represent mathematical objects (such as particular scalars, matrices, and functions) are defined, and are leaves of any generated expression tree. Note that in the case of representing matrices, the analytic code does not explicitly store or calculate elements of these matrices; such details are reserved for numerically

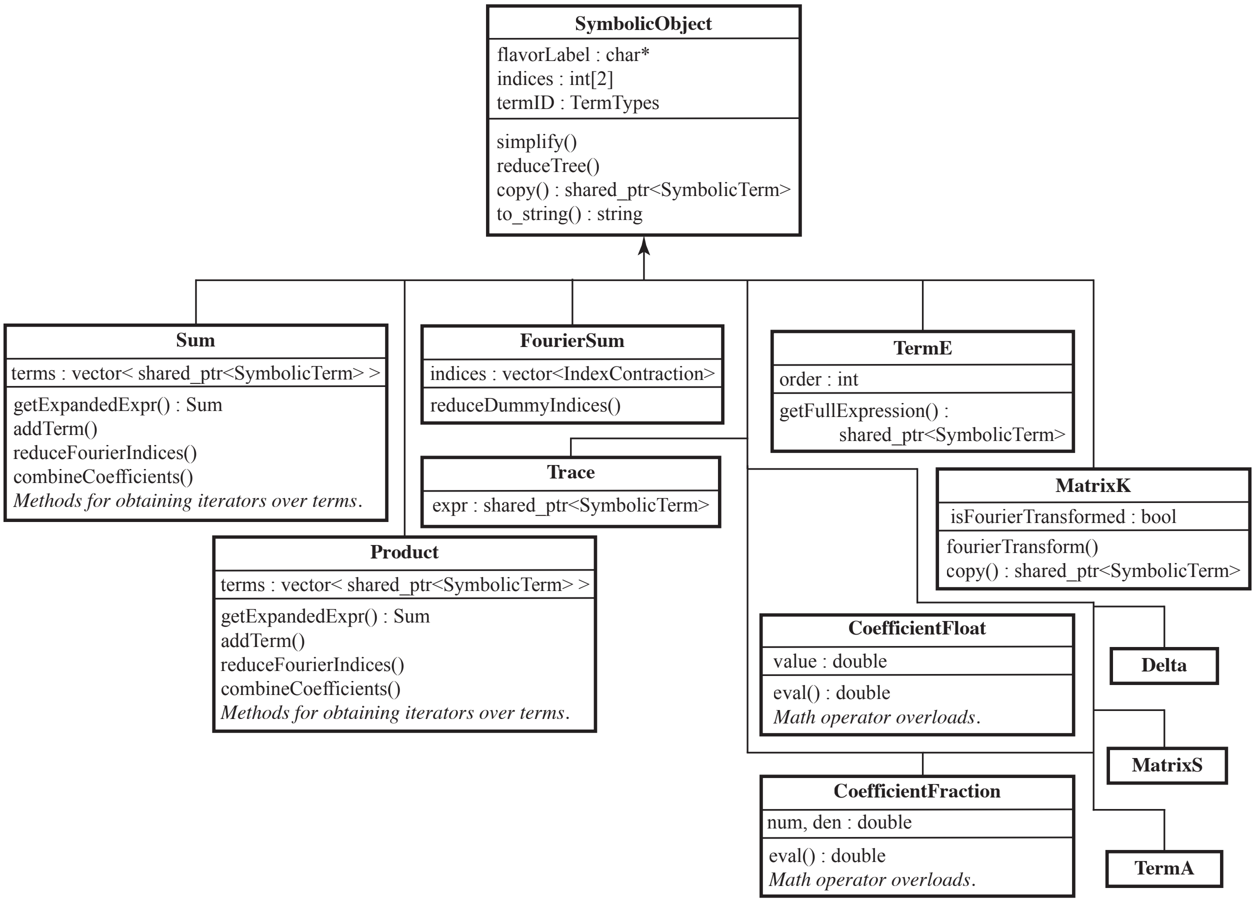
SymbolicObject
flavorLabel : char*
indices : int[2]
termID : TermTypes
simplify()
reduceTree()
copy() : shared_ptr<SymbolicTerm>
to_string() : string
Sum
terms : vector< shared_ptr<SymbolicTerm> >
getExpandedExpr() : Sum
addTerm()
reduceFourierIndices()
combineCoefficients()
Methods for obtaining iterators over terms.
FourierSum
indices : vector<IndexContraction>
reduceDummyIndices()
TermE
order : int
getFullExpression() : shared_ptr<SymbolicTerm>
Trace
expr : shared_ptr<SymbolicTerm>
MatrixK
isFourierTransformed : bool
fourierTransform()
copy() : shared_ptr<SymbolicTerm>
Product
terms : vector< shared_ptr<SymbolicTerm> >
getExpandedExpr() : Sum
addTerm()
reduceFourierIndices()
combineCoefficients()
Methods for obtaining iterators over terms.
CoefficientFloat
value : double
eval() : double
Math operator overloads.
Delta
MatrixS
CoefficientFraction
num, den : double
eval() : double
Math operator overloads.
TermA

Figure 5.11: Reduced class diagram for the C++ implementation of computing the analytic expressions for perturbative contributions to the grand-canonical partition function. All objects used in the calculation are derived from the `SymbolicTerm` class, and can be broken into two categories. The left hand side of the diagram contains expression objects which are containers for pointers to one or more `SymbolicTerm` instances (which itself may resolve to an expression object), and the right hand side of the diagram shows terminal objects which are representations of mathematical objects that appear in the perturbation theory formalism. For brevity, this diagram only displays particular methods and fields discussed further in the text below. In addition, each class typically provides relevant operator overloads to define particular behaviors, as well as overriding implementations of `SymbolicTerm::copy()` and `SymbolicTerm::to_string()`.

evaluating the expressions later on once the analytic form of the perturbative expansion is obtained.

The calculation of perturbative expansion of the partition function in terms of Feynman diagrams proceeds in several distinct stages:

1. The evaluation of a determinant of a single fermion matrix M proceeds according to the prescription provided in Sec. 5.1.2. To consider the case of several flavors of particles, a "flavor label" is assigned to each object. The series in powers of A with the corresponding factors of E_k are generated on-the-fly using the methods provided by the `TermA` and `TermE` classes. Functions for calculating the Taylor series of e^x using the `Sum`, `Product`, and `CoefficientFraction` classes are provided.

2. After the expansion of a single determinant is obtained, a product of determinants is taken and expanded, or equivalently, the appropriate factor of the number of flavors N_f is included beforehand in the definition of E_k [see below Eq. (5.16)]. The expansion is truncated to the power of A desired, and terms which are in odd powers of A are removed (since they will always vanish).

3. The arguments of `Trace` objects are provided indices such that the expression is given in an implied summation notation; for instance, consider the rewriting

$$\mathrm{Tr}(K_\uparrow \mathcal{S} K_\downarrow \mathcal{S}) \to \sum_{i,j} K_{\uparrow\, i,j}\, \mathcal{S}_{j,k}\, K_{\downarrow\, k,\ell}\, \mathcal{S}_{\ell,i}. \tag{5.61}$$

4. At this point, the path integral of each term in the expansion can be evaluated over products of the form $K_{ab}\mathcal{S}_{bc}K_{cd}\mathcal{S}_{de}\cdots K_{fg}\mathcal{S}_{ga}$, whose path integral will be of the form

$$K_{ab}K_{cd}\cdots K_{fg}\int \mathcal{D}\sigma\, \mathcal{S}_{bc}\mathcal{S}_{de}\mathcal{S}_{ga}, \tag{5.62}$$

   where in text we have referred to the integral as $I_n(a,b,c,\ldots)$, where the integrand is n-th order in the matrix $\mathcal{S}$. A separate function determines I_n in terms of the appropriate numerical coefficients and Kronecker delta functions of the indices $a,b,c,\ldots$, where the relevant mapping between the generic indices and those appearing in the integrand expression is implicitly understood. This computation involves calculating all possible "contractions" of order n, or all the possible ways in which a non-vanishing contribution to the path integral can group σ-fields together; each such contraction contributes one term to the integral I_n. A variety of additional classes and structures are written to handle this with clarity.

5. After computing the path integral and fully expanding the result, we are left with an expression of the form $K_{0,1}K_{2,3}\cdots\delta_{ij}\delta_{kl}\cdots$, where integers refer to spacetime indices and lowercase letters indicate momentum-frequency indices. To proceed further, we must symbolically transform the matrix K to the free propagator D which is written in the momentum-frequency basis, and insert the resulting sums from this transform. This introduces the `FourierSum` class, which represents a set of sums over spacetime indices, and can handle a basic elimination of redundant indices. Once the calculation is complete, the contents of this object can be used to quickly determine the Feynman diagram corresponding to a given term in the expansion.

6. At this point, the calculation is complete, but terms of the same type of diagram must be combined to simplify the expression. The number of terms present at this point is far too large to be able to do this manually. The new `FeynmanDiagram` and `Vertex` classes are used to identify topologically identical diagrams based on the indices of the free propagators. Similar diagrams are then combined together using a separate function, which breaks the sum into smaller parts to make this computation more manageable.

At this stage the work of the software described at the beginning of this section is complete, and the contributing terms are output in the general form $\frac{a}{b}A^n K_{0,1}K_{2,3}\cdots K_{2n-2,2n-1}$ where the Fourier transform has rendered K_{ab} to

$$K_{ab} = \sum_{ab} U^{\dagger}_{ai} D_i U_{ib}. \tag{5.63}$$

The collection of spacetime indices which transform to the diagonal momentum-space representation are stored in the `FourierSum` object and are written with each contributing term, for instance an N2LO term can be presented as

```
{-1 / 4} {A} {A} {A} {A} D_{0, 1} D_{2, 3} D_{4, 5} D_{6, 7}
FourierSum[(0, 1) (1, 0) (0, 0) (0, 0)]
```

where here the argument of the `FourierSum` represents

$$\sum_{0,1} U^{\dagger}_{0i} U_{i1} U^{\dagger}_{1j} U_{j0} U^{\dagger}_{0k} U_{k0} U^{\dagger}_{0\ell} U_{\ell 0}. \tag{5.64}$$

A final step to arrive at the form of the expressions in Tables 5.1, 5.2, and 5.3 is to consider momentum conservation conditions. As an example, rearranging the explicit form of the Fourier sum of the above expression gives

$$\begin{aligned} D_i D_j \sum_{0,1} e^{p_i(x_0-x_1)} e^{p_j(x_1-x_0)} &= D_i D_j \left(\sum_{0} e^{x_0(p_i-p_j)} \right) \left(\sum_{1} e^{x_1(p_j-p_i)} \right) && (5.65) \\ &= D_i D_j \delta(p_i - p_j) \delta(p_j - p_i) && (5.66) \end{aligned}$$

where x_n are spatial coordinates and p_n are momenta. We can see here that $p_i = p_j$, which results in the final expression D_i^2, corresponding to frequency sum S_1.

CHAPTER 6: Complex Langevin Dynamics

In the first few chapters of this thesis, the hybrid Monte Carlo (HMC) method was applied to unpolarized and spin-polarized systems (in the case of iHMC) of fermions with contact interactions in one dimension. Although the HMC algorithm was an efficient method to solve for the equations of state of these problems, it has a significant drawback – any system of interest must be free of the sign problem, since the Metropolis algorithm no longer functions when the action used as the probability measure fluctuates in sign. Generally, there exist many more physical systems we would like to study which present a sign problem, than those that do not. As such, we would like to continue exploring techniques to avoid this roadblock. One method to circumvent the sign problem which we propose and develop in this chapter, is the complex Langevin method.[1] This technique has gathered considerable attention in the area of finite-density lattice QCD [117–126], but its application to non-relativistic latter is extremely limited (see, however, Refs. [127, 128]).

The Langevin equation was originally proposed [129] as a method to study the motion of a particle in a fluid experiencing Brownian motion as a stochastic differential equation [130] for the particle's trajectory $\mathbf{x}(t)$:

$$m\ddot{\mathbf{x}} = -\alpha\dot{\mathbf{x}} + X \tag{6.1}$$

where m is the mass of the particle, α is a parameter related to the viscosity of the fluid, and X is a term which Langevin refers to as the *complementary force* over which the average behavior over an ensemble of particles can be evaluated. Langevin concluded that this analysis exactly reproduces the result for the mean squared displacement of a particle experiencing Brownian motion after a given time, as first predicted by A. Einstein. In the case of our QMC studies, we instead imagine the trajectory through configuration space of the auxiliary field experiencing stochastic noise according to a particular probability distribution. Additionally, we allow our field variables to be complex, such that the random walk can wander around the complex plane. This is in direct contrast to the HMC approach, where instead the trajectory is governed by the Metropolis algorithm. Although this modification avoids the sign problem in principle, in practice the complex Langevin algorithm does not come without its own price. In fact, much of the complex Langevin algorithm in the context of auxiliary field techniques is still under active investigation.

---

[1] This chapter is based in part on the work published in Refs. [112, 113].

Section 6.1: Formulation of the complex Langevin approach for QMC

As previously alluded to, the basic idea to the complex Langevin approach is to make the auxiliary field variable σ complex, introduce a noise term $\eta(x, \tau)$ to the dynamical equations of motion, and eliminate the Metropolis step present in HMC implementations. The starting point is once again the grand-canonical partition function

$$\mathcal{Z} = \int \mathcal{D}\sigma \, \det{}^2 M[\sigma], \tag{6.2}$$

where one normally identifies $P[\sigma] = \det{}^2 M[\sigma]$ as the unnormalized probability measure to be used in a Metropolis-based Monte Carlo calculation. One further defines an effective action S via $P[\sigma] = \exp(-S[\sigma])$. Most physical observables can then be shown to take the form

$$\langle O \rangle = \frac{1}{\mathcal{Z}} \int \mathcal{D}\sigma \, e^{-S[\sigma]} O[\sigma], \tag{6.3}$$

such that the expectation value can be determined by importance sampling the auxiliary field σ according to the weight $P[\sigma]$. We have already established hybrid Monte Carlo as a well-known way of carrying out such sampling, so long as $P[\sigma]$ satisfies the requisite properties. Additionally, the *real Langevin* (RL) method, also known simply as stochastic quantization (see, e.g., Refs. [131–133]), can also typically be used in cases where HMC does not have a sign problem. In this situation, the auxiliary field resorts to be a real field, and the complex Langevin method reduces to what is known as real Langevin. When performing calculations in the complex plane, computations for observables which could otherwise be done using RL will naturally find themselves restricted to the real axis; any initial imaginary part of the observable will decay to zero.

Recall that in HMC, one defines a secondary auxiliary field variable π which is conjugate to the HS field σ with global, molecular-dynamics type equations of motion in a fictitious phase-space time t which provide global configuration updates, such that

$$\begin{aligned} \dot{\sigma} &= \pi, && (6.4) \\ \dot{\pi} &= -\frac{\delta S[\sigma]}{\delta\sigma}. && (6.5) \end{aligned}$$

Note that the right-hand side of the last equation represents a functional derivative of the action S, and naturally represents a molecular dynamics force. In the RL method, on the other hand, the Metropolis step is removed, and the equations of motion are modified such that

$$\dot{\sigma} = -\frac{\delta S[\sigma]}{\delta\sigma} + \eta, \tag{6.6}$$

where there is no longer an auxiliary momentum field π and a t-dependent noise field η appears instead. Note that η cannot be just any chosen random noise field, but should satisfy particular properties, namely such that the mean satisfies $\langle\eta(x,\tau)\rangle = 0$ and spacetime correlations satisfy $\langle\eta(x,\tau)\eta(x',\tau')\rangle = 2\delta_{x,x'}\delta_{\tau,\tau'}$.

Conventionally, recall that the mathematical underpinnings of HMC and RL depend on the probability distribution $P[\sigma]$ being positive semidefinite. As is well known, this property generally fails to hold, for instance, for repulsive interactions and polarized systems, and the calculation is then said to have a sign problem (or more generally, a complex phase problem). In the case of HMC, this implies that the Metropolis step is no longer well-defined, and the guarantees that algorithm provides is no longer provided, which renders HMC unavailable. Although RL does not include such a Metropolis step, one can observe that the resulting sign problem causes the algorithm to converge to the incorrect result, if it even converges at all. A generalization of RL is possible, namely complex Langevin (CL), as is first noted in Ref. [134]. In this case, one complexifies the HS auxiliary field σ into

$$\sigma = \sigma_R + i\sigma_I, \tag{6.7}$$

where the new auxiliary fields σ_R and σ_I are both real. The resulting equations of motion are given as

$$\begin{aligned} \delta\sigma_R &= -\mathrm{Re}\left[\frac{\delta S[\sigma]}{\delta\sigma}\right]\delta t + \eta\sqrt{\delta t}, && (6.8) \\ \delta\sigma_I &= -\mathrm{Im}\left[\frac{\delta S[\sigma]}{\delta\sigma}\right]\delta t. && (6.9) \end{aligned}$$

Here the action $S[\sigma]$ is to be understood as a complex function of the complex variable σ. Note that, when the action is real, the imaginary part of the force vanishes and then CL reduces to RL. In particular, when applied to the case of fermions with contact interactions, we will see that for the attractive case, where there is no sign problem present, σ is real and the CL simulation behaves as RL.

6.1.1: Complex Langevin pitfalls

Under certain conditions, which have lately received much attention (see, e.g., Ref. [135]), the CL method can be guaranteed to converge to the right answer. However, such guarantees come for limited cases and are difficult to prove, and typically do not apply to many physical systems. In such situations, expectation values $\langle O \rangle$ are correctly obtained by averaging over the real part of $O[\sigma]$ given complex fields σ samples throughout the CL dynamics evolution. In particular, for the model we study here, it is *a priori* not known if CL will converge to the correct result; one goal of the work in this chapter is to explore the viability of CL for this class of systems.

In the process of making CL a viable solution to the sign problem in lattice QCD, two crucial challenges were identified: the appearance of numerical instabilities in the CL evolution, and the uncontrolled excursions of σ into the complex plane due to singularities in $P[\sigma]$. The former was largely resolved by implementing adaptive time-step solvers [136] (which we also use in this work); the latter, on the other hand, is currently under investigation and a few approaches have been proposed (see, e.g., Refs. [137, 138]). In the calculations presented here, those excursions are highly problematic because of the dependence of $P[\sigma]$ on σ_I is through hyperbolic functions; one may easily see this by inspecting the HS transformation used and noting the dependence on $\sin \sigma$, and

$$\sin \sigma = \sin(\sigma_R + i\sigma_I) = \sin(\sigma_R)\cosh(\sigma_I) + i\cos(\sigma_R)\sinh(\sigma_I). \tag{6.10}$$

Therefore, a growing (positive or negative) σ_I effectively increases the coupling at an exponential rate (recall for the transform we use, roughly $e^{\tau \hat{V}} \sim A \sin \sigma$), which can completely stall the calculation or result in a converged but wrong answer, as we have observed in a variety of our tests. This exponential growth is similar to the problem found in gauge theories, as complexified link variables representing the gauge field become unbounded in the same fashion in those theories.

6.1.2: Modified action

Throughout our tests of the application of complex Langevin to fermionic systems with contact interactions, we determined that the straightforward application of Eqs. (6.8) and (6.9) is far too susceptible to uncontrolled excursions into the complex plane, as discussed in the previous section. In order to overcome this problem, we modified the action in a way reminiscent of the dynamical stabilization approach of Refs. [139, 140]. In the latter, a new term was added to the CL dynamics which vanishes in the continuum limit and renders the calculation stable. A technical distinction between the modification we make here and the approach of dynamical stabilization, is that in the second, the term added to the equations of motion is not holomorphic.

We propose here to modify the CL equations by adding a regulating term controlled by a parameter ξ, such that the new equations, in their discretized form, are given as

$$\delta\sigma_R = -\mathrm{Re}\left[\frac{\delta S[\sigma]}{\delta\sigma}\right]\delta t - 2\xi\sigma_R\delta t + \eta\sqrt{\delta t}, \tag{6.11}$$

$$\delta\sigma_I = -\mathrm{Im}\left[\frac{\delta S[\sigma]}{\delta\sigma}\right]\delta t - 2\xi\sigma_I\delta t. \tag{6.12}$$

From the perspective of molecular dynamics in the context of hybrid Monte Carlo, one can see that this change amounts to modifying the action with a term which is quadratic in the auxiliary field,

$$S[\sigma] \to S[\sigma] + \xi\sum_{\mathbf{x},t}\sigma^2. \tag{6.13}$$

The rationale for adding such a regulating term was originally based on our understanding of $\delta S[\sigma]/\delta\sigma$ as a molecular dynamics force in the HMC algorithm (although it is typically referred to as the "drift" in the literature regarding the CL method). In the sense of this dynamical force, the new term in the action can be understood as a harmonic oscillator trapping potential, i.e. a restoring force that prevents the field from exponentially running away. However, we know that HMC does not apply when σ is complex; a more appropriate interpretation is obtained by keeping only those new terms in the CL equations and neglecting the rest, which results in the decoupled form

$$\delta\sigma_R = -2\xi\sigma_R\delta t, \tag{6.14}$$

$$\delta\sigma_I = -2\xi\sigma_I\delta t, \tag{6.15}$$

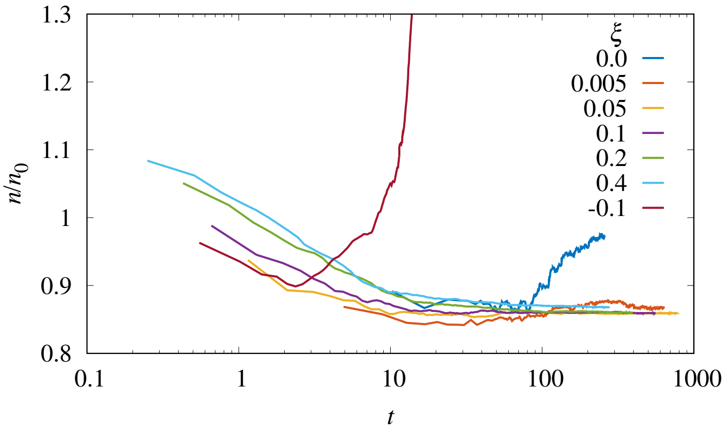

Figure 6.1: The normalized density n/n_0, where n_0 is the noninteracting result, for $\lambda = -1.0$ and $\beta\mu = 1.6$, as a function of the Langevin time t for several values for the regulating parameter ξ [see Eq. (6.13)]. The result was computed on a spatial lattice of $N_x = 80$ and a temporal lattice of $N_\tau = 160$. For a choice of $\xi = 0$, where the regulating term is removed, CL tends toward an incorrect value for the density. When $\xi \simeq 0.1$, the additional term provides a restoring force and the stochastic process converges to a different value consistent with perturbation theory. On the other hand, for cases where $\xi < 0$, the solution diverges, as expected. Each plotted line corresponds to a fixed count of 10^5 iterations of performing one integration step of the adaptive step δt; as such, the length of the line gives an indication as to the computational demand to reach time t for a given ξ.

whose solution is a decaying exponential (assuming $\xi > 0$) for both σ_R and σ_I. Thus, this new *ad hoc* term represents a damping force. In principle, one could additionally explore anharmonic damping term, such as a regulated term proportional to σ^4. Such an addition may more quickly bound runaway excursions, but one must balance this behavior with allowing the system to explore appropriate regions of configuration space.

Naturally, the proposed modification introduced a systematic effect that needs to be studied for each quantity of interest, i.e. it is crucial to understand the ξ dependence of the output. The results previously presented in Figs. 5.6 and 5.7 correspond to $\xi = 0.1$. To gain specific insight into the variations of the density with ξ, we show in Fig. 6.1 a plot of the running average of the density as a function of the Langevin time t for several values of ξ in the neighborhood of zero. As evident in that figure, there is a sizable window of small values of ξ where CL converges. Additionally, we show in Fig. 6.2 a plot of the phase and magnitude of e^{-S}, where S is the complex action, for different values of ξ. The effect of the ξ term on the CL dynamics can be clearly seen in that figure (note the change of scale for the $\xi < 0$ plot, where the results are expected to diverge).

Section 6.2: Unpolarized equation of state using complex Langevin

We have previously displayed the pressure and density equations of state of the one-dimensional balanced system of fermions in Figs. 5.6 and 5.7 where the CL predictions were used to validate results obtained for N3LO perturbation theory. Higher coupling results from CL were also compared against HMC in Fig. 5.8

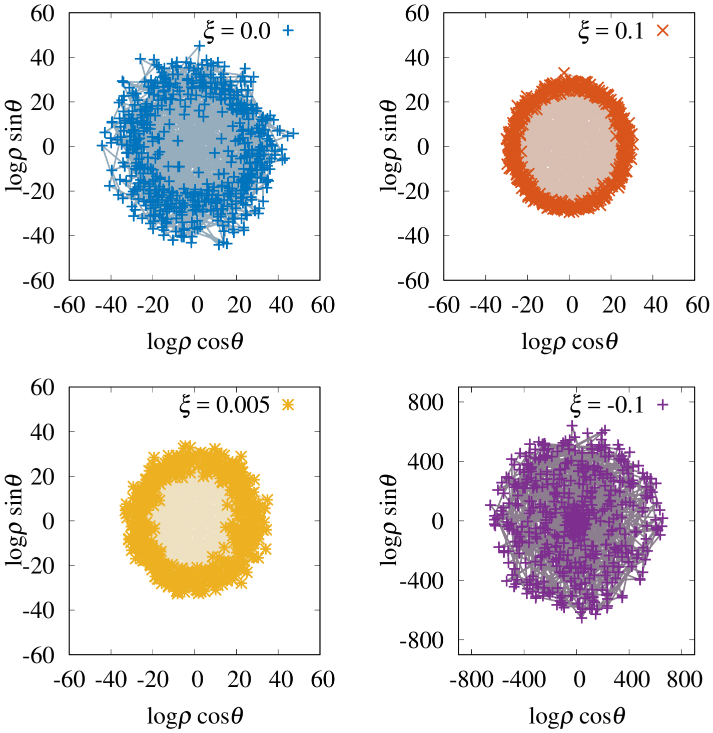

Figure 6.2: Plot of the complex quantity e^{-S} in terms of its magnitude ρ and phase θ such that $e^{-S} = \rho e^{i\theta}$, for a CL calculation at $\lambda = -1.0$ and $\beta\mu = 1.6$. Data points are plotted as $\ln(\rho)\cos(\theta)$ and $\ln(\rho)\sin(\theta)$ as parametric functions of the Langevin time t. Plots are displayed for four values of the parameter ξ. Note that for $\xi = 0$, the solution does not converge, but does converge for $\xi = 0.005$ and 0.1. For the case where $\xi = -0.1$, the result for the density n/n_0 rapidly diverges, as expected [note change in scale for y axis and see Fig. 6.1]. Data points show the locations where samples were taken along the CL trajectory; the shaded areas result from straight lines joining the data points.

where perturbation theory drastically breaks down. For both repulsive and attractive interactions, CL reproduces the N3LO result to high accuracy in regimes where it is expected to be valid. Where perturbation theory fails at high couplings strengths or within the virial region, CL agrees with both the virial expansion and HMC, where available (see in particular the figures presented in the following section for curves corresponding to vanishing polarization). Even though CL is not necessarily guaranteed to converge *a priori* to the correct expectation value, these studies with the addition of the modified action agree well with other known techniques (where applicable), indicating that it does seem to properly converge for this model. Overall, the results obtained for the equation of state of the balanced system indicated that the algorithm could be viable for use in the spin-polarized system.

In order to further assess whether the simulation encounters singularities in the drift and that excursions into the complex plane are reasonably constrained, we display a histogram of the absolute value of the action, $-S \simeq \ln|\det M|$ in Fig. 6.3. The important quantity to consider is the magnitude of $\det M$, since a vanishing determinant would result in a divergence when integrating the equations of motion. We show such plots for both the strongest and weakest couplings and for values of the chemical potential primarily in the strongly interacting region where the density deviates the most from the noninteracting value. This approximately log-normal distribution is consistently well-defined across parameter values with a reasonable width, even though the magnitude of the action may vary across $\beta\mu$. In this respect, there is assurance that the flow of the simulation is well-controlled and not subject to severely problematic points. The scatter plot of e^{-S} corresponding to $\xi = 0.1$ in Fig. 6.2 also supports this finding; the distribution of the magnitude of this quantity is well contained and is symmetric on the complex plane.

Section 6.3: Spin-polarized fermions using complex Langevin

In the previous section, we discussed equation of state results for unpolarized fermions as calculated using CL and compared those results with N3LO perturbation theory and HMC. Here we turn once again to calculating the equation of state for *spin-polarized* spin-1/2 fermions as we did with iHMC in Chapter 4, but with the CL method, which does not require fitting data on the imaginary axis and taking an analytic continuation to the physical observables. In addition to the increased simplicity of the technique for avoiding the sign problem, we note that CL is not subject to the prohibitive statistical noise that appears at strong couplings under iHMC, and also may remain valid for parameter space regions where phase transitions occur. These difficulties made studies in higher dimensions impractical using iHMC, but have succeeded

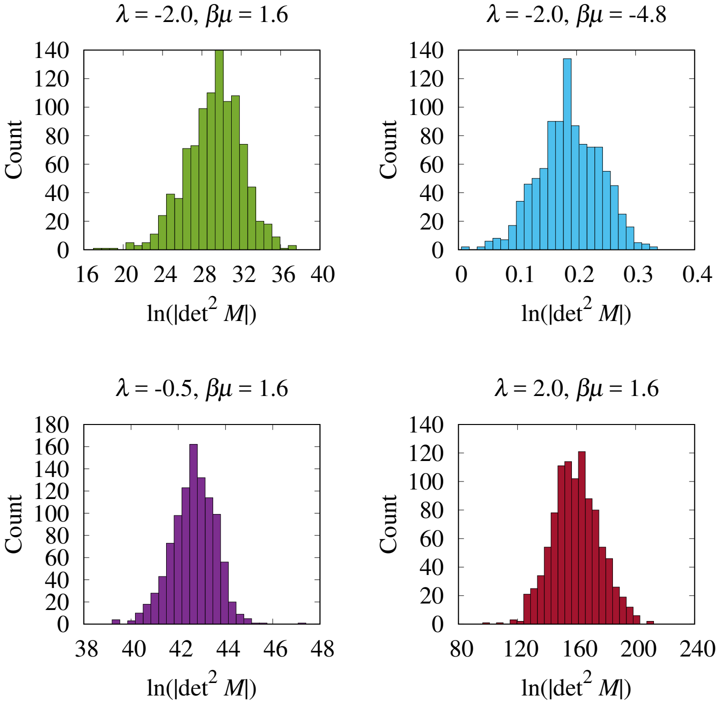

Figure 6.3: Histograms of values taken of $2\ln(|\det M|)$ over the course of a CL simulation at $\xi = 0.1$ for a few representative values of the coupling λ (shown primarily on the repulsive side and for the strongest coupling) and the chemical potential $\beta\mu$ (shown in the virial and strongly interacting regions). The distributions across parameter values appear approximately log-normal and well behaved, and indicate that the drift force is generally free of singularities. Although the magnitude of the action can vary across parameter space, the variance across field configurations is centered about a well-defined mean.

under CL, as we present in Chapter 7. For now, let's review the results and analysis for the system in one spatial dimension.

We again consider the same Hamiltonian as Eq. (3.1) for two particle species,

$$\hat{H} = -\frac{\hbar^2}{2m}\sum_i \nabla_i^2 - g\sum_{i<j}\delta(x_i - x_j) \tag{6.16}$$

where the sums over i and j are taken over all particles for spin-up ($\uparrow$) and spin-down ($\downarrow$) species. The grand-canonical partition function is, as usual, $\mathcal{Z} = \mathrm{Tr}\left[e^{-\beta\hat{K}}\right]$ for $\hat{K} = \hat{H} - \mu_\uparrow\hat{N}_\uparrow - \mu_\downarrow\hat{N}_\downarrow$, where μ_s and $\hat{N}_s$ are the chemical potential and particle number operators for the corresponding species, respectively. To address the polarized systems, we again adopt the notation

$$\mu \equiv \frac{\mu_\uparrow + \mu_\downarrow}{2} \tag{6.17}$$

$$h \equiv \frac{\mu_\uparrow - \mu_\downarrow}{2} \tag{6.18}$$

such that $\mu_\uparrow = \mu + h$ and $\mu_\downarrow = \mu - h$. The parameter h is referred to as the chemical potential asymmetry, and is also made a dimensionless quantity via a factor of β. The same Hubbard-Stratonovich transformation as used in previous chapters is applied to this Hamiltonian, where the partition function is evaluated over a determinant for each spin:

$$\mathcal{Z} = \int \mathcal{D}\sigma\ \det(1 + z_\uparrow\mathcal{U}[\sigma])\ \det(1 + z_\downarrow\mathcal{U}[\sigma]). \tag{6.19}$$

Note that unlike the case where we sampled this path integral using an imaginary polarization, these determinants are not complex conjugates of one another and the integrand in general is a complex quantity even under attractive interactions. The density is evaluated similarly to the unpolarized case, with the exception that derivatives of $\ln\mathcal{Z}$ are taken with respect to $\beta\mu_\uparrow$ and $\beta\mu_\downarrow$, producing $n_\uparrow$ and $n_\downarrow$, respectively.

These computations using CL and PT were performed on a lattice size of $N_x = 61$ and $N_\tau = 160$ and are compared with the third-order virial expansion within the region of validity. In the case of $\lambda = 1$, which corresponds to an attractive interaction, we additionally compare with the data of Chapter 4 (also see Ref. [2]) which was obtained using iHMC. The temporal lattice spacing was again set to $\tau = 0.05$ such that $\beta = \tau N_\tau$. In contrast to the unpolarized results shown above, the evolution was performed using an adaptive Euler integrator (replacing adaptive fourth-order Runge-Kutta) for a total of 10^5 iterations, where the first

10% of samples were discarded to thermalize the system and improve convergence properties.

6.3.1: Third-order virial expansion

In previous chapters, we have routinely used the second-order virial expansion to compare Monte Carlo results for equations of state in the limit of small fugacity. We will now introduce the virial expansion to third-order, which naturally contains information relevant to the three-body system. Only one third-order coefficient is required to describe a polarized spin-1/2 system. Additionally, instead of using the full virial coefficients b_n, we will find it more convenient to write it as $\Delta b_n = b_n - b_n^{(0)}$, the value relative to the non-interacting case. Therefore, the expansion of the pressure for a polarized gas takes the form

$$\beta \Delta P V = \ln\left(\frac{\mathcal{Z}}{\mathcal{Z}_0}\right) = Q_1 \sum_{n,m=1}^{\infty} \Delta b_{n,m} z_\uparrow^n z_\downarrow^m. \tag{6.20}$$

By writing down the grand-canonical partition function in terms of the (n, m)-particle canonical partition functions $Q_{n,m}$, one can see that

$$\begin{aligned} \Delta b_{1,1} &= \Delta b_2, & (6.21)\\ \Delta b_{2,1} &= \Delta b_{1,2} = \frac{\Delta b_3}{2}. & (6.22) \end{aligned}$$

This provides the virial expansion up to third order for the polarized case entirely in terms of the unpolarized coefficients; i.e. all information regarding the chemical potential asymmetry is separated into the two fugacity factors $z_\uparrow$ and $z_\downarrow$. Therefore, if we define n_0 as the noninteracting unpolarized result, and $n^{(\mathrm{ni})}$, $m^{(\mathrm{ni})}$ as the noninteracting polarized result, then for the density up to third order,

$$\frac{n}{n_0} = \frac{Q_1}{n_0 V}\left[2\Delta b_2 z_\uparrow z_\downarrow + \frac{3}{2}\Delta b_3 (z_\uparrow^2 z_\downarrow + z_\uparrow z_\downarrow^2)\right] + \frac{n^{(\mathrm{ni})}}{n_0}. \tag{6.23}$$

Similarly for the magnetization,

$$\frac{m}{n_0} = \frac{Q_1}{n_0 V}[\Delta b_3 (z_\uparrow^2 z_\downarrow - z_\uparrow z_\downarrow^2)] + \frac{m^{(\mathrm{ni})}}{n_0}. \tag{6.24}$$

Naturally, these expressions must be symmetric under exchange of spin-up and spin-down particles. We plot the evaluation of this expansion in the figures below in comparison with CL results.

6.3.2: Density equation of state

In Fig. 6.4 we show our results for the density equation of state of the spin-polarized Fermi gas at a coupling strength of $\lambda = 1$ (top) and $\lambda = -1$ (bottom) as a function of $\beta\mu$ and varying chemical potential asymmetry $\beta h = 0$ to 2. Additionally, the corresponding equations of state for a coupling of $\lambda = \pm 2$ and ± 4 are shown in Figs. 6.5 and 6.6, respectively. The insets (where available) show zooms into the region of positive $\beta\mu$, where quantum effects dominate. We compare the CL results with third-order perturbation theory, imaginary-polarization calculations (for the attractive case where iHMC is available), and the third-order viral expansion in the region $\beta\mu \leq -1.5$ (for $|\lambda| = 1$ and 2).

In the case of the smallest coupling of $\lambda = \pm 1$, the agreement between the methods is remarkable, in particular in the viral region (for both attractively- and repulsively-interacting regimes), where except for very small deviations in the perturbative third-order answer, the results are almost indistinguishable from one another. Note that, although the virial coefficients b_2 and b_3 used here vary considerably with the interaction strength, the lowest-order dominant term at large negative $\beta\mu$ is interaction independent. All of the methods shown here, including CL, reproduce that universal asymptotic behavior. The insets in Fig. 6.4 show for $\beta\mu > 1$ the agreement of the CL results with the perturbative and iHMC calculations.

As the coupling is increased to a moderate value of $\lambda = \pm 2$, the agreement between all three techniques begins to deteriorate when compared to $\lambda = \pm 1$, although the overall comparison is satisfactory. Perturbation theory at third order is expected to begin breaking down at this interaction strength, as shown in Ref. [112]. The virial expansion also demonstrates deterioration at this coupling as both $\beta\mu$ and βh move away from $z_s \sim 0$. We show our results for the density equation of state at $\lambda = 2$ (top) and $\lambda = -2$ (bottom) in Fig. 6.5.

Finally, in order to demonstrate that CL is capable of providing a prediction of the equation of state in a non-perturbative regime (at least up to N3LO), we strengthen the coupling to $\lambda = \pm 4$. The density at this coupling strength for attractive (top) and repulsive (bottom) regimes is shown in Fig. 6.6. As expected, PT breaks down significantly when compared to CL at this interaction strength. However, it is reassuring to note that CL reproduces the unpolarized result for attractive interactions (where the HMC technique is available) to within acceptable accuracy. Note that at the fixed value of $\beta = 8$, finite beta effects (resulting from the finite temporal lattice size) are expected to be more prevalent when compared to the more weakly-coupled counterparts (see Ref. [1] for quantitative details).

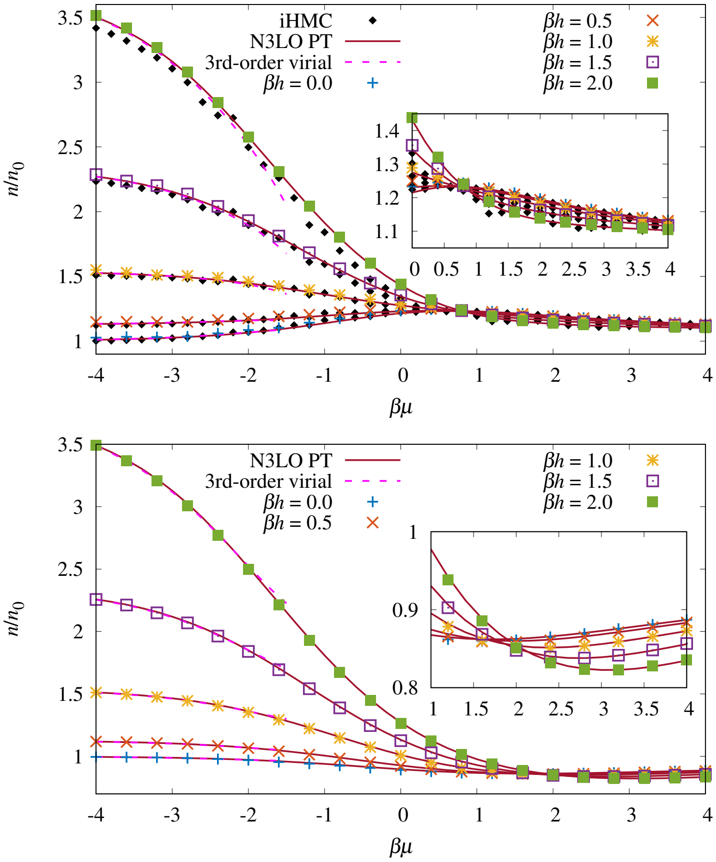

Figure 6.4: Density equation of state $n = n_\uparrow + n_\downarrow$ normalized by the non-interacting, unpolarized counterpart n_0, for attractive (top) and repulsive (bottom) interactions of strength $\lambda = \pm 1$. *Insets:* Zoom in on region $\beta\mu > 0$ (top) and $\beta\mu > 1$ (bottom). In all cases, the CL results are shown with colored symbols, iHMC results (from Ref. [2]) appear with black diamonds, perturbative results at third order are shown with solid lines, and virial expansion results appear as dashed lines.

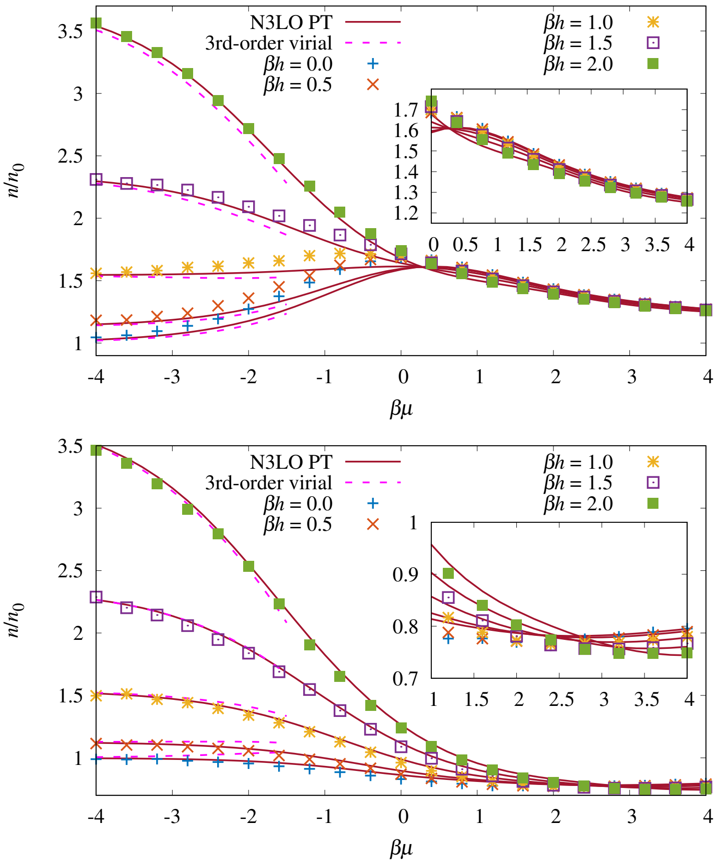

Figure 6.5: Density equation of state $n = n_\uparrow + n_\downarrow$ normalized by the non-interacting, unpolarized counterpart n_0 for attractive (top) and repulsive (bottom) interactions of strength $\lambda = \pm 2$. *Insets:* Zoom in on region $\beta\mu > 0$ (top) and $\beta\mu > 1$ (bottom). The CL results are shown with colored symbols, perturbative results at third order are shown with solid lines, and virial expansion results appear as dashed lines.

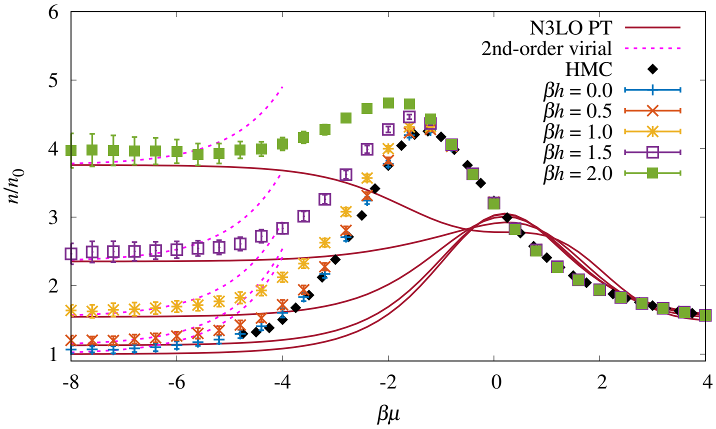

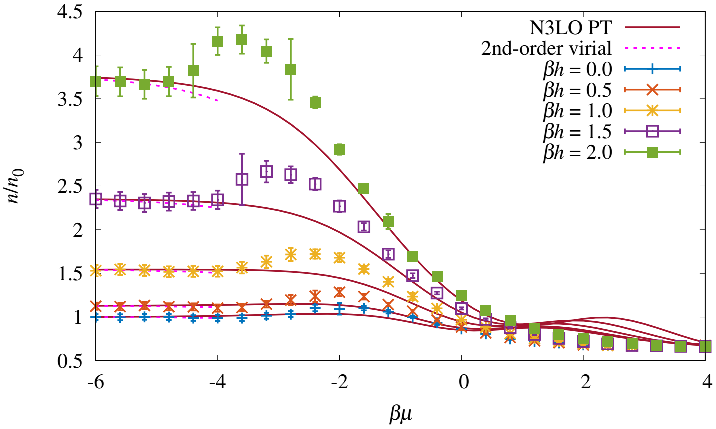

Figure 6.6: Density equation of state $n = n_\uparrow + n_\downarrow$ normalized by the non-interacting, unpolarized counterpart n_0 for attractive (top) and repulsive (bottom) interactions of strength $\lambda = \pm 4$. The CL results are shown with colored symbols, perturbative results are shown with solid red lines, and HMC for the attractive, unpolarized case is shown in black diamonds [1].

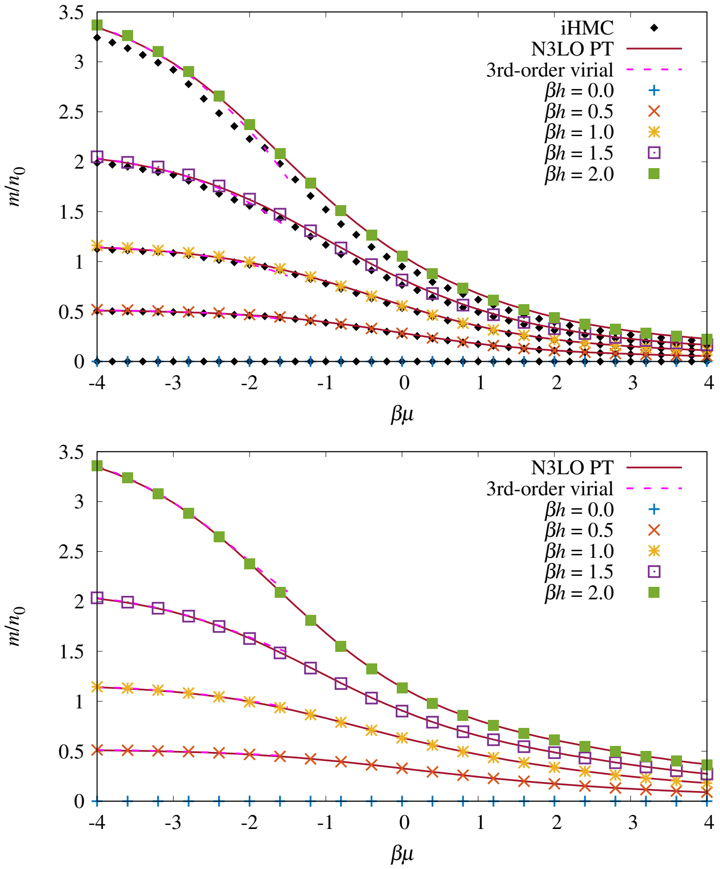

Figure 6.7: Spin polarization $m = n_\uparrow - n_\downarrow$ normalized by the non-interacting, unpolarized counterpart n_0 for attractive (top) and repulsive (bottom) interactions of strength $\lambda = \pm 1$. The CL results are shown with colored symbols, iHMC results (from Ref. [2]) appear with black diamonds, perturbative results at third order are shown with solid lines, and virial expansion results appear as dashed lines.

6.3.3: Polarization equation of state

In addition to the density equation of state, we also provide the spin polarization (sometimes also referred to as the magnetization) equation of state for all of the couplings mentioned in the previous section. Again, we can compare the CL results with third-order PT, imaginary-polarization calculations (in the attractive case), and the third-order virial expansion in the region $\beta\mu \leq -1.5$. Agreement is satisfactory among all of these techniques within the regions we study here. When contrasted with the density, it is interesting to note that the polarization is approximately (but not precisely) insensitive to the coupling strength. The results for these calculations are shown in Figs. 6.7, 6.8, and 6.9 for attractive (top) and repulsive (bottom) coupling strengths of $|\lambda| = 1$, 2, and 4, respectively.

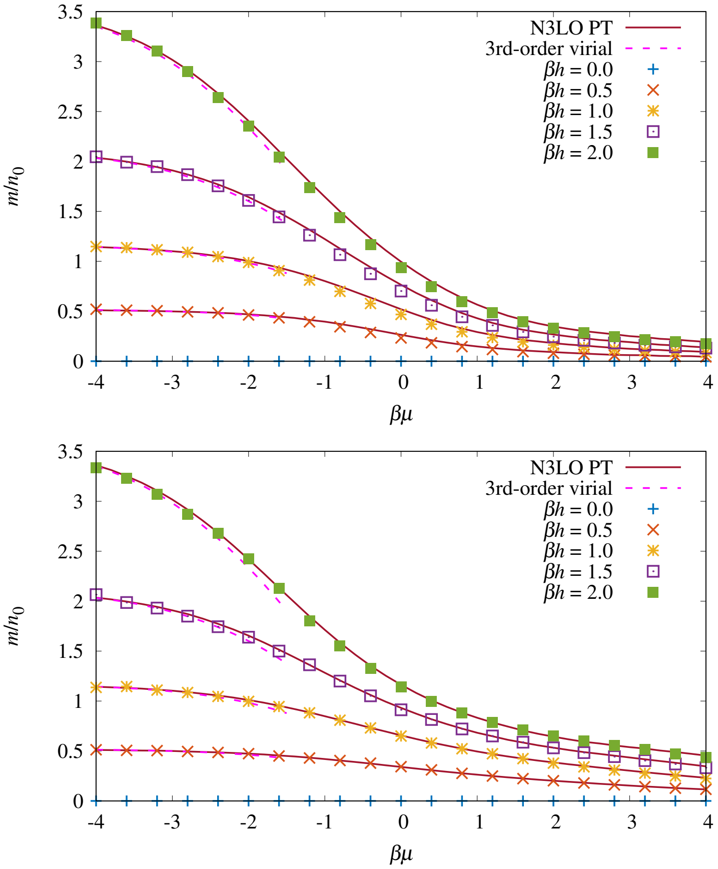

Figure 6.8: Spin polarization $m = n_\uparrow - n_\downarrow$ normalized by the non-interacting, unpolarized counterpart n_0 for attractive (top) and repulsive (bottom) interactions of strength $\lambda = \pm 2$. The CL results are shown with colored symbols, perturbative results at third order are shown with solid lines, and virial expansion results appear as dashed lines.

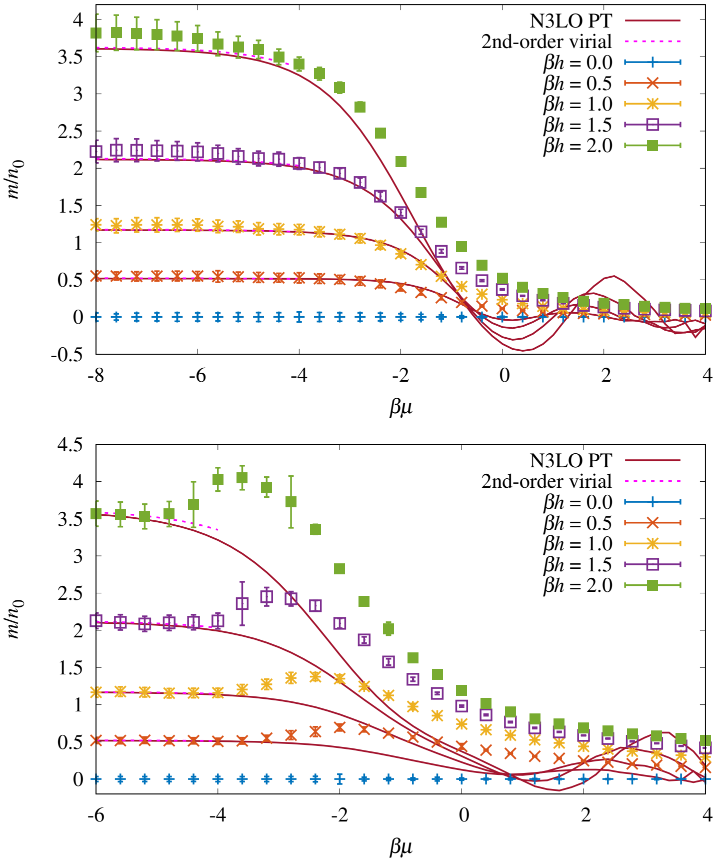

Figure 6.9: Spin polarization $m = n_\uparrow - n_\downarrow$ normalized by the non-interacting, unpolarized counterpart n_0 for attractive (top) and repulsive (bottom) interactions of strength $\lambda = \pm 4$. The CL results are shown with colored symbols, perturbative results at third order are shown with solid lines, and virial expansion results appear as dashed lines.

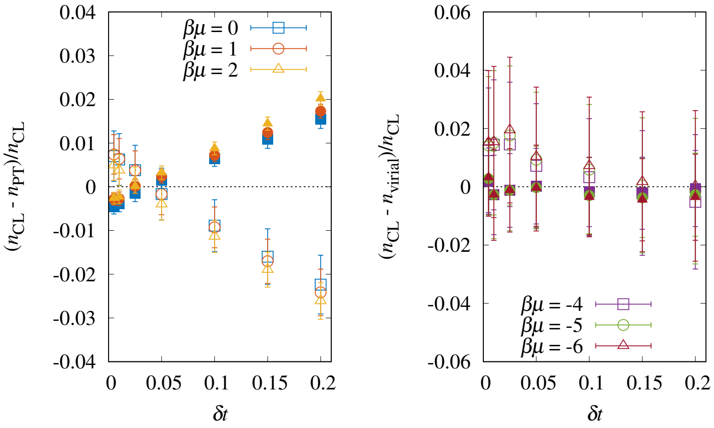

Figure 6.10: *Left:* Relative difference between the density $n_\uparrow + n_\downarrow$ computed via CL ($n_{\rm CL}$) and the third-order perturbative result $n_{\rm PT}$ for three positive values of $\beta\mu$, as a function of the CL timestep $t_{\rm CL}$. The dashed horizontal line shows where $n_{\rm CL} = n_{\rm PT}$. *Right:* Relative difference between $n_{\rm CL}$ and the third-order virial expansion $n_{\rm virial}$ for three values of $\beta\mu$ of small fugacity, as a function of $t_{\rm CL}$. The dashed horizontal line shows where $n_{\rm CL} = n_{\rm virial}$. In both plots, the coupling was set to $\lambda = \pm 1$, where solid and open symbols refer to repulsive and attractive couplings, respectively. Error bars represent the statistical error of the CL calculation, and indicate agreement with PT and the virial expansion as $t_{\rm CL} \to 0$.

6.3.4: Systematics of Langevin time discretization

One of the features of the Langevin method is that, in either its real or complex forms, it performs a walk in configuration space for a fictitious time t which is discretized with a finite timestep δt. Even when using adaptive integrators, as was done throughout this chapter, the tolerance of the adaptive algorithm effectively determines a scale for δt which affects the results. We have observed effects where if the tolerance is set such that it corresponds to an average time step which is too large, the CL evolution will converge to a value which systematically deviates from the true result.

To illustrate these effects, we show in Fig. 6.10 a plot of the sensitivity in the density to the size of the CL time step δt for $|\lambda| = 1$ using the perturbative answer for $\beta\mu \geq 0$ and the answer from the virial expansion for $\beta\mu \leq -4.0$ as a reference. These sensitivities are compared for three representative values of the chemical potential at $\beta h = 2$. As is evident from that figure, the size of δt can be responsible for potential discrepancies. The remaining difference between the CL and perturbative results in the limit $\delta t \to 0$ is ascribed in part to the inaccuracy of N3LO PT, and in part to statistical uncertainties, as shown by the error bars. On the scale of the insets of Figs. 6.4 and 6.5, however, that remaining difference would appear as agreement between CL and PT. This highlights the need to explore such systematic effects when using the CL method.

Section 6.4: Reducing the sign problem with convolutional neural networks

As a sharp departure from the techniques presented so far to overcome the sign problem, we will now introduce a first exploration in using convolutional neural networks (CNNs) to reduce the impact of a low signal-to-noise when stochastically estimating a thermodynamic observable. In particular, we will use the CNN to identify the field configurations which lie close to the true expectation value, such that the standard deviation of the sample population is significantly reduced. When combined with a quantum Monte Carlo algorithm, such as CL, the CNN has the potential to increase the overall efficiency of the simulation. Specifically, we would like to apply the CNN to address regimes where MC techniques have greater difficulty, in particular the virial region where the probability measure flattens. In a sense, we would like to be able to more intelligently transfer knowledge of the deep quantum regime over to the virial region; at present, MC simulations at different points of $\beta\mu$ and λ are independent of one another, and perhaps this may not be the most efficient approach. Machine learning and neural networks have been making an increasing number of appearances in the quantum many-body literature, most notably in estimating phase transition boundaries [141–145], approximating ground-state energies [146, 147], and in other areas as well.

Deep learning has drastically changed the ways in which modern algorithms draw inferences from large and complex datasets and generalize to new situations. Although the ideas of neural networks have existed for decades, it is only relatively recently that technology has gained the computational capacity to train large neural networks. The details of how networks are designed, and their vast array of applications are very interesting and quickly evolving, but outside the scope of this dissertation; as such we point the reader to Ref. [148] as an excellent reference to the details of deep learning.

The CNN used in this example contains both sequentially-connected convolutional and dense layers, with no recurrent steps. A diagram of the network architecture used is shown in Fig. 6.11, and indicates types of layers used (including kernel sizes, number of filters, and number of neurons), as well as activations applied. A normalized form of the fermion matrix $\mathcal{U}[\sigma]$ is used as an input to the convolutional portion (recall that $\mathcal{U} = (M - 1)/z$, where M is the $N_x \times N_x$ fermion matrix and z is the fugacity). For the purposes of this demonstration, a smaller volume of $N_x = 31$ and $N_\tau = 60$ for $\beta = 6$ in one spatial dimension was used, but the expectation is that the same techniques should apply to larger volumes (but would require an appropriately larger number of convolutional layers). In particular, we take the difference with the kinetic

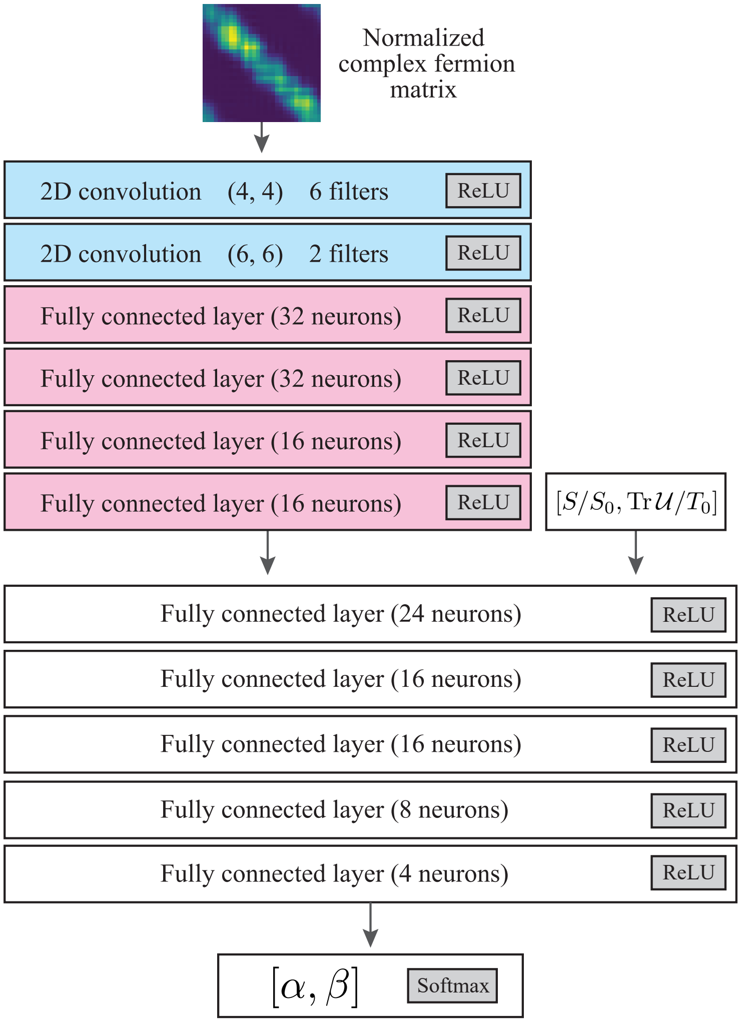
Normalized complex fermion matrix
2D convolution (4, 4) 6 filters ReLU
2D convolution (6, 6) 2 filters ReLU
Fully connected layer (32 neurons) ReLU
Fully connected layer (32 neurons) ReLU
Fully connected layer (16 neurons) ReLU
Fully connected layer (16 neurons) ReLU
$[S/S_0, \mathrm{Tr}\,\mathcal{U}/T_0]$
Fully connected layer (24 neurons) ReLU
Fully connected layer (16 neurons) ReLU
Fully connected layer (16 neurons) ReLU
Fully connected layer (8 neurons) ReLU
Fully connected layer (4 neurons) ReLU
$[\alpha, \beta]$ Softmax

Figure 6.11: Architecture of the convolutional neural network. The complex, normalized form of the fermion matrix is inserted as the input of the convolutional network. Additional information is passed in at an intermediate step through the sequential network, and two output neurons categorize the accuracy of the considered auxiliary field configuration (see main text).

energy operator at $\mu = 0$ in coordinate space:

$$\tilde{\mathcal{U}}[\sigma] = \mathcal{U}[\sigma] - T_x \quad , \quad [T_p]_{p,p'} = \sum_n \exp\left[\frac{-\beta}{2}\left(\frac{2\pi n}{N_x}\right)^2\right]\delta_{p,p'}, \tag{6.25}$$

where T_x is the Fourier transform of T_p, the representation in momentum space. We choose to set $\mu = 0$ considering that the matrix $\mathcal{U}[\sigma]$ is independent of the chemical potential. This abstraction can allow the neural network to make generalizations across all values of μ. The matrix $\mathcal{U}[\sigma]$ (where the real and imaginary parts are treated as two channels) is passed through two convolutional layers which contain several trainable filters, after which the output of the second layer is flattened into a one-dimensional vector and passed through several fully-connected layers for global processing. At this point, additional information (referred to as the auxiliary vector below) about the field configuration is introduced into the network, including the value of the fermion determinant S/S_0 and the trace of $\mathcal{U}[\sigma]$, $\mathrm{Tr}\,\mathcal{U}/T_0$, both of which are normalized by a non-interacting counterpart. Here, we define S_0 and T_0 such that

$$S_0 = 2\sum_k \ln\left(1 + ze^{-\beta p_k^2/2}\right), \tag{6.26}$$

$$T_0 = \sum_k e^{-\beta p_k^2/2}, \tag{6.27}$$

where $p_k = 2\pi k/N_x$ and the sum is over the spatial lattice from $k = -N_x/2$ to $N_x/2 - 1$. The combined vector containing the result from the convolution and the auxiliary vector is passed through additional fully-connected layers and finally through two output neurons with a softmax activation, both of which categorizes the input fermion matrix (and corresponding auxiliary field). Note that all other layers in the network have a rectified linear unit (ReLU) activation, which introduces the requisite nonlinearity into the network. Training is performed for 200 epochs using the Adam [149] optimizer with a cross-entropy loss function. The network was implemented using the software packages Keras and TensorFlow.

The network is trained such that if the output vector is approximately [0, 1] (or if the output of the second neuron is similarly maximal), the trained observable (here, the density n/n_0) as calculated from the input fermion matrix is estimated to be within 10% of the true expectation value. Conversely, if the first neuron is maximized, the corresponding field configuration is estimated to provide a sample for the observable which is above 10% in error. The training data used consists of 452,000 samples gathered from 226 independent CL simulations corresponding to $\beta\mu = -2.4$ to 5 and $\lambda = \pm 0.75$ to ± 2 (corresponding to both attractive and repulsive interactions). An additional 60,000 samples from the virial regime where $-5.0 \leq \beta\mu \leq -3.0$ and $0.25 \leq |\lambda| \leq 2.0$ were withheld from the training set as validation data, which was used to determine the accuracy of the trained model. Data from N3LO perturbation theory at a matching lattice size was used as the reference value to determine the relative error of each field configuration, which is known to be acceptably accurate within the regime studied here, particularly at $\lambda = \pm 1$. In practice, one should use a nonperturbative result from CL, but available computational resources to obtain well-converged results, particularly in the deep virial region, was a limiting factor for this first exploration. A smaller study using CL results indicated that the CNN was able to appropriately learn the features of whatever reference value the network is trained on.

A number of plots demonstrating the performance and predictions of the trained CNN model for $\lambda = \pm 1$ is shown in Fig. 6.12. The top plots show the mean values of the density equation of state n/n_0 as conventionally determined by the CL simulation (containing 10,000 samples), in addition to the mean value of the subset of samples which the CNN estimates to be within 10% of the true expectation value. The red and blue shaded regions show the standard deviation of the full set and subset selected by the CNN, respectively. The shaded grey background of all plots throughout the figure where $\beta\mu > -2.4$ indicates the data points at $\lambda = \pm 1$ that were used to train the CNN; the data points for $\beta\mu < -2.4$ are a prediction made by the CNN on field configurations not previously seen. Even though the predictions made by CL and the CNN are very close to one another, the CNN is often able to make a slightly improved result. The key advantage offered by the CNN, as indicated by this first exploratory study, is that the variance of the sample set is significantly reduced, which can offer a drastic improvement in other situations where the sign problem is too severe and too computationally expensive to overcome.

The center plots show the percentage of samples which were correctly classified by the CNN. Even though the network struggles near the density peak, particularly in the attractive case, the accuracy always remains above 90%. The network is still able to provide an accurate mean for the density considering that an average is taken over many inferences. The bottom plots indicate the fraction of samples collected by the CL simulation whose difference from the true expectation value is $\leq 10\%$. This demonstrates that CL becomes much less efficient in the virial region where the probability measure flattens and becomes approximately independent of the auxiliary field as $z \rightarrow 0$. Considering that a smaller percentage of samples in the virial region are classified as close to the reference value, yet the network's accuracy is above 96%, indicates that the CNN is learning nontrivial features of the fermion matrix and of the relevant quantum dynamics.

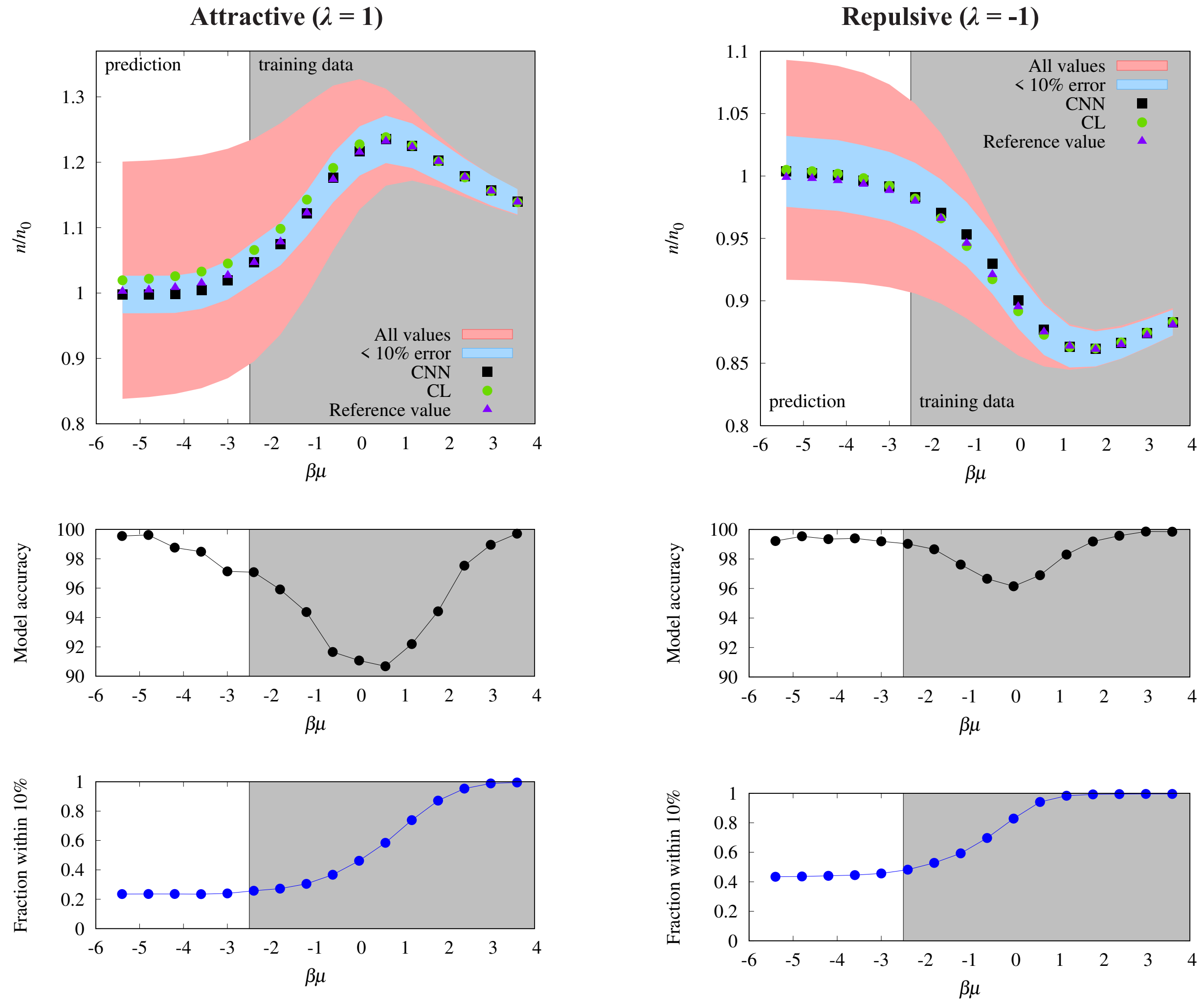

Figure 6.12: Predictions and performance of the trained convolutional neural network shown in Fig. 6.11. The plots on the left hand side corresponds to the case of attractive interactions where $\lambda = 1$, and the right corresponds to repulsive interactions where $\lambda = -1$. *Top:* Density n normalized by the non-interacting counterpart n_0. Values of the density made by the CNN prediction (black squares), CL simulations (green circles), and N3LO reference values (purple triangles) are shown. The red shaded curve indicates the standard deviation of all samples provided by CL, and the blue shaded curve shows the standard deviation of the subset of samples selected by the CNN whose error is estimated to be $\leq 10\%$. *Center:* Percentage of the samples across the training and validation data sets which were correctly classified by the CNN for each value of $\beta\mu$. *Bottom:* Fraction of the density samples whose error is $\leq 10\%$ for each value of $\beta\mu$. In all plots, the grey shaded region indicates the values of $\beta\mu$ whose samples were used to train the CNN.

Therefore, it is likely to be a promising approach to more challenging situations for conventional Monte Carlo techniques.

CHAPTER 7: Systems in Higher Dimensions

In the previous chapters of this dissertation, we explored equations of state of unpolarized and spin-polarized Fermi gases in one spatial dimension using a variety of numerical and analytic techniques. All of this prior work has been building up to the point where we are capable of moving beyond these models in low dimensions. We will now gather the expertise we gained by exploring the one-dimensional counterpart in detail, and apply those methods to systems in two and three spatial dimensions. As is to be expected, these calculations are significantly more challenging, primarily due to the computational resources required. However, the payoff may be rewarding – these systems can be much richer since phase transitions occur, and are experimentally relevant in modern research. In particular, the unitary Fermi gas in three dimensions[1], where the two-body interaction strength is tuned to the threshold of bound state formation, has been of particular theoretical and experimental interest for the past decade.

Section 7.1: Spin-polarized fermions in two spatial dimensions

The quantum gas in two spatial dimensions (2D) is a unique character, and is quite different from the one- and three-dimensional cases. The difference arises from the fact that the 2D system contains an anomalous scale invariance, where the classical interpretation of the Hamiltonian contains symmetries which are broken by quantum mechanical effects. In particular, the bare coupling g in the non-relativistic 2D Hamiltonian with contact interactions is dimensionless, and appears to be scale invariant until a two-body bound state is immediately formed after an interaction is turned on. As such, this and other quantum anomalies related to scale invariance has been a subject of interest for decades [151–156]. The natural dimensionless scale that sets the interaction strength here is therefore $\beta\epsilon_B$, where β is the inverse temperature and ϵ_B is the ground-state two-body binding energy. Unfortunately, the two-dimensional form of the Hamiltonian [see Eq. (3.1)] is still written in terms of the bare coupling g. This means that a renormalization procedure must be done to determine the mapping of $\epsilon_B(g, \beta)$.

This intermediary of mapping the theory to the interactions of the physical system introduces an additional complication to the study of two-dimensional gases. By performing a numerical calculation of the function $g(\epsilon_B, \beta, N_x)$, one finds that this coupling runs logarithmically with parameters of the finite system (e.g. N_x and β) and will generally not converge when taking the continuum limit. Therefore, observables should generally be computed via an extrapolation in N_x and β at fixed ϵ_B. To determine $g(\epsilon_B, \beta, N_x)$, the two-body ground state energy is calculated numerically on the lattice using a Green's function projection method (see e.g. [157] for related work to this method). In this case a trial wavefunction $|\psi_0\rangle$ is constructed using the Slater determinant of plane wave solutions, and is then evolved according to

---

[1] This chapter is based in part on the work published in Ref. [114, 150]. Fig. 7.4 as it appears in Ref. [114] is published by EDP Sciences under the Creative Commons Attribution License 4.0.

$$|\psi_\beta\rangle = \exp(-\beta\hat{H})|\psi_0\rangle \tag{7.1}$$

in the limit of $\beta \to \infty$. The Hamiltonian in the evolution operator is the usual non-relativistic dispersion with a contact interaction controlled by the bare coupling g. The corresponding binding energy E_0 is given by the exponential decay of the energy as a function of β:

$$E_\beta = E_0 + Ae^{-\beta(E_1 - E_0)} + \cdots \tag{7.2}$$

where E_1 denotes the first excited state. These measurements for varying values of g gives a parametric function which can therefore be used to determine the mapping of $g(\epsilon_B)$ across relevant values of N_x and β.

A full extrapolation of the spin-polarized equation of state for this Hamiltonian in 2D to the continuum limit is still underway, but we will present results for this calculation for a choice of N_x and β and see how it compares to perturbation theory and experiments in the unpolarized limit. The density and polarization equations of state of the spin-polarized 2D system may be computed under complex Langevin with the appropriate straightforward modifications; we focus here on the density for attractively interacting fermions.

Fig. 7.1 shows the density n/n_0 for the unpolarized system corresponding to five values of $\beta\epsilon_B$ across a handful of techniques including CL (for $N_x = 16$) and a previous calculation [3] using HMC ($N_x = 19$). Although the curves agree satisfactorily for the smallest coupling strengths, the deviations which appear at increasing interaction strengths indicate the finite-volume effects which are still present at these computationally-demanding lattice sizes. This underscores our desire for performing an accurate extrapolation to the infinite volume limit. However, the comparison between the CL and HMC datasets indicate that CL continues to perform as expected as was observed in one spatial dimension. Note that other simulation

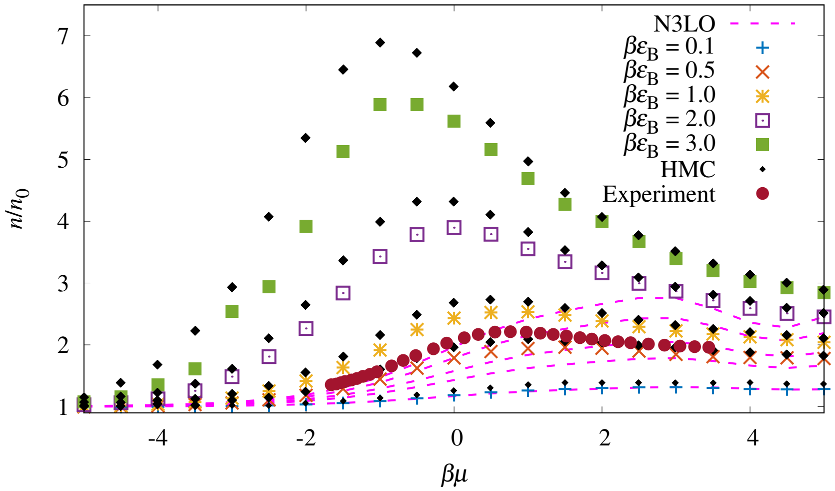

Figure 7.1: Density equation of state n normalized by the non-interacting counterpart n_0 for the spin-balanced attractively interacting Fermi gas in two spatial dimensions as a function of the dimensionless chemical potential $\beta\mu$. Curves are displayed for five interaction strengths from $\beta\epsilon_B = 0.1$ to 3.0. Colored symbols correspond to CL calculations at $N_x = 16$, and black diamonds correspond to HMC calculations [3] at $N_x = 19$, where both are at $\beta = 10$. PT at N3LO (pink dotted lines) are shown at each value of the chemical potential asymmetry, which correspond to that of the CL data points from bottom to top.

parameters, including the imaginary time discretization $\tau = 0.05$ and the regulation parameter $\xi = 0.1$ remain the same here as from our 1D explorations. A result from an experimental study of 2D ultracold atomic gases [49] is also shown for $\beta\epsilon_B \simeq 0.5$. Although the agreement between these experimental and theoretical data seems qualitatively correct, minor deviations which are likely due to finite volume effects can be seen near the peak of this curve. Indeed, as one moves from the $N_x = 16$ to 19 data, one approaches this experimental result, which can be expected to lie in the continuum limit. Finally, perturbation theory up to N3LO for the unpolarized gas (which is less computationally demanding than the polarized counterpart) is also displayed. However, the result only agrees well with the smallest coupling strength, and highlights the highly nonperturbative nature of the 2D system, where the radius of convergence of PT may be drastically smaller when compared to 1D. This behavior may be attributed to the logarithmic divergence of the bare coupling, which is essentially the expansion parameter used in PT here. Note that a comparison with the virial expansion is not displayed in this plot, but the coefficients up to third order in the continuum have been determined [158, 159], and a comparison of the HMC data with other analytic approaches are displayed and discussed in Ref. [3].

Two examples of the density equation of state for the spin-polarized system are shown in Fig. 7.2, where the top and bottom plots correspond to a coupling of $\beta\epsilon_B = 0.1$ and 0.5, respectively. The data points correspond to calculations performed using CL with a lattice size of $N_x = 16$ and where $\beta = 10$. Note that the non-zero chemical potential asymmetry introduces a sign problem, which prohibits the use of HMC. Perturbation theory results are shown at N2LO for where $\beta h \neq 0$, and at N3LO where $\beta h = 0$; note that the values of βh correspond to those of the CL data points from bottom to top. The perturbative results at both second- and third-order agree well at $\beta\epsilon_B = 0.1$, but show significant breakdown at the increased coupling strength of $\beta\epsilon_B = 0.5$.

Section 7.2: The polarized Fermi gas at unitarity

One of the most intensely studied physical systems in recent years, at the interface of atomic, nuclear, and high-energy physics, is the unitary Fermi gas (UFG) [68, 160, 161]. This system refers to a two-component Fermi gas in three spatial dimensions where the s-wave scattering length a_0 is tuned to be infinite and the interaction range r_0 is effectively zero. As such, the system can be modeled with a Hamiltonian which contains a contact interaction tuned to the appropriate value of the bare coupling g, i.e. the three-dimensional analogue of the Gaudin-Yang model. Additionally, the lack of scales typically set by the scattering length and interaction range results in a equation of state for the unitary Fermi gas which is universal, in the sense that it can be characterized solely by the density (or alternatively, the dimensionless Fermi momentum $k_F a_0$; $k_F = (3\pi^2 n)^{-1/3}$) [162]. This property renders this model of the UFG relevant across vast energy scales, from atomic physics to astrophysics (including approximately, the crusts of neutron stars [163–169]). Since this system has importance across an intersection of multiple fields, it has been experimentally explored in a variety of contexts [170, 171]. In particular, a unitary Fermi gas can be realized to an excellent approximation using ultracold alkali atoms in optical traps and manipulated via a Feshbach resonance [4].

By studying a strongly-interacting system in three spatial dimensions, we enter a regime where we may encounter superfluid phase transitions at sufficiently low temperatures. In particular, the UFG lies at a point between the Bardeen-Cooper-Schrieffer (BCS) and Bose-Einstein condensation (BEC) phases, for which the details of the crossover in the unpolarized case has been extensively studied [161], yet the crossover along spin-polarized plane remains unknown (although a few studies have been made, see e.g. Refs. [172–174]). The BCS phase is a weakly-interacting limit where large-volume Cooper pairs are formed, and the BEC phase is a strongly-interacting limit consisting of tightly-bound dimers [175]. However, it is expected that a superfluid system will lose its superfluidity at a sufficiently high spin polarization [176, 177]. An understanding of how this BEC-BCS crossover occurs, and its relation to the UFG, can have important implications beyond atomic superfluids, including high-T_c and color superconductors [172, 178–182]. Note

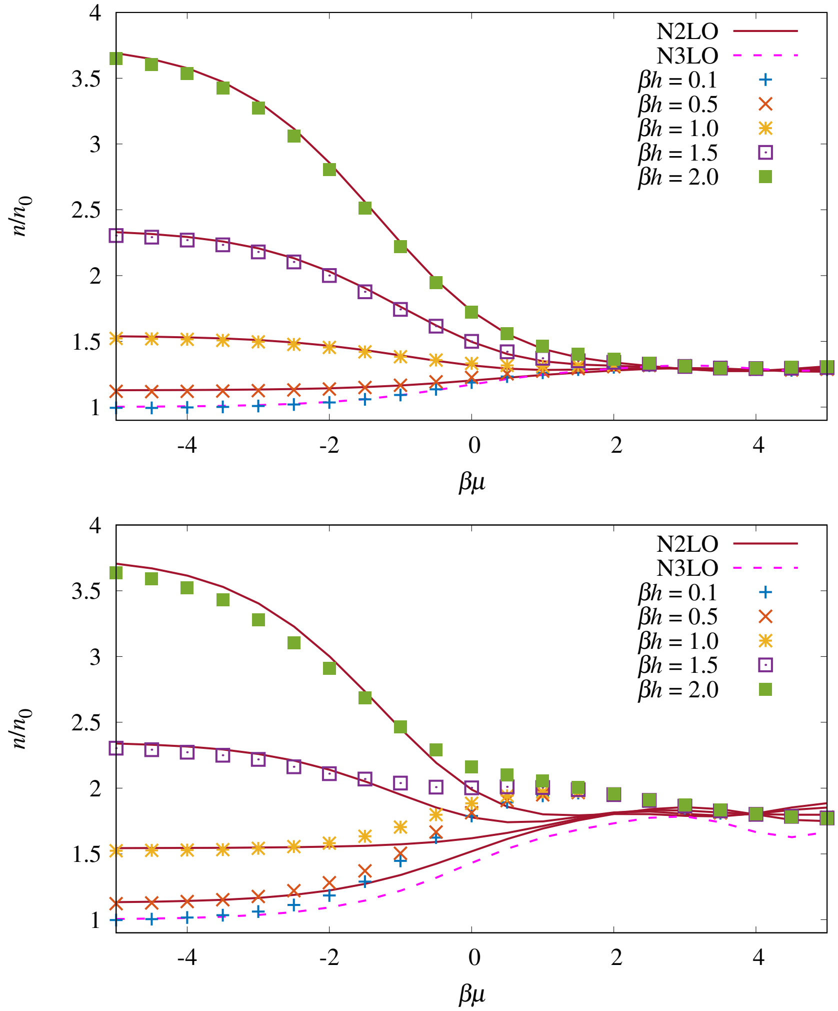

Figure 7.2: Density equation of state n normalized by the non-interacting counterpart n_0 for the spin-polarized attractively interacting Fermi gas in two spatial dimensions as a function of the dimensionless chemical potential $\beta\mu$. Curves are displayed for five polarizations from $\beta h = 0.0$ to 2.0. Colored symbols correspond to CL calculations at $\beta\epsilon_B = 0.1$ (top) and $\beta\epsilon_B = 0.5$ (bottom) for $N_x = 16$ and $\beta = 10$. PT at N2LO (red solid lines) is shown for the polarized case, and at N3LO (pink dotted line) for the spin-balanced case. Note that the values of βh for each of the PT curves correspond to that of the CL data points from bottom to top.

that in comparison with the 2D model of the previous section, the relevant phase transition there is instead the Berezinskii-Kosterlitz-Thouless type [68].

As the UFG is a strongly-coupled many body system, it is highly non-perturbative and exhibits a severe sign problem in the polarized case. Just as in the one-dimensional counterpart, the fermion determinants corresponding to the two-particle species are unequal (since $\mu_\uparrow \neq \mu_\downarrow$) and may generally differ in both sign and magnitude from one another. One may suggest the route of introducing an imaginary chemical potential asymmetry and perform an analytic continuation, as was done in Chapter 4 for the 1D case, but one will very likely find that this method becomes intractable in such a strongly coupled system. Indeed, it was determined that even in one dimension the method of analytic continuation shows significant breakdown as the coupling strength increases. As we will show below, the complex Langevin method, as it was introduced in the previous chapter, performs much better at attacking this problem.

Recall that the complex Langevin method complexifies the auxiliary field $\sigma \to \sigma_R + i\sigma_I$ such that the path integral representation of the grand-canonical partition function is

$$\mathcal{Z} = \int \mathcal{D}\sigma \, e^{-S[\sigma]} \tag{7.3}$$

where the action $S[\sigma] = -\ln\left[\det(M_\uparrow[\sigma])\det(M_\downarrow[\sigma])\right]$ and M_s is once again the fermion matrix for spin s; see Chapter 5 or Ref. [115] on details of how this matrix is constructed. The Hamiltonian that is studied here is again a non-relativistic dispersion with a contact interaction, but now in three spatial dimensions. The bare coupling g is fixed throughout this calculation such that in the unitary limit [see the discussion of Eq. (2.21)]

$$p \cot\delta(p) = 0 \tag{7.4}$$

to zeroth order in p, which corresponds to $g \approx 5.14$. Also note that M is also a function of the fugacity z_s, such that in the spin-polarized case where $\mu_\uparrow \neq \mu_\downarrow$ and it is no longer the case that $e^{-S[\sigma]} \geq 0$, it is also generally true $\det(M_\uparrow[\sigma]) \neq \det(M_\downarrow[\sigma])$. Therefore, in the spin-polarized regime $S[\sigma]$ can also generally be complex, which introduces a sign problem and hinders the use of probabilistic MC approaches. The same is the case in one spatial dimension; however here, we have the additional complexity that the spacetime volume of the system is now $V = N_x^3 \times N_\tau$ (the fermion matrix has $V \times V$ elements) where to reach the continuum limit $\ell = 1 \ll \lambda_T, \lambda_F \ll N_x$ must still be satisfied (where λ_F is the Fermi wavelength, and the Fermi momentum in 3D is $k_F = (3\pi^2 n)^{1/3}$). In other words, the calculation must be performed in a way such that N_x and β are made as large as possible, while still remaining in a dilute regime to avoid lattice artifacts due to finite range. Therefore, the computational challenge to compute the equation of state is great, and requires months of execution time for up to $N_x = 11$.

To characterize the universal thermodynamics of the spin-polarized UFG, we have computed the density n, magnetization m and normalized susceptibility $\bar{\chi}_M$ as function of the dimensionless chemical potential $\beta\mu$ and chemical potential asymmetry βh, where

$$\mu = \frac{\mu_\uparrow + \mu_\downarrow}{2} \quad , \quad h = \frac{\mu_\uparrow - \mu_\downarrow}{2}. \tag{7.5}$$

As usual, the path integral form of $\langle n \rangle$ and $\langle m \rangle$ is obtained by differentiating $\ln \mathcal{Z}$ with respect to μ and h, respectively. The magnetic susceptibility is derived from the magnetic equation of state, where

$$\bar{\chi}_M = \frac{\partial \bar{m}}{\partial(\beta h)} \quad , \quad \bar{m} = \frac{m}{n}\bigg|_{\beta h = 0}. \tag{7.6}$$

Computations have been performed [150] at $N_x = 7$, 9 and 11 with $N_\tau = 160$ (corresponding to $\beta = 8$ and $d\tau = 0.05$) using the complex Langevin method. As usual, periodic boundary conditions are used in the spatial direction and antiperiodic in the temporal direction to respect the fermion fields. In this study, the chemical potential asymmetry parameter was varied over the range $\beta h \in [0.0, 2.0]$ and the mean chemical potential was in the interval $\beta\mu \in [-3.0, 2.5]$ which covers the semiclassical regime to the deep quantum regime, including a small region below the superfluid transition temperature of the unpolarized system at $(\beta\mu)_c \simeq 2.5$ [4, 183–185]. We compare with experimental results in the unpolarized limit obtained at MIT and the second- or third-order virial expansion [see Eqs. (6.23) and (6.24)], where note that in 3D for the single-particle partition function of two spins in the continuum, $Q_1/V \to 2/\lambda_T^3$, and the non-interacting virial coefficients are $b_n^{(0)} = (-1)^n\, n^{-5/2}$. The coefficients of the interacting gas at unitarity up to third-order are $b_2 = 3/(4\sqrt{2})$ and $b_3 \approx -0.29095$ (see, e.g., Refs. [81, 186]). Studies of the unpolarized unitary Fermi gas were first conducted experimentally in Ref. [53, 54] and calculated with QMC in Ref. [106].

We first validate results of the CL calculation for the unpolarized case against prior bold diagrammatic [5] and determinantal hybrid Monte Carlo [6] calculations for the density, which is shown in Fig. 7.3 (top). For

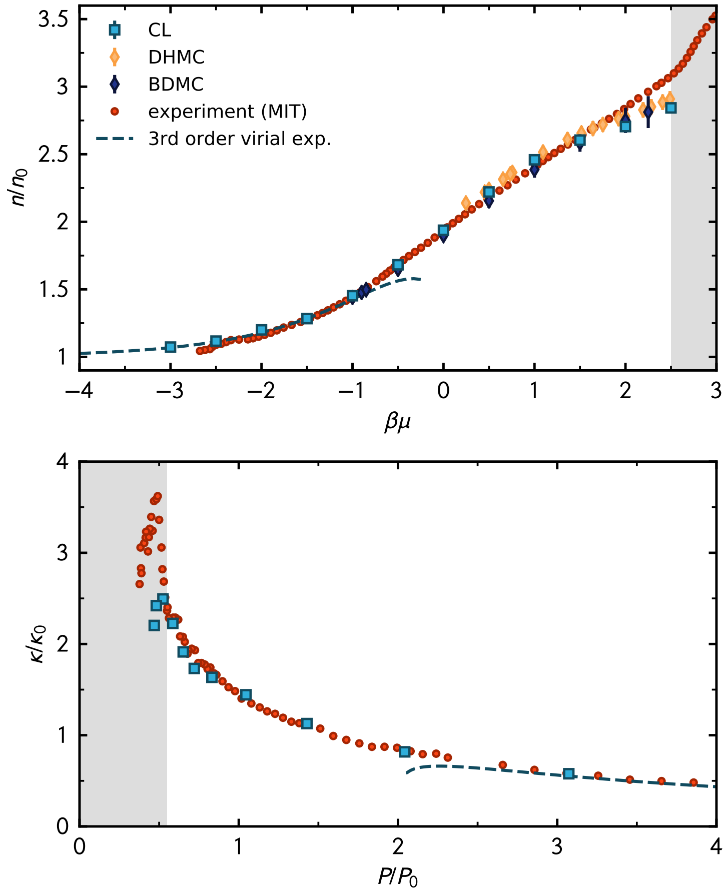

Figure 7.3: *Top:* Density of the unpolarized UFG obtained with CL (blue squares), in units of the noninteracting, unpolarized density n_0 as a function of the dimensionless mean chemical potential $\beta\mu$. Also shown is the third-order virial expansion (dashed line), experimental results of Refs. [4, 5] (red circles), bold diagrammatic Monte Carlo (BDMC) calculations [5] (dark diamonds), and determinantal hybrid Monte Carlo (DHMC) calculations [6] (light diamonds). *Bottom:* Compressibility κ as derived from the density EOS, in units of its noninteracting counterpart κ_0 as a function of the dimensionless pressure P/P_0 (blue squares). A comparison is made to experimental values [4] (red circles) and the third-order virial expansion (dashed line). Statistical uncertainties for the CL results are on the order of the symbol sizes. The shaded areas indicate the superfluid phase.

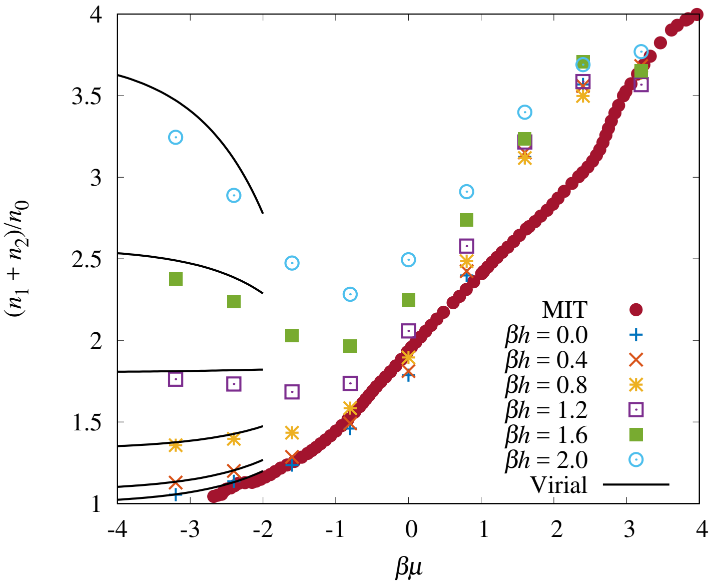

Figure 7.4: Density $n = n_1 + n_2$ of the spin-polarized Fermi gas at unitarity in three spatial dimensions, normalized by the density of the non-interacting, unpolarized system n_0. Results using CL are shown in colored points for chemical potential asymmetries $\beta h = 0.0, 0.4, 0.8, 1.2, 1.6$, and 2.0 at a spatial lattice volume of $N_x^3 = 7^3$. The second-order virial expansion is shown in solid black lines. Additionally, experimental results for the unpolarized system at unitarity are shown in solid red circles (see Ref. [4]).

the parameter region that was studied, the balanced equation of state is in excellent agreement with the third-order virial expansion for $\beta\mu \lesssim -1$. Additionally, the isothermal compressibility held at constant temperature,

$$\kappa = \frac{1}{n}\frac{\partial n}{\partial P}\bigg|_T, \tag{7.7}$$

is also in excellent agreement with experimental values and the third-order virial expansion above the superfluid phase transition, as displayed in Fig. 7.3 (bottom). Although quantitative discrepancies are apparent at the phase transition of the compressibility, the location of the sharp peak at $P/P_0 \approx 0.5$ is in agreement with experiment. The smoothness of these curves in both the density and compressibility EOS indicate that statistical uncertainties are well controlled and are roughly the size of the plotted symbols. However, close to the phase transition, all state-of-the-art methods shown display finite-range and finite-volume effects, once again highlighting the challenge of these calculations.

Provided the excellent agreement of the density and compressibility equations of state for where $\mu_\uparrow = \mu_\downarrow$, we now move to discuss the unbalanced case. Initial results for the density equation of state of the polarized unitary Fermi gas [114] at $N_x^3 = 7^3$ are shown in Fig. 7.4 against unpolarized experimental results and

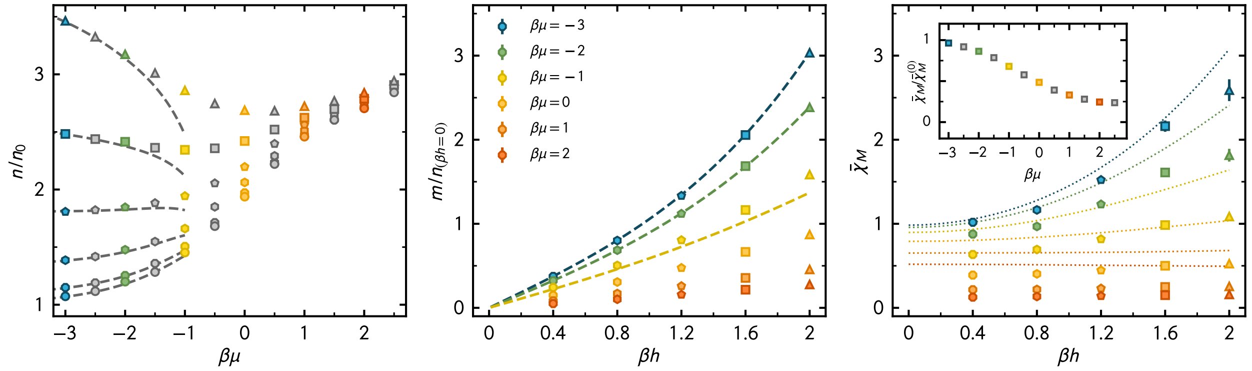

Figure 7.5: *Left:* Density of the UFG in units of the noninteracting density, from top to bottom: $\beta h = 0$ (circles), 0.4 (octagons), 0.8 (hexagons), 1.2 (pentagons), 1.6 (squares), 2.0 (triangles), compared to the third-order virial expansion (dashed lines). Note the colors encode fixed values of $\beta\mu$ shown in all panels. *Center:* Magnetization in units of the interacting density for the balanced system as a function of βh for several values of $\beta\mu$. For $\beta\mu \leq -1.0$, the third-order virial expansion is shown with dashed lines. *Right:* Dimensionless magnetic susceptibility $\bar{\chi}_M$ as a function of βh (symbols) compared to the corresponding susceptibility of the free Fermi gas $\bar{\chi}_M^0$ (dotted lines) at equal chemical potential and asymmetry (color and shake coding match other panels). *Inset:* Ratio $\bar{\chi}_M / \bar{\chi}_M^0$ as a function of $\beta\mu$ at $\beta h = 0.4$.

the second-order virial expansion. Agreement with these limits is not ideal; the CL data does not heel appropriately to the virial expansion for larger values of βh, and finite range effects are strongly evident in the deep quantum regime. As such, larger lattices are required to correctly determine the density equation of state, as well as the other thermodynamic quantities derived from it.

Such equations of state at a more appropriate spatial lattice size of $N_x^3 = 11^3$ are shown in Fig. 7.5. The left and center panels show the density and magnetization equation of state, respectively, and are compared with the third-order virial expansion in the appropriate regimes. Once again, we find excellent agreement for sufficiently negative $\beta\mu$. However, as was also observed in the one-dimensional case, the regime of validity for the virial expansion appears to shrink as βh is increased.

APPENDIX: NLO WEAK-COUPLING EXPANSION FOR POLARIZED SYSTEMS

In Chapter 5 we presented the results of a high-order perturbative expansion for the grand-canonical partition function of interacting quantum gases using a Hubbard-Stratonovich representation. Here we will in complete detail provide a derivation of the next-to-leading order (NLO) expansion for the case of a polarized Fermi gas with contact interactions, as was discussed in Chapter 4.

We are working to compute an expansion for the partition function in the grand canonical ensemble for a polarized system with $N_f = 2$, where we have some population of spin-up (↑) and spin-down (↓) fermions. Therefore, under a path integral representation, we begin with

$$\mathcal{Z} = e^{-\beta\Omega} = \int \mathcal{D}\sigma \; \det\left(1 + z_{\uparrow}\mathcal{U}\right)\det\left(1 + z_{\downarrow}\mathcal{U}\right). \tag{A1}$$

We introduce the expansion by expanding the matrix product $\mathcal{U}$ in a Taylor's series in the parameter $A \equiv \sqrt{2(e^{\tau g} - 1)}$ about $A = 0$ (corresponding to the weak-coupling limit),

$$\mathcal{U}[\sigma] = \mathcal{U}_0 + A\mathcal{U}_1 + \frac{A^2}{2}\mathcal{U}_2 + \cdots, \tag{A2}$$

where we define the notation

$$\mathcal{U}_j = \left.\frac{\partial^j \mathcal{U}[\sigma]}{\partial A^j}\right|_{A=0}. \tag{A3}$$

Equivalently, we perform a series expansion of the determinant, where in order to evaluate the relevant derivatives we make use of the identity

$$\frac{\partial}{\partial\lambda}\det[M(\lambda)] = \det[M(\lambda)]\mathrm{Tr}\left[M^{-1}\frac{\partial M}{\partial\lambda}\right]. \tag{A4}$$

Therefore, we note the evaluations

$$\left.\frac{\partial}{\partial A}\det(1 + z\mathcal{U})\right|_{A=0} = \det(1 + z\mathcal{U}_0)\mathrm{Tr}\left[\frac{z\mathcal{U}_1}{1 + z\mathcal{U}_0}\right] \tag{A5}$$

and

$$\frac{\partial^2}{\partial A^2}\det(1+z\mathcal{U})\bigg|_{A=0} = \det(1+z\mathcal{U}_0)\left(\mathrm{Tr}\left[\frac{z\mathcal{U}_2}{1+z\mathcal{U}_0}\right]-\mathrm{Tr}\left[\frac{z^2\mathcal{U}_1^2}{(1+z\mathcal{U}_0)^2}\right]\right) + \det(1+z\mathcal{U}_0)\mathrm{Tr}^2\left[\frac{z\mathcal{U}_1}{1+z\mathcal{U}_0}\right]. \tag{A6}$$

The series expansion of the fermion determinant for a single flavor is then written as, after factoring out the common non-interacting determinant,

$$\det(1+z\mathcal{U}) = \det(1+z\mathcal{U}_0)\left(1+A\mathrm{Tr}\left[\frac{z\mathcal{U}_1}{1+z\mathcal{U}_0}\right]+\frac{A^2}{2}\mathrm{Tr}\left[\frac{z\mathcal{U}_2}{1+z\mathcal{U}_0}\right] -\frac{A^2}{2}\mathrm{Tr}\left[\frac{z^2\mathcal{U}_1^2}{(1+z\mathcal{U}_0)^2}\right]+\frac{A^2}{2}\mathrm{Tr}^2\left[\frac{z\mathcal{U}_1}{1+z\mathcal{U}_0}\right]+\cdots\right). \tag{A7}$$

To consider two flavors of particles (spin-up and spin-down), we take the product of two such expansions, and place a subscript on the fugacity z to distinguish the two species,

$$\begin{aligned}\det(1+z_\uparrow\mathcal{U})\det(1+z_\downarrow\mathcal{U}) &= \det(1+z_\uparrow\mathcal{U}_0)\det(1+z_\downarrow\mathcal{U}_0)\Bigg[1+A\left(\mathrm{Tr}\left[\frac{z_\uparrow\mathcal{U}_1}{1+z_\uparrow\mathcal{U}_0}\right]\right.\\ &\left.+\mathrm{Tr}\left[\frac{z_\downarrow\mathcal{U}_1}{1+z_\downarrow\mathcal{U}_0}\right]\right)+\frac{A^2}{2}\left(\mathrm{Tr}^2\left[\frac{z_\uparrow\mathcal{U}_1}{1+z_\uparrow\mathcal{U}_0}\right]+\mathrm{Tr}^2\left[\frac{z_\downarrow\mathcal{U}_1}{1+z_\downarrow\mathcal{U}_0}\right]+2\,\mathrm{Tr}\left[\frac{z_\uparrow\mathcal{U}_1}{1+z_\uparrow\mathcal{U}_0}\right]\mathrm{Tr}\left[\frac{z_\downarrow\mathcal{U}_1}{1+z_\downarrow\mathcal{U}_0}\right]\right.\\ &\left.-\mathrm{Tr}\left[\frac{z_\uparrow^2\mathcal{U}_1^2}{(1+z_\uparrow\mathcal{U}_0)^2}\right]-\mathrm{Tr}\left[\frac{z_\downarrow^2\mathcal{U}_1^2}{(1+z_\downarrow\mathcal{U}_0)^2}\right]+\mathrm{Tr}\left[\frac{z_\uparrow\mathcal{U}_2}{1+z_\uparrow\mathcal{U}_0}\right]+\mathrm{Tr}\left[\frac{z_\downarrow\mathcal{U}_2}{1+z_\downarrow\mathcal{U}_0}\right]\right)+\cdots\Bigg].\end{aligned} \tag{A8}$$

To determine the partition function to second-order in A, which we denote here as $\mathcal{Z}^{(2)}$, we must compute the path integral of the above expression. However, before moving to this step, we must determine how to explicitly represent the matrices $\mathcal{U}_j$ that appear in Eq. (A8), where all the dynamics of the Hamiltonian are contained. Recall that in general, through a Trotter-Suzuki decomposition $\mathcal{U}[\sigma]$ is given by

$$\mathcal{U}[\sigma] = \prod_{i=1}^{N_\tau}\mathcal{T}\mathcal{V}[\sigma_i], \tag{A9}$$

where for a contact interaction the Hubbard-Stratonovich transformation gives

$$\mathcal{V}[\sigma_i] = 1 + A\sin(\sigma_i), \tag{A10}$$

given that $\sigma \epsilon [-\pi, \pi]$. It may be easily noted that

$$\mathcal{U}_0 = e^{-\beta \hat{T}}. \tag{A11}$$

A first derivative of $\mathcal{U}[\sigma]$ with respect to A, and then evaluating $A = 0$ will give

$$\mathcal{U}_1 = \sum_{j=1}^{N_\tau} \left(e^{-\tau \hat{T}}\right)^{j-1} \sin(\sigma_j) \left(e^{-\tau \hat{T}}\right)^{N_\tau - j}, \tag{A12}$$

and similarly, a second derivative will give

$$\mathcal{U}_2 = \sum_{j,k=1}^{N_\tau} \left(e^{-\tau \hat{T}}\right)^{k-1} \sin(\sigma_k) \left(e^{-\tau \hat{T}}\right)^{j-k} \sin(\sigma_j) \left(e^{-\tau \hat{T}}\right)^{N_\tau - j - 1}. \tag{A13}$$

Since $\det(1 + z_\uparrow \mathcal{U}_0) \det(1 + z_\downarrow \mathcal{U}_0)$ is independent of the auxiliary field σ, we will factor it out and compute the path integral within the square brackets term by term. For the terms that are linear in A, where for brevity we denote $s = \uparrow, \downarrow$,

$$\begin{aligned} A \int \mathcal{D}\sigma \, \mathrm{Tr}\left[\frac{z_s \mathcal{U}_1}{1 + z_s \mathcal{U}_0}\right] &= A z_s \int \mathcal{D}\sigma \sum_a \sum_{j=1}^{N_\tau} \left[\frac{e^{-\beta \hat{T}}}{1 + z_s e^{-\beta \hat{T}}}\right]_{aa} [\sin(\sigma_j)]_a & \text{(A14)} \\ &= A z_s \sum_a \sum_{j=1}^{N_\tau} \left[\frac{e^{-\beta \hat{T}}}{1 + z_s e^{-\beta \hat{T}}}\right]_{aa} \int_{-\pi}^{\pi} \frac{d\sigma_j}{2\pi} [\sin(\sigma_j)]_a & \text{(A15)} \\ &= 0 & \text{(A16)} \end{aligned}$$

since the integral over the odd integrand vanishes. Note here that j is a temporal index, while a is a spatial index. Therefore, we have that the first-order contribution in the perturbation expansion is zero, and we must proceed to A^2 in order to obtain the next-to-leading order result. For the case of the two terms where the trace is squared, we have the path integral

$$\begin{align}
\frac{A^2}{2}\int \mathcal{D}\sigma\, \mathrm{Tr}^2\left[\frac{z_s\mathcal{U}_1}{1+z_s\mathcal{U}_0}\right] &= \frac{A^2}{2}z_s^2\int \mathcal{D}\sigma \sum_{j,k=1}^{N_\tau}\left(\sum_a\left[\frac{e^{-\beta\hat{T}}}{1+z_se^{-\beta\hat{T}}}\right]_{aa}[\sin(\sigma_j)]_a\right. \nonumber\\
&\quad \left.\times\sum_b\left[\frac{e^{-\beta\hat{T}}}{1+z_se^{-\beta\hat{T}}}\right]_{bb}[\sin(\sigma_j)]_b\right) \tag{A17}\\
&= \frac{A^2}{2}z_s^2\sum_{j,k=1}^{N_\tau}\sum_{a,b}\left[\frac{e^{-\beta\hat{T}}}{1+z_se^{-\beta\hat{T}}}\right]_{aa}\left[\frac{e^{-\beta\hat{T}}}{1+z_se^{-\beta\hat{T}}}\right]_{bb} \nonumber\\
&\quad \times\int_{-\pi}^{\pi}\frac{d\sigma_i\,d\sigma_j}{2\pi}[\sin(\sigma_j)]_a[\sin(\sigma_k)]_b \tag{A18}\\
&= \frac{A^2}{2}z_s^2\sum_{j,k=1}^{N_\tau}\sum_{a,b}\left[\frac{e^{-\beta\hat{T}}}{1+z_se^{-\beta\hat{T}}}\right]_{aa}\left[\frac{e^{-\beta\hat{T}}}{1+z_se^{-\beta\hat{T}}}\right]_{bb}\frac{\delta_{jk}\delta_{ab}}{2} \tag{A19}\\
&= \frac{A^2}{4}z_s^2\sum_{j=1}^{N_\tau}\sum_a\frac{A^2}{2}z_s\sum_{j,k=1}^{N_\tau}\sum_{a,b}\left[\frac{e^{-\beta\hat{T}}}{1+z_se^{-\beta\hat{T}}}\right]_{aa}\left[\frac{e^{-\beta\hat{T}}}{1+z_se^{-\beta\hat{T}}}\right]_{bb} \tag{A20}\\
&= \frac{A^2}{4}z_s^2N_\tau\sum_a\left[\frac{e^{-\beta\hat{T}}}{1+z_se^{-\beta\hat{T}}}\right]_{aa}^2 \tag{A21}
\end{align}$$

Next, let's evaluate the path integral over the negative term where we a trace over the factor of $\mathcal{U}^2$, such that

$$\begin{align}
-\frac{A^2}{2}\int \mathcal{D}\sigma\, \mathrm{Tr}\left[\frac{z_s^2\mathcal{U}_1^2}{(1+z_s\mathcal{U}_0)^2}\right] &= \frac{A^2}{2}z_s^2\int \mathcal{D}\sigma \sum_{j,k=1}^{N_\tau}\sum_{a,b}\left[\frac{e^{-\beta\hat{T}}}{1+z_se^{-\beta\hat{T}}}\right]_{aa}[\sin(\sigma_j)]_a \nonumber\\
&\quad \times\left[\frac{e^{-\beta\hat{T}}}{1+z_se^{-\beta\hat{T}}}\right]_{bb}[\sin(\sigma_j)]_b \tag{A22}\\
&= -\frac{A^2}{4}z_s^2N_\tau\sum_a\left[\frac{e^{-\beta\hat{T}}}{1+z_se^{-\beta\hat{T}}}\right]_{aa}^2 \tag{A23}
\end{align}$$

by the same argument made above. Clearly, these two terms will cancel.

Finally, let's consider what should be the only non-vanishing term in this second-order perturbation expansion. Therefore, as a shorthand we write that

$$\mathcal{Z}^{(2)} = A^2\int \mathcal{D}\sigma\, \mathrm{Tr}\left[\frac{z_\uparrow\mathcal{U}_1}{1+z_\uparrow\mathcal{U}_0}\right]\mathrm{Tr}\left[\frac{z_\downarrow\mathcal{U}_1}{1+z_\downarrow\mathcal{U}_0}\right], \tag{A24}$$

so then

$$\begin{aligned}
\mathcal{Z}^{(2)} &= A^2 z_\uparrow z_\downarrow \int \mathcal{D}\sigma \sum_{j,k=1}^{N_\tau} \left(\sum_a \left[\frac{e^{-\beta \hat{T}}}{1+z_\uparrow e^{-\beta \hat{T}}} \right]_{aa} [\sin(\sigma_j)]_a \right. \\
&\qquad \left. \times \sum_b \left[\frac{e^{-\beta \hat{T}}}{1+z_\downarrow e^{-\beta \hat{T}}} \right]_{bb} [\sin(\sigma_k)]_b \right) &\text{(A25)} \\
&= A^2 z_\uparrow z_\downarrow \sum_{j,k=1}^{N_\tau} \sum_{a,b} \left[\frac{e^{-\beta \hat{T}}}{1+z_\uparrow e^{-\beta \hat{T}}} \right]_{aa} \left[\frac{e^{-\beta \hat{T}}}{1+z_\downarrow e^{-\beta \hat{T}}} \right]_{bb} \\
&\qquad \times \int_{-\pi,\pi} \frac{d\sigma_j \, d\sigma_k}{2\pi} [\sin(\sigma_j)]_a [\sin(\sigma_k)]_b &\text{(A26)} \\
&= A^2 z_\uparrow z_\downarrow \sum_{j,k=1}^{N_\tau} \sum_{a,b} \left[\frac{e^{-\beta \hat{T}}}{1+z_\uparrow e^{-\beta \hat{T}}} \right]_{aa} \left[\frac{e^{-\beta \hat{T}}}{1+z_\downarrow e^{-\beta \hat{T}}} \right]_{bb} \frac{\delta_{jk}\delta_{ab}}{2} &\text{(A27)} \\
&= \frac{A^2}{2} z_\uparrow z_\downarrow \sum_{j=1}^{N_\tau} \sum_a \left[\frac{e^{-\beta \hat{T}}}{1+z_\uparrow e^{-\beta \hat{T}}} \right]_{aa} \left[\frac{e^{-\beta \hat{T}}}{1+z_\downarrow e^{-\beta \hat{T}}} \right]_{aa} &\text{(A28)} \\
&= \frac{A^2}{2} N_\tau z_\uparrow z_\downarrow \sum_a \left[\frac{e^{-\beta \hat{T}}}{1+z_\uparrow e^{-\beta \hat{T}}} \right]_{aa} \left[\frac{e^{-\beta \hat{T}}}{1+z_\downarrow e^{-\beta \hat{T}}} \right]_{aa} &\text{(A29)}
\end{aligned}$$

Notice that the index a on the Boltzmann factors place the kinetic energy operator $\hat{T}$ in the coordinate representation, when it would be more useful to evaluate these matrix elements in the diagonal momentum basis. Therefore, we insert two Fourier transforms $\hat{\mathcal{F}}(a,p)$ that will introduce sums over all lattice momenta, and therefore leave the product independent of spatial coordinates (which introduces a factor of the volume at the end of the calculation). We define

$$\hat{\mathcal{F}} = \frac{1}{N_x} \sum_p e^{-i\hat{p}(a-a')} \tag{A30}$$

and also similarly,

$$\hat{\mathcal{F}}^\dagger = \frac{1}{N_x} \sum_p e^{i\hat{p}(a-a')} \tag{A31}$$

so therefore we now write that, where for a non-relativistic system we take $\hat{T} = \hat{p}^2/2m$,

$$\begin{aligned}
\mathcal{Z}^{(2)} &= \frac{A^2}{2} N_\tau z_\uparrow z_\downarrow \sum_a \hat{\mathcal{F}} \left[\frac{e^{-\beta \hat{T}}}{1 + z_\uparrow e^{-\beta \hat{T}}} \right]_{aa} \hat{\mathcal{F}}^\dagger \hat{\mathcal{F}} \left[\frac{e^{-\beta \hat{T}}}{1 + z_\downarrow e^{-\beta \hat{T}}} \right]_{aa} \hat{\mathcal{F}}^\dagger & \text{(A32)} \\
&= \frac{A^2 N_\tau}{2N_x^2} z_\uparrow z_\downarrow \sum_a \left(\sum_p \left[\frac{e^{-\beta \hat{p}^2/2m}}{1 + z_\uparrow e^{-\beta \hat{p}^2/2m}} \right] \right) \left(\sum_p \left[\frac{e^{-\beta \hat{p}^2/2m}}{1 + z_\downarrow e^{-\beta \hat{p}^2/2m}} \right] \right) & \text{(A33)} \\
&= \frac{A^2 N_\tau}{2N_x} z_\uparrow z_\downarrow \prod_{s=\uparrow,\downarrow} \left(\sum_p \left[\frac{e^{-\beta \epsilon_k}}{1 + z_s e^{-\beta \epsilon_k}} \right] \right) & \text{(A34)}
\end{aligned}$$

where we have set $\hat{p}^2 |\psi\rangle = k^2$ and $\epsilon_k = k^2/2m$ where $k = -(N_x - 1)/2 \ldots (N_x - 1)/2 - 1$. Also notice that $z_\uparrow z_\downarrow = e^{2\beta\mu}$, and $\beta = \tau N_\tau$. Therefore, we have the result

$$\mathcal{Z}^{(2)} = \frac{\beta}{2\tau N_x} A^2 e^{2\beta\mu} \prod_{s=\uparrow,\downarrow} \left(\sum_k \left[\frac{e^{-\beta \epsilon_k}}{1 + z_s e^{-\beta \epsilon_k}} \right] \right). \tag{A35}$$

The complete grand-canonical partition function to second-order will be given by $\mathcal{Z} = \mathcal{Z}^{(0)}(1 + \mathcal{Z}^{(2)})$, so therefore in order to compute thermodynamic observables more easily, we write that

$$\ln \mathcal{Z} = \ln \mathcal{Z}^{(0)} + \ln(1 + \mathcal{Z}^{(2)}) \tag{A36}$$

where $\mathcal{Z}^{(0)}$ is the non-interacting partition function. In order to consistently expand $\ln Z$ to order A^2, we expand $\ln(1 + \mathcal{Z}^{(2)}) \approx \mathcal{Z}^{(2)}$, which gives the final result

$$\boxed{\ln \mathcal{Z} = \ln \mathcal{Z}^{(0)} + \frac{\beta}{2\tau N_x} (A e^{\beta\mu})^2 \prod_{s=\uparrow,\downarrow} \left(\sum_k \left[\frac{e^{-\beta \epsilon_k}}{1 + z_s e^{-\beta \epsilon_k}} \right] \right)} \tag{A37}$$

REFERENCES

[1] M. D. Hoffman, P. D. Javernick, A. C. Loheac, W. J. Porter, E. R. Anderson, and J. E. Drut, *Universality in one-dimensional fermions at finite temperature: Density, pressure, compressibility, and contact*, Phys. Rev. A **91**, 033618 (2015).

[2] A. C. Loheac, J. Braun, J. E. Drut, and D. Roscher, *Thermal equation of state of polarized fermions in one dimension via complex chemical potentials*, Phys. Rev. A **92**, 063609 (2015).

[3] E. R. Anderson and J. E. Drut, *Pressure, Compressibility, and Contact of the Two-Dimensional Attractive Fermi Gas*, Phys. Rev. Lett. **115**, 115301 (2015).

[4] M. J. H. Ku, A. T. Sommer, L. W. Cheuk, and M. W. Zwierlein, *Revealing the Superfluid Lambda Transition in the Universal Thermodynamics of a Unitary Fermi Gas*, Science **335**, 6068, 563 (2012).

[5] K. V. Houcke, F. Werner, E. Kozik, N. Prokof'ev, B. Svistunov, M. J. H. Ku, A. T. Sommer, L. W. Cheuk, A. Schirotzek, and M. W. Zwierlein, *Feynman diagrams versus Fermi-gas Feynman emulator*, Nature Physics **8**, 366 (2012).

[6] J. E. Drut, T. A. Lähde, G. Wlazłowski, and P. Magierski, *Equation of state of the unitary Fermi gas: An update on lattice calculations*, Phys. Rev. A **85**, 051601 (2012).

[7] S. J. Aarseth, *Gravitational N-body simulations*, (Cambridge University Press, 2003).

[8] J. Carlson, S. Gandolfi, F. Pederiva, S. C. Pieper, R. Schiavilla, K. E. Schmidt, and R. B. Wiringa, *Quantum Monte Carlo methods for nuclear physics*, Rev. Mod. Phys. **87**, 1067 (2015).

[9] J. Kolorenč and L. Mitas, *Applications of quantum Monte Carlo methods in condensed systems*, Reports on Progress in Physics **74**, 2, 026502 (2011).

[10] A. Bazavov, D. Toussaint, C. Bernard, J. Laiho, C. DeTar, L. Levkova, M. B. Oktay, S. Gottlieb, U. M. Heller, J. E. Hetrick, P. B. Mackenzie, R. Sugar, and R. S. Van de Water, *Nonperturbative QCD simulations with* $2 + 1$ *flavors of improved staggered quarks*, Rev. Mod. Phys. **82**, 1349 (2010).

[11] M. Troyer and U.-J. Wiese, *Computational Complexity and Fundamental Limitations to Fermionic Quantum Monte Carlo Simulations*, Phys. Rev. Lett. **94**, 170201 (2005).

[12] M. Gaudin, *Un systeme a une dimension de fermions en interaction*, Physics Letters A **24**, 1, 55 (1967).

[13] C. N. Yang, *Some Exact Results for the Many-Body Problem in one Dimension with Repulsive Delta-Function Interaction*, Phys. Rev. Lett. **19**, 1312 (1967).

[14] K. G. Wilson, *Confinement of quarks*, Phys. Rev. D **10**, 2445 (1974).

[15] C. Gattringer and C. B. Lang, *Quantum Chromodynamics on the Lattice*, vol. 788, (Springer-Verlag Berlin Heidelberg, 2010).

[16] F. Knechtli, M. Günther, and M. Peardon, *Lattice Quantum Chromodynamics: Practical Essentials*, (Springer Netherlands, 2017).

[17] H. Bethe, *Zur Theorie der Metalle*, Zeitschrift für Physik **71**, 3, 205 (1931).

[18] M. Karbach and G. Müller, *Introduction to the Bethe Ansatz I*, Computers in Physics **11**, 1, 36 (1997).

[19] M. Karbach, K. Hu, and G. Müller, *Introduction to the Bethe Ansatz II*, Computers in Physics **12**, 6, 565 (1998).

[20] M. Karbach, K. Hu, and G. Müller, *Introduction to the Bethe Ansatz III*, arXiv:cond-mat/0008018 [cond-mat.stat-mech] (2000).

[21] C. N. Yang and C. P. Yang, *Thermodynamics of a One Dimensional System of Bosons with Repulsive Delta Function Interaction*, Journal of Mathematical Physics **10**, 7, 1115 (1969).

[22] S. J. van Tongeren, *Introduction to the thermodynamic Bethe ansatz*, Journal of Physics A: Mathematical and Theoretical **49**, 32, 323005 (2016).

[23] M. Gaudin, *Thermodynamics of the Heisenberg-Ising Ring for* $\Delta >\sim 1$, Phys. Rev. Lett. **26**, 1301 (1971).

[24] M. Takahashi, *One-Dimensional Hubbard Model at Finite Temperature*, Progress of Theoretical Physics **47**, 1, 69 (1972).

[25] P. Echenique and J. L. Alonso, *A mathematical and computational review of Hartree-Fock SCF methods in quantum chemistry*, Molecular Physics **105**, 23-24, 3057 (2007).

[26] C. Pisani, *Hartree-Fock ab initio approaches to the solution of some solid-state problems: state of the art and prospects*, International Reviews in Physical Chemistry **6**, 4, 367 (1987).

[27] M. H. Kalos, *Monte Carlo Calculations of the Ground State of Three- and Four-Body Nuclei*, Phys. Rev. **128**, 1791 (1962).

[28] J. Toulouse, R. Assaraf, and C. J. Umrigar, *Chapter Fifteen - Introduction to the Variational and Diffusion Monte Carlo Methods*, in P. E. Hoggan and T. Ozdogan, eds., *Electron Correlation in Molecules - ab initio Beyond Gaussian Quantum Chemistry*, vol. 73 of *Advances in Quantum Chemistry*, 285 – 314, (Academic Press, 2016).

[29] I. Brida, S. C. Pieper, and R. B. Wiringa, *Quantum Monte Carlo calculations of spectroscopic overlaps in* $A \leqslant 7$ *nuclei*, Phys. Rev. C **84**, 024319 (2011).

[30] E. A. McCutchan, C. J. Lister, S. C. Pieper, R. B. Wiringa, D. Seweryniak, J. P. Greene, P. F. Bertone, M. P. Carpenter, C. J. Chiara, G. Gürdal, C. R. Hoffman, R. V. F. Janssens, T. L. Khoo, T. Lauritsen, and S. Zhu, *Lifetime of the* 2_1^+ *state in* ^{10}C, Phys. Rev. C **86**, 014312 (2012).

[31] A. Lovato, S. Gandolfi, R. Butler, J. Carlson, E. Lusk, S. C. Pieper, and R. Schiavilla, *Charge Form Factor and Sum Rules of Electromagnetic Response Functions in* ^{12}**C**, Phys. Rev. Lett. **111**, 092501 (2013).

[32] S. Pastore, S. C. Pieper, R. Schiavilla, and R. B. Wiringa, *Quantum Monte Carlo calculations of electromagnetic moments and transitions in* $A \leq 9$ *nuclei with meson-exchange currents derived from chiral effective field theory*, Phys. Rev. C **87**, 035503 (2013).

[33] S. Pastore, R. B. Wiringa, S. C. Pieper, and R. Schiavilla, *Quantum Monte Carlo calculations of electromagnetic transitions in* $^{8}\mathrm{Be}$ *with meson-exchange currents derived from chiral effective field theory*, Phys. Rev. C **90**, 024321 (2014).

[34] R. B. Wiringa, S. Pastore, S. C. Pieper, and G. A. Miller, *Charge-symmetry breaking forces and isospin mixing in* ^{8}Be, Phys. Rev. C **88**, 044333 (2013).

[35] S. Pastore, J. Carlson, V. Cirigliano, W. Dekens, E. Mereghetti, and R. B. Wiringa, *Neutrinoless double-β decay matrix elements in light nuclei*, Phys. Rev. C **97**, 014606 (2018).

[36] P. Hohenberg and W. Kohn, *Inhomogeneous Electron Gas*, Phys. Rev. **136**, B864 (1964).

[37] R. O. Jones, *Density functional theory: Its origins, rise to prominence, and future*, Rev. Mod. Phys. **87**, 897 (2015).

[38] R. G. Parr, *Density Functional Theory*, Annual Review of Physical Chemistry **34**, 1, 631 (1983).

[39] P. N. Ma, S. Pilati, M. Troyer, and X. Dai, *Density functional theory for atomic Fermi Gases*, Nature Physics **8**, 601 (2012).

[40] M. Cristoforetti, F. Di Renzo, and L. Scorzato, *New approach to the sign problem in quantum field theories: High density QCD on a Lefschetz thimble*, Phys. Rev. D **86**, 074506 (2012).

[41] M. Cristoforetti, F. Di Renzo, A. Mukherjee, and L. Scorzato, *Monte Carlo simulations on the Lefschetz thimble: Taming the sign problem*, Phys. Rev. D **88**, 051501 (2013).

[42] H. Fujii, D. Honda, M. Kato, Y. Kikukawa, S. Komatsu, and T. Sano, *Hybrid Monte Carlo on Lefschetz thimbles — A study of the residual sign problem*, Journal of High Energy Physics **2013**, 10, 147 (2013).

[43] G. Aarts, L. Bongiovanni, E. Seiler, and D. Sexty, *Some remarks on Lefschetz thimbles and complex Langevin dynamics*, Journal of High Energy Physics **2014**, 10, 159 (2014).

[44] A. Alexandru, G. Basar, P. F. Bedaque, G. W. Ridgway, and N. C. Warrington, *Sign problem and Monte Carlo calculations beyond Lefschetz thimbles*, Journal of High Energy Physics **2016**, 5, 53 (2016).

[45] S. Chandrasekharan, *Fermion bag approach to lattice field theories*, Phys. Rev. D **82**, 025007 (2010).

[46] S. Chandrasekharan, *Fermion bag approach to fermion sign problems*, The European Physical Journal A **49**, 7, 90 (2013).

[47] E. Huffman and S. Chandrasekharan, *Fermion bag approach to Hamiltonian lattice field theories in continuous time*, Phys. Rev. D **96**, 114502 (2017).

[48] E. Huffman, *Monte Carlo methods in continuous time for lattice Hamiltonian*, Proc. Sci., LATTICE2016, 258 (2016).

[49] K. Fenech, P. Dyke, T. Peppler, M. G. Lingham, S. Hoinka, H. Hu, and C. J. Vale, *Thermodynamics of an Attractive 2D Fermi Gas*, Phys. Rev. Lett. **116**, 045302 (2016).

[50] P. Kapitza, *Viscosity of Liquid Helium below the λ-Point*, Nature **141**, 74 (1938).

[51] J. F. Allen and A. D. Misener, *Flow Phenomena in Liquid Helium II*, Nature **142**, 643 (1938).

[52] M. H. Anderson, J. R. Ensher, M. R. Matthews, C. E. Wieman, and E. A. Cornell, *Observation of Bose-Einstein Condensation in a Dilute Atomic Vapor*, Science **269**, 5221, 198 (1995).

[53] K. M. O'Hara, S. L. Hemmer, M. E. Gehm, S. R. Granade, and J. E. Thomas, *Observation of a Strongly Interacting Degenerate Fermi Gas of Atoms*, Science **298**, 5601, 2179 (2002).

[54] L. Luo, B. Clancy, J. Joseph, J. Kinast, and J. E. Thomas, *Measurement of the Entropy and Critical Temperature of a Strongly Interacting Fermi Gas*, Phys. Rev. Lett. **98**, 080402 (2007).

[55] B. DeMarco and D. S. Jin, *Onset of Fermi Degeneracy in a Trapped Atomic Gas*, Science **285**, 5434, 1703 (1999).

[56] J. P. Gaebler, J. T. Stewart, T. E. Drake, D. S. Jin, A. Perali, P. Pieri, and G. C. Strinati, *Observation of pseudogap behaviour in a strongly interacting Fermi gas*, Nature Physics **6**, 569 (2010).

[57] C. A. Regal, M. Greiner, and D. S. Jin, *Observation of Resonance Condensation of Fermionic Atom Pairs*, Phys. Rev. Lett. **92**, 040403 (2004).

[58] R. Islam, R. Ma, P. M. Preiss, M. E. Tai, A. Lukin, M. Rispoli, and M. Greiner, *Measuring entanglement entropy in a quantum many-body system*, Nature **528**, 77 (2015).

[59] J. E. Drut and W. J. Porter, *Convexity of the Entanglement Entropy of SU($2N$)-Symmetric Fermions with Attractive Interactions*, Phys. Rev. Lett. **114**, 050402 (2015).

[60] J. E. Drut and W. J. Porter, *Hybrid Monte Carlo approach to the entanglement entropy of interacting fermions*, Phys. Rev. B **92**, 125126 (2015).

[61] J. E. Drut and W. J. Porter, *Entanglement, noise, and the cumulant expansion*, Phys. Rev. E **93**, 043301 (2016).

[62] W. J. Porter and J. E. Drut, *Entanglement spectrum and Rényi entropies of nonrelativistic conformal fermions*, Phys. Rev. B **94**, 165112 (2016).

[63] R. K. Pathria and P. D. Beale, *Statistical Mechanics*, (Academic Press, 2011), 3rd ed.

[64] M. Suzuki, *Fractal decomposition of exponential operators with applications to many-body theories and Monte Carlo simulations*, Physics Letters A **146**, 6, 319 (1990).

[65] M. Lüscher, *Volume dependence of the energy spectrum in massive quantum field theories. II. Scattering states*, Comm. Math. Phys. **105**, 2, 153 (1986).

[66] M. Lüscher, *Two-particle states on a torus and their relation to the scattering matrix*, Nuclear Physics B **354**, 2, 531 (1991).

[67] M. Lüscher and U. Wolff, *How to calculate the elastic scattering matrix in two-dimensional quantum field theories by numerical simulation*, Nuclear Physics B **339**, 1, 222 (1990).

[68] W. Zwerger, ed., *The BCS-BEC Crossover and the Unitary Fermi Gas*, (Springer-Verlag, 2012).

[69] J. E. Drut, *Improved lattice operators for nonrelativistic fermions*, Phys. Rev. A **86**, 013604 (2012).

[70] R. Blankenbecler, D. J. Scalapino, and R. L. Sugar, *Monte Carlo calculations of coupled boson-fermion systems. I*, Phys. Rev. D **24**, 2278 (1981).

[71] C. W. Johnson, W. E. Ormand, K. S. McElvain, and H. Shan, *BIGSTICK: A flexible configuration-interaction shell-model code*, arXiv:1801.08432 [physics.comp-ph] (2018).

[72] L. Beilina, E. Karchevskii, and M. Karchevskii, *Numerical Linear Algebra: Theory and Applications*, (Springer, Cham, 2017).

[73] W. K. Hastings, *Monte Carlo sampling methods using Markov chains and their applications*, Biometrika **57**, 1, 97 (1970).

[74] N. Metropolis, A. W. Rosenbluth, M. N. Rosenbluth, A. H. Teller, and E. Teller, *Equation of State Calculations by Fast Computing Machines*, The Journal of Chemical Physics **21**, 6, 1087 (1953).

[75] S. Duane, A. Kennedy, B. J. Pendleton, and D. Roweth, *Hybrid Monte Carlo*, Physics Letters B **195**, 2, 216 (1987).

[76] R. M. Neal, *MCMC using Hamiltonian dynamics*, arXiv:1206.1901 [stat.CO] (2012).

[77] M. Frigo and S. G. Johnson, *The Design and Implementation of FFTW3*, Proceedings of the IEEE **93**, 2, 216 (2005), special issue on "Program Generation, Optimization, and Platform Adaptation".

[78] S. Tan, *Energetics of a strongly correlated Fermi gas*, Annals of Physics **323**, 12, 2952 (2008).

[79] S. Tan, *Large momentum part of a strongly correlated Fermi gas*, Annals of Physics **323**, 12, 2971 (2008).

[80] S. Tan, *Generalized virial theorem and pressure relation for a strongly correlated Fermi gas*, Annals of Physics **323**, 12, 2987 (2008).

[81] X.-J. Liu, *Virial expansion for a strongly correlated Fermi system and its application to ultracold atomic Fermi gases*, Physics Reports **524**, 2, 37 (2013).

[82] S. Zhang and A. J. Leggett, *Sum-rule analysis of radio-frequency spectroscopy of ultracold Fermi gas*, Phys. Rev. A **77**, 033614 (2008).

[83] F. Werner, *Virial theorems for trapped cold atoms*, Phys. Rev. A **78**, 025601 (2008).

[84] E. Braaten and L. Platter, *Exact Relations for a Strongly Interacting Fermi Gas from the Operator Product Expansion*, Phys. Rev. Lett. **100**, 205301 (2008).

[85] E. Braaten, D. Kang, and L. Platter, *Short-Time Operator Product Expansion for rf Spectroscopy of a Strongly Interacting Fermi Gas*, Phys. Rev. Lett. **104**, 223004 (2010).

[86] V. Romero-Rochin, *The thermodynamic origin of the Contact and its relation to the gap in the BEC-BCS crossover*, arXiv:1012.0236 [cond-mat.quant-gas] (2010).

[87] X. Guan, *Critical phenomena in one dimension from a Bethe ansatz perspective*, International Journal of Modern Physics B **28**, 24, 1430015 (2014).

[88] M. D. Hoffman, A. C. Loheac, W. J. Porter, and J. E. Drut, *Thermodynamics of one-dimensional SU(4) and SU(6) fermions with attractive interactions*, Phys. Rev. A **95**, 033602 (2017).

[89] J. Braun, J.-W. Chen, J. Deng, J. E. Drut, B. Friman, C.-T. Ma, and Y.-D. Tsai, *Imaginary Polarization as a Way to Surmount the Sign Problem in Ab Initio Calculations of Spin-Imbalanced Fermi Gases*, Phys. Rev. Lett. **110**, 130404 (2013).

[90] D. Roscher, J. Braun, J.-W. Chen, and J. E. Drut, *Fermi gases with imaginary mass imbalance and the sign problem in Monte-Carlo calculations*, Journal of Physics G: Nuclear and Particle Physics **41**, 5, 055110 (2014).

[91] J. Braun, J. E. Drut, and D. Roscher, *Zero-Temperature Equation of State of Mass-Imbalanced Resonant Fermi Gases*, Phys. Rev. Lett. **114**, 050404 (2015).

[92] P. de Forcrand and O. Philipsen, *The QCD phase diagram for small densities from imaginary chemical potential*, Nuclear Physics B **642**, 1, 290 (2002).

[93] M. Alford, A. Kapustin, and F. Wilczek, *Imaginary chemical potential and finite fermion density on the lattice*, Phys. Rev. D **59**, 054502 (1999).

[94] P. Cea, L. Cosmai, M. D'Elia, C. Manneschi, and A. Papa, *Analytic continuation of the critical line: Suggestions for QCD*, Phys. Rev. D **80**, 034501 (2009).

[95] M. D'Elia and M.-P. Lombardo, *Finite density QCD via an imaginary chemical potential*, Phys. Rev. D **67**, 014505 (2003).

[96] F. Karbstein and M. Thies, *How to get from imaginary to real chemical potential*, Phys. Rev. D **75**, 025003 (2007).

[97] M. Lombardo, *Lattice at finite baryon density: imaginary chemical potential*, PoS(CPOD2006)003 (2006).

[98] A. I. Larkin and Y. N. Ovchinnikov, *Nonuniform state of superconductors*, Sov. Phys. JETP **20**, 762 (1965).

[99] P. Fulde and R. A. Ferrell, *Superconductivity in a Strong Spin-Exchange Field*, Phys. Rev. **135**, A550 (1964).

[100] C. Langmack, M. Barth, W. Zwerger, and E. Braaten, *Clock Shift in a Strongly Interacting Two-Dimensional Fermi Gas*, Phys. Rev. Lett. **108**, 060402 (2012).

[101] J. E. Drut, T. A. Lähde, and T. Ten, *Momentum Distribution and Contact of the Unitary Fermi Gas*, Phys. Rev. Lett. **106**, 205302 (2011).

[102] K. V. Houcke, F. Werner, E. Kozik, N. Prokof'ev, and B. Svistunov, *Contact and Momentum Distribution of the Unitary Fermi Gas by Bold Diagrammatic Monte Carlo*, arXiv:1303.6245 [cond-mat.quant-gas] (2013).

[103] F. Werner and Y. Castin, *General relations for quantum gases in two and three dimensions: Two-component fermions*, Phys. Rev. A **86**, 013626 (2012).

[104] M. Valiente, N. T. Zinner, and K. Mølmer, *Universal relations for the two-dimensional spin-1/2 Fermi gas with contact interactions*, Phys. Rev. A **84**, 063626 (2011).

[105] A. Bulgac, J. E. Drut, and P. Magierski, *Quantum Monte Carlo simulations of the BCS-BEC crossover at finite temperature*, Phys. Rev. A **78**, 023625 (2008).

[106] A. Bulgac, J. E. Drut, and P. Magierski, *Spin* $1/2$ *Fermions in the Unitary Regime: A Superfluid of a New Type*, Phys. Rev. Lett. **96**, 090404 (2006).

[107] F. F. Assaad and H. G. Evertz, *Computational Many-Particle Physics*, (Springer, Berlin, 2008).

[108] D. Lee, *Ground state energy at unitarity*, Phys. Rev. C **78**, 024001 (2008).

[109] D. Lee, *Lattice simulations for few- and many-body systems*, Progress in Particle and Nuclear Physics **63**, 1, 117 (2009).

[110] M. Karabach and G. Müller, *Introduction to the Bethe Ansatz I*, Comput. Phys. **11**, 1, 36 (1997).

[111] X.-W. Guan, M. T. Batchelor, and C. Lee, *Fermi gases in one dimension: From Bethe ansatz to experiments*, Rev. Mod. Phys. **85**, 1633 (2013).

[112] A. C. Loheac and J. E. Drut, *Third-order perturbative lattice and complex Langevin analyses of the finite-temperature equation of state of nonrelativistic fermions in one dimension*, Phys. Rev. D **95**, 094502 (2017).

[113] A. C. Loheac, J. Braun, and J. E. Drut, *Polarized fermions in one dimension: Density and polarization from complex Langevin calculations, perturbation theory, and the virial expansion*, Phys. Rev. D **98**, 054507 (2018).

[114] A. C. Loheac, J. Braun, and J. E. Drut, *Equation of state of non-relativistic matter from automated perturbation theory and complex Langevin*, EPJ Web Conf. **175**, 03007 (2018).

[115] J. E. Drut and A. N. Nicholson, *Lattice methods for strongly interacting many-body systems*, Journal of Physics G: Nuclear and Particle Physics **40**, 4, 043101 (2013).

[116] C. R. Shill and J. E. Drut, *Virial coefficients of one-dimensional and two-dimensional Fermi gases by stochastic methods and a semiclassical lattice approximation*, Phys. Rev. A **98**, 053615 (2018).

[117] G. Aarts, *Introductory lectures on lattice QCD at nonzero baryon number*, Journal of Physics: Conference Series **706**, 2, 022004 (2016).

[118] G. Aarts, *Complex Langevin dynamics and other approaches at finite chemical potential*, Proc. Sci., LATTICE2012, 017 (2013).

[119] D. Sexty, *New algorithms for finite density QCD*, Proc. Sci., LATTICE2014, 016 (2014).

[120] G. Aarts and I.-O. Stamatescu, *Stochastic quantization at finite chemical potential*, Journal of High Energy Physics **2008**, 09, 018 (2008).

[121] E. Seiler, D. Sexty, and I.-O. Stamatescu, *Gauge cooling in complex Langevin for lattice QCD with heavy quarks*, Physics Letters B **723**, 1, 213 (2013).

[122] G. Aarts, F. Attanasio, B. Jäger, and D. Sexty, *The QCD phase diagram in the limit of heavy quarks using complex Langevin dynamics*, Journal of High Energy Physics **2016**, 9, 87 (2016).

[123] D. Sexty, *Simulating full QCD at nonzero density using the complex Langevin equation*, Physics Letters B **729**, 108 (2014).

[124] G. Aarts, E. Seiler, D. Sexty, and I.-O. Stamatescu, *Simulating QCD at nonzero baryon density to all orders in the hopping parameter expansion*, Phys. Rev. D **90**, 114505 (2014).

[125] D. K. Sinclair and J. B. Kogut, *Exploring Complex-Langevin Methods for Finite-Density QCD*, Proc. Sci., LATTICE2016, 153 (2016).

[126] J. Bloch, J. Glesaaen, J. J. M. Verbaarschot, and S. Zafeiropoulos, *Complex Langevin simulation of a random matrix model at nonzero chemical potential*, Journal of High Energy Physics **2018**, 3, 15 (2018).

[127] T. Hayata and A. Yamamoto, *Complex Langevin simulation of quantum vortices in a Bose-Einstein condensate*, Phys. Rev. A **92**, 043628 (2015).

[128] A. Yamamoto and T. Hayata, *Complex Langevin simulation in condensed matter physics*, Proc. Sci., LATTICE2015, 041 (2015).

[129] D. S. Lemons, *Paul Langevin's 1908 paper "On the Theory of Brownian Motion" ["Sur la théorie du mouvement brownien", C. R. Acad. Sci. (Paris) 146, 530-533 (1908)]*, American Journal of Physics **65**, 1079 (1997).

[130] Y. Pomeau and J. Piasecki, *The Langevin equation*, Comptes Rendus Physique **18**, 9, 570 (2017), Science in the making: The Comptes rendus de l'Académie des sciences throughout history.

[131] G. Parisi and T. Yong-Shi, *Perturbation theory without gauge fixing*, Scientia Sinica **24**, 4, 483 (1981).

[132] P. H. Damgaard and H. Hüffel, *Stochastic quantization*, Physics Reports **152**, 5, 227 (1987).

[133] G. G. Batrouni, G. R. Katz, A. S. Kronfeld, G. P. Lepage, B. Svetitsky, and K. G. Wilson, *Langevin simulations of lattice field theories*, Phys. Rev. D **32**, 2736 (1985).

[134] G. Parisi, *On complex probabilities*, Physics Letters B **131**, 4, 393 (1983).

[135] G. Aarts, E. Seiler, and I.-O. Stamatescu, *Complex Langevin method: When can it be trusted?*, Phys. Rev. D **81**, 054508 (2010).

[136] G. Aarts, F. A. James, E. Seiler, and I.-O. Stamatescu, *Adaptive stepsize and instabilities in complex Langevin dynamics*, Physics Letters B **687**, 2, 154 (2010).

[137] J. Bloch, J. Meisinger, and S. Schmalzbauer, *Reweighted complex Langevin and its application to two-dimensional QCD*, Proc. Sci., LATTICE2016, 046 (2017).

[138] J. Bloch, *Reweighting complex Langevin trajectories*, Phys. Rev. D **95**, 054509 (2017).

[139] F. Attanasio and B. Jäger, *Testing dynamic stabilisation in complex Langevin simulations*, Proc. Sci., LATTICE2016, 053 (2016).

[140] G. Aarts, F. Attanasio, B. Jäger, and D. Sexty, *Complex Langevin in Lattice QCD: Dynamic stabilisation and the phase diagram*, Acta Phys. Pol. B Proc. Suppl. **9**, 621 (2016).

[141] J. Carrasquilla and R. G. Melko, *Machine learning phases of matter*, Nature Physics **13**, 431 (2017).

[142] P. Broecker, J. Carrasquilla, R. G. Melko, and S. Trebst, *Machine learning quantum phases of matter beyond the fermion sign problem*, Scientific Reports **7**, 8823 (2017).

[143] M. J. S. Beach, A. Golubeva, and R. G. Melko, *Machine learning vortices at the Kosterlitz-Thouless transition*, Phys. Rev. B **97**, 045207 (2018).

[144] P. Suchsland and S. Wessel, *Parameter diagnostics of phases and phase transition learning by neural networks*, Phys. Rev. B **97**, 174435 (2018).

[145] K. Ch'ng, J. Carrasquilla, R. G. Melko, and E. Khatami, *Machine Learning Phases of Strongly Correlated Fermions*, Phys. Rev. X **7**, 031038 (2017).

[146] G. Carleo and M. Troyer, *Solving the quantum many-body problem with artificial neural networks*, Science **355**, 6325, 602 (2017).

[147] H. Saito, *Solving the Bose-Hubbard Model with Machine Learning*, Journal of the Physical Society of Japan **86**, 9, 093001 (2017).

[148] I. Goodfellow, Y. Bengio, and A. Courville, *Deep Learning*, (MIT Press, Cambridge, MA, 2016).

[149] D. P. Kingma and J. Ba, *Adam: A Method for Stochastic Optimization*, arXiv:1412.6980 [cs.LG] (2014).

[150] L. Rammelmüller, A. C. Loheac, J. E. Drut, and J. Braun, *Finite-Temperature Equation of State of Polarized Fermions at Unitarity*, Phys. Rev. Lett. **121**, 173001 (2018).

[151] L. P. Pitaevskii and A. Rosch, *Breathing modes and hidden symmetry of trapped atoms in two dimensions*, Phys. Rev. A **55**, R853 (1997).

[152] M. Olshanii, H. Perrin, and V. Lorent, *Example of a Quantum Anomaly in the Physics of Ultracold Gases*, Phys. Rev. Lett. **105**, 095302 (2010).

[153] Y. Hu and Z. Liang, *Visualization of Dimensional Effects in Collective Excitations of Optically Trapped Quasi-Two-Dimensional Bose Gases*, Phys. Rev. Lett. **107**, 110401 (2011).

[154] J. Hofmann, *Quantum Anomaly, Universal Relations, and Breathing Mode of a Two-Dimensional Fermi Gas*, Phys. Rev. Lett. **108**, 185303 (2012).

[155] E. Taylor and M. Randeria, *Apparent Low-Energy Scale Invariance in Two-Dimensional Fermi Gases*, Phys. Rev. Lett. **109**, 135301 (2012).

[156] J. E. Drut, J. R. McKenney, W. S. Daza, C. L. Lin, and C. R. Ordóñez, *Quantum Anomaly and Thermodynamics of One-Dimensional Fermions with Three-Body Interactions*, Phys. Rev. Lett. **120**, 243002 (2018).

[157] L. Rammelmüller, W. J. Porter, A. C. Loheac, and J. E. Drut, *Few-fermion systems in one dimension: Ground- and excited-state energies and contacts*, Phys. Rev. A **92**, 013631 (2015).

[158] V. Ngampruetikorn, J. Levinsen, and M. M. Parish, *Pair Correlations in the Two-Dimensional Fermi Gas*, Phys. Rev. Lett. **111**, 265301 (2013).

[159] C. Chafin and T. Schäfer, *Scale breaking and fluid dynamics in a dilute two-dimensional Fermi gas*, Phys. Rev. A **88**, 043636 (2013).

[160] T. Schäfer and D. Teaney, *Nearly perfect fluidity: from cold atomic gases to hot quark gluon plasmas*, Reports on Progress in Physics **72**, 12, 126001 (2009).

[161] S. Giorgini, L. P. Pitaevskii, and S. Stringari, *Theory of ultracold atomic Fermi gases*, Rev. Mod. Phys. **80**, 1215 (2008).

[162] T.-L. Ho, *Universal Thermodynamics of Degenerate Quantum Gases in the Unitarity Limit*, Phys. Rev. Lett. **92**, 090402 (2004).

[163] A. Schwenk and C. J. Pethick, *Resonant Fermi Gases with a Large Effective Range*, Phys. Rev. Lett. **95**, 160401 (2005).

[164] I. Tews, J. M. Lattimer, A. Ohnishi, and E. E. Kolomeitsev, *Symmetry Parameter Constraints from a Lower Bound on Neutron-matter Energy*, The Astrophysical Journal **848**, 2, 105 (2017).

[165] G. C. Strinati, P. Pieri, G. Röpke, P. Schuck, and M. Urban, *The BCS-BEC crossover: From ultra-cold Fermi gases to nuclear systems*, Physics Reports **738**, 1 (2018).

[166] T. Mehen, I. W. Stewart, and M. B. Wise, *Conformal invariance for non-relativistic field theory*, Physics Letters B **474**, 1, 145 (2000).

[167] Y. Nishida and D. T. Son, *Nonrelativistic conformal field theories*, Phys. Rev. D **76**, 086004 (2007).

[168] X. Bekaert, E. Meunier, and S. Moroz, *Towards a gravity dual of the unitary Fermi gas*, Phys. Rev. D **85**, 106001 (2012).

[169] T. Enss, *Quantum critical transport in the unitary Fermi gas*, Phys. Rev. A **86**, 013616 (2012).

[170] I. Bloch, J. Dalibard, and W. Zwerger, *Many-body physics with ultracold gases*, Rev. Mod. Phys. **80**, 885 (2008).

[171] C. Chin, R. Grimm, P. Julienne, and E. Tiesinga, *Feshbach resonances in ultracold gases*, Rev. Mod. Phys. **82**, 1225 (2010).

[172] R. Casalbuoni and G. Nardulli, *Inhomogeneous superconductivity in condensed matter and QCD*, Rev. Mod. Phys. **76**, 263 (2004).

[173] F. Chevy and C. Mora, *Ultra-cold polarized Fermi gases*, Reports on Progress in Physics **73**, 11, 112401 (2010).

[174] K. Gubbels and H. Stoof, *Imbalanced Fermi gases at unitarity*, Physics Reports **525**, 4, 255 (2013).

[175] M. M. Parish, *Quantum Gas Experiments: Exploring Many-Body States*, vol. 3 of *Cold Atoms*, chap. 9, 179–197, (Imperial College Press, London, 2015).

[176] B. S. Chandrasekhar, *A Note On The Maximum Critical Field of High-Field Superconductors*, Applied Physics Letters **1**, 1, 7 (1962).

[177] A. M. Clogston, *Upper Limit for the Critical Field in Hard Superconductors*, Phys. Rev. Lett. **9**, 266 (1962).

[178] A. Perali, P. Pieri, G. C. Strinati, and C. Castellani, *Pseudogap and spectral function from superconducting fluctuations to the bosonic limit*, Phys. Rev. B **66**, 024510 (2002).

[179] Q. Chen, J. Stajic, S. Tan, and K. Levin, *BCS-BEC crossover: From high temperature superconductors to ultracold superfluids*, Physics Reports **412**, 1, 1 (2005).

[180] P. Magierski, G. Wlazłowski, A. Bulgac, and J. E. Drut, *Finite-Temperature Pairing Gap of a Unitary Fermi Gas by Quantum Monte Carlo Calculations*, Phys. Rev. Lett. **103**, 210403 (2009).

[181] P. Magierski, G. Wlazłowski, and A. Bulgac, *Onset of a Pseudogap Regime in Ultracold Fermi Gases*, Phys. Rev. Lett. **107**, 145304 (2011).

[182] G. Wlazłowski, P. Magierski, J. E. Drut, A. Bulgac, and K. J. Roche, *Cooper Pairing Above the Critical Temperature in a Unitary Fermi Gas*, Phys. Rev. Lett. **110**, 090401 (2013).

[183] I. Boettcher, J. Braun, T. K. Herbst, J. M. Pawlowski, D. Roscher, and C. Wetterich, *Phase structure of spin-imbalanced unitary Fermi gases*, Phys. Rev. A **91**, 013610 (2015).

[184] D. Roscher, J. Braun, and J. E. Drut, *Phase structure of mass- and spin-imbalanced unitary Fermi gases*, Phys. Rev. A **91**, 053611 (2015).

[185] O. Goulko and M. Wingate, *Numerical study of the unitary Fermi gas across the superfluid transition*, Phys. Rev. A **93**, 053604 (2016).

[186] S. Nascimbène, N. Navon, K. J. Jiang, F. Chevy, and C. Salomon, *Exploring the thermodynamics of a universal Fermi gas*, Nature **463**, 1057 (2010).